



---

Doctoral Dissertations

Graduate School

---

5-2012

## Theoretical Modeling of the Formation and Functionality of Low-Dimensional Materials

Hua Chen  
hchen12@utk.edu

Follow this and additional works at: [https://trace.tennessee.edu/utk\\_graddiss](https://trace.tennessee.edu/utk_graddiss)

 Part of the Condensed Matter Physics Commons

---

### Recommended Citation

Chen, Hua, "Theoretical Modeling of the Formation and Functionality of Low-Dimensional Materials. " PhD diss., University of Tennessee, 2012.  
[https://trace.tennessee.edu/utk\\_graddiss/1280](https://trace.tennessee.edu/utk_graddiss/1280)

This Dissertation is brought to you for free and open access by the Graduate School at TRACE: Tennessee Research and Creative Exchange. It has been accepted for inclusion in Doctoral Dissertations by an authorized administrator of TRACE: Tennessee Research and Creative Exchange. For more information, please contact [trace@utk.edu](mailto:trace@utk.edu).

To the Graduate Council:

I am submitting herewith a dissertation written by Hua Chen entitled "Theoretical Modeling of the Formation and Functionality of Low-Dimensional Materials." I have examined the final electronic copy of this dissertation for form and content and recommend that it be accepted in partial fulfillment of the requirements for the degree of Doctor of Philosophy, with a major in Physics.

Hanno H. Weitering, Major Professor

We have read this dissertation and recommend its acceptance:

Pengcheng Dai, Adriana Moreo, Tim Schulze, Zhenyu Zhang

Accepted for the Council:

Carolyn R. Hodges

Vice Provost and Dean of the Graduate School

(Original signatures are on file with official student records.)

# **Theoretical Modeling of the Formation and Functionality of Low-Dimensional Materials**

A Dissertation

Presented for the

Doctor of Philosophy

Degree

The University of Tennessee, Knoxville

Hua Chen

May 2012

© by Hua Chen, 2012  
All Rights Reserved.

*To Qin*

# Acknowledgements

It would not have been possible to complete this thesis without the help and support of the kind people around me, to only some of whom it is possible to give particular mention here.

Above all, I would like to express my deepest gratitude to my wife Qin, who stood by me willingly through thick and thin in the long march toward my Ph.D. No words could thank you enough.

My most sincere and earnest thankfulness goes to my advisor, Prof. Zhenyu Zhang, for his generous help, support and patience in my doctoral study. I have learned so many things from him in various aspects of life and research, which helped to keep the fire in me burning so that this thesis could get to see the light of day.

I am most grateful to Dr. Wenguang Zhu, who taught me with great patience how to use the VASP software and many other skills which are crucial for me to complete the works included in this thesis.

I would like to thank the current and former members of our group: Dr. Shenyuan Yang, Dr. Ke Zhao, Dr. Xiaoguang Li, Dr. Di Xiao, Dr. Kirk H. Bevan, Dr. Claudia Troparevsky, Dr. Shunfang Li, Mr. Wei Chen, Mr. Robert Van Wesep, Ms. Guangfen Wu, Mr. Guo Li, *et al.*, for your help and support, for our collaborations and daily discussions, and for all the fun we have had together.

I am grateful to Prof. Qian Niu, who hosted me at the University of Texas at Austin during the last year of my doctoral study, and taught me many things related to the analytical approaches in condensed matter physics. My gratitude also goes to

Prof. Allan H. MacDonald at the University of Texas at Austin, who is kind enough to advise me on the project of electrically-tunable magnetic coupling in graphene, and I learned a lot from him on how to do phenomenological modeling.

I would like to thank the members of my doctoral committee: Prof. Pengcheng Dai, Prof. Adriana Moreo, Prof. Tim Schulze, and Prof. Hanno Weitering, for critical reading of this dissertation and helping to improve its contents.

Special thanks go to Prof. Yu Jia at Zhengzhou University, who gave me generous help and support at the very early stage of my scientific life, and introduced me to Prof. Zhenyu Zhang for graduate study.

Last, but by no means least, I am truly indebted and thankful to my parents, for their unconditional love and support through all these years.

# Abstract

This dissertation presents a series of work under the topic of designing and modeling novel low-dimensional materials and structures with desired and coherent structural, electronic, and magnetic properties, using a variety of theoretical tools, including first-principles density functional theory (DFT) method, numerical Monte Carlo (MC) method, and analytical phenomenological approaches, etc. The contents are divided into three major topics:

(1) Magnetic properties of *n-p* codoped materials. The noncompensated *n-p* codoping method is proposed to increase the density of magnetic dopants in diluted magnetic semiconductors (DMS) while keeping the magnetic coupling strength, which may lead to a high Curie temperature, comparable to room temperature. A two-step approach, combining first-principles and Monte Carlo methods, is developed to estimate the Curie temperatures of these systems.

(2) Growth and functionality of graphene. We focus on the nucleation processes of carbon adatoms in the early stages of graphene epitaxial growth on transition metal surfaces, and revealed that the strong interaction between C adatoms can lead to very different nucleation behaviors compared to conventional epitaxial growth. Our other works along this line include the prediction of stable carbon “nanoarches” in the early stages of graphene growth on Cu surface, the realization of graphene *p-n* superlattices using wedged Pb islands, and the proposal to suppress grain boundaries of epitaxial graphene by using superstructured Mn-Cu(111) surface alloy as substrates and a two-step kinetic pathway. In an ongoing work, we also found the compensated

*n-p* codoping method to be promising to establish long-range ferromagnetic order in graphene.

(3) Electronic and chemical properties of topological insulator (TI) heterostructures. By studying the structure of the TI  $\text{Bi}_2\text{Se}_3$  covered by an ultrathin gold film, we found that the unconventionally robust topological surface states (TSS) of the  $\text{Bi}_2\text{Se}_3$  can make the gold film a better platform for the adsorption and reaction of both CO and O<sub>2</sub> molecules, by acting as a charge reservoir. Following this work, we investigated the behavior of TSS in the heterostructures of TI and thin films of conventional insulators (CI), and discovered dual-proximity effects, implied by the spatial relocation of the TSS in the vertical direction.

# Contents

<b>List of Tables</b>	<b>xii</b>
<b>List of Figures</b>	<b>xiv</b>
<b>1 Introduction</b>	<b>1</b>
1.1 Characteristics of Low-Dimensional Materials . . . . .	2
1.1.1 Structural properties . . . . .	2
1.1.2 Electronic properties . . . . .	4
1.1.3 Magnetic properties . . . . .	7
1.2 Designing New Low-Dimensional Materials and Systems . . . . .	10
1.2.1 Electronic $\Rightarrow$ Structural . . . . .	10
1.2.2 Structural $\Rightarrow$ Electronic . . . . .	14
1.2.3 Structural/Electronic $\Rightarrow$ Magnetic . . . . .	16
1.3 Outline . . . . .	18
<b>2 Magnetic Properties of <i>n-p</i> Codoped Diluted Magnetic Semiconductors</b>	<b>19</b>
2.1 Introduction . . . . .	19
2.2 Methods . . . . .	21
2.3 <i>Ab initio</i> study of the codoping processes . . . . .	22
2.3.1 Intrinsic (Mn,IV) without additional dopants . . . . .	22
2.3.2 Energetics and kinetics of the codoped systems . . . . .	23

2.4	Magnetic properties of the codoped systems . . . . .	32
2.4.1	Magnetic coupling between Mn moments . . . . .	32
2.4.2	Curie temperature . . . . .	35
2.5	Dicussion and conclusion . . . . .	40
<b>3</b>	<b>Graphene: Growth and Functionality</b>	<b>45</b>
3.1	Contrasting Behavior of Carbon Nucleation in the Initial Stages of Graphene Epitaxial Growth on Stepped Metal Surfaces . . . . .	45
3.1.1	Introduction . . . . .	45
3.1.2	Methods . . . . .	47
3.1.3	Dynamics and kinetics of single carbon atoms on metal surfaces	47
3.1.4	Formation of carbon dimers on metal surfaces . . . . .	50
3.1.5	Generalization to other metal substrates . . . . .	52
3.1.6	Conclusion . . . . .	54
3.2	Stable Carbon Nanoarches in the Initial Stages of Epitaxial Growth of Graphene on Cu(111) . . . . .	56
3.2.1	Introduction . . . . .	56
3.2.2	Methods . . . . .	57
3.2.3	Energetic preference of linear carbon nanoarches for small clusters	58
3.2.4	Transformation from linear nanoarches to compact carbon islands	60
3.2.5	Discussion and conclusion . . . . .	61
3.3	Suppression of Grain Boundaries in Graphene Growth on Superstructured Mn-Cu(111) Surface . . . . .	63
3.3.1	Introduction . . . . .	63
3.3.2	Methods . . . . .	64
3.3.3	Formation of graphene GBs on Cu(111) surface . . . . .	65
3.3.4	Suppression of graphene GBs using a superstructurally alloyed substrate and a two-step kinetic pathway . . . . .	67
3.3.5	Discussion and conclusion . . . . .	72

3.4	Formation of Graphene <i>p-n</i> Superlattices on Pb Quantum Wedged Islands	72
3.4.1	Introduction . . . . .	72
3.4.2	Methods . . . . .	74
3.4.3	Oscillatory electron doping of graphene on Pb wedged islands	76
3.4.4	Realization of graphene <i>p-n</i> superlattice with the help of electric gating . . . . .	78
3.4.5	Discussion and conclusion . . . . .	82
3.5	Diluted Ferromagnetic Graphene via Compensated <i>n-p</i> Codoping . . .	85
3.5.1	Introduction and methods . . . . .	85
3.5.2	Enhancement in binding energies and magnetic moments of TM adatoms on graphene via <i>n-p</i> codoping . . . . .	86
3.5.3	Magnetic coupling between two <i>n-p</i> pairs . . . . .	87
3.5.4	Ongoing work . . . . .	89
<b>4</b>	<b>Topological Insulator Heterostructures</b>	<b>93</b>
4.1	CO Oxidation Facilitated by Robust Surface States on Au-Covered Topological Insulators . . . . .	93
4.1.1	Introduction . . . . .	93
4.1.2	Methods . . . . .	94
4.1.3	TSS on Au-covered Bi <sub>2</sub> Se <sub>3</sub> surface . . . . .	95
4.1.4	“Electron bath” effect of TSS in promoting surface reactions .	97
4.1.5	Discussion and conclusion . . . . .	101
4.2	Precise Tuning of the Vertical Location of Helical Surface States in Topological Insulator Heterostructures via Dual-Proximity Effects .	101
4.2.1	Introduction . . . . .	101
4.2.2	Methods . . . . .	103
4.2.3	Proximity effects in ZnS/Bi <sub>2</sub> Se <sub>3</sub> and ZnSe/Bi <sub>2</sub> Se <sub>3</sub> . . . . .	105
4.2.4	Reverse proximity effect in ZnTe/Bi <sub>2</sub> Se <sub>3</sub> . . . . .	108
4.2.5	Discussion and conclusion . . . . .	111

<b>5 Conclusion and Perspective</b>	<b>113</b>
<b>Bibliography</b>	<b>116</b>
<b>List of Publications</b>	<b>134</b>
<b>Vita</b>	<b>136</b>

# List of Tables

2.1	Calculated energy differences $\Delta E = E_f - E_i$ (in eV) between the final and initial states of Process I and Process II. $\varepsilon_a$ (in eV) is the activation energy for a transition from the initial to final state. Results highlighted in bold correspond to processes for which $\Delta E$ or $\varepsilon_a$ or both are $< 0.8$ eV. All the results are for Mn concentration of 1.56%; results for selected cases with Mn concentration of 0.46% are given in brackets.	27
2.2	Relative formation energy of substitutional and interstitial Mn in the presence of a neighboring substitutional <i>n</i> -type codopant, defined as: $\Delta E_2 = (E_{pair} + \mu_{host}) - E_{inter}$ (in eV). Negative values indicate higher stability of the substitutional configuration over the interstitial. The relative energy of substitutional and interstitial Mn in pure Si or Ge are included for comparison. . . . .	31
4.1	Binding energies (in eV) of CO and O <sub>2</sub> on three comparative substrates. (1) 2 ML Au on Bi-terminated Bi <sub>2</sub> Se <sub>3</sub> , (2) freestanding 2 ML Au fixed in the same geometry as in (1), and (3) (unreconstructed) Au(111) surface. The CO/O <sub>2</sub> coverage is 1/4 ML in (1) and (2), and 1/16 ML in (3). The geometries of adsorbed CO and O <sub>2</sub> are shown in Figs. 4.2 (e) and (f), respectively. . . . .	99



# List of Figures

1.1	Quantum corral formed by arranging Fe atoms on Cu(111) surface[1].	5
1.2	Schematic illustration of the formation of a chemical bond between an adsorbate valence level and the <i>s</i> and <i>d</i> states of a transition metal surface [2]. . . . .	7
1.3	Topological surface states on Bi <sub>2</sub> Se <sub>3</sub> . (a-c) ARPES measurements of the surface electronic bands on Bi <sub>2</sub> Se <sub>3</sub> (111). (d,e) Brillouin zone and surface Fermi surface of Bi <sub>2</sub> Se <sub>3</sub> . (f), Band structure from density functional theory calculations [3]. . . . .	9
2.1	Different Mn sites in bulk Si or Ge: (a) Mn at a substitutional site. (b) Mn at an interstitial site. (c) Final state of an interstitial Mn kicking out a neighboring host atom to an interstitial site and occupying the left-behind substitutional one. . . . .	24
2.2	Calculated relative total energy as a function of the distance between an interstitial Mn and a substitutional codopant in bulk Ge. . . . .	26
2.3	Atomic structures and schematic energy profiles for Process I: (a) Initial state with Mn in the <i>I<sub>T</sub></i> position (except for <i>n</i> -type doped Ge); (b) Final state; (c) Initial state for <i>n</i> -type doped Ge with Mn at the <i>I<sub>H</sub></i> position. . . . .	28
2.4	Calculated relative total energy as a function of the distance between a substitutional Mn and an interstitial <i>n</i> -type codopant in bulk Ge. .	29

2.5	Atomic structures and schematic energy profiles of Process II: (a) Initial state with Mn in the $I_T$ position (except for $n$ -type doped Ge); (b) Final state; (c) Initial state for $n$ -type doped Ge, with Mn at the $I_T$ position. . . . .	31
2.6	Relative total energy as a function of the distance between a substitutional Mn and a substitutional codopant in bulk Ge. . . . .	33
2.7	Total energy difference between AFM and FM states of two Mn atoms versus Mn-Mn separation for Mn/As doped Ge at (a) 3.125% and (b) 0.939% Mn concentration; (c) for two Mn/P pairs doped Si, represented by small orange dots. The large red dots are averages over the small orange dots for a given Mn-Mn distance. For comparison, the results for the systems doped with only two Mn impurities are shown as blue diamonds. . . . .	34
2.8	Magnetic coupling along different crystal directions. Black squares are for the (111) direction, red dots for the (110) direction and blue triangles for the (100) direction. Magnetic coupling along a close-packed chain is illustrated in the inset. . . . .	36
2.9	Comparison between Curie temperatures calculated by the Monte Carlo approach (MC, black squares) and those obtained by the mean field approximation (MFA, red dots). . . . .	38
2.10	Spin-spin correlation function obtained from the Monte Carlo simulations. . . . .	41

3.1 Top views of adsorption sites and binding energies of a C adatom around (a) Ir A-step, (b) Ir B-step , (c) Ru A-step, and (d) Ru B-step. The solid curves represent C diffusion profiles. The vertical dashed line represents the position of step edge, and the horizontal dot-dashed line indicates the C binding energy on flat surfaces. Definition of labels: U - upper terrace, L - lower terrace, R - ridge site where C only binds to atoms in the ridge of a step edge; b - hcp site, c - fcc site. . . . .	49
3.2 Binding energies of two C adatoms on flat metal surfaces as a function of their separation distance. Data points around the vertical dashed line correspond to the formation of C dimers. Inset shows the top view of a C dimer on a close-packed metal surface. Kinetic barriers are not shown. . . . .	51
3.3 (a) and (b) Top- and side-view of the most stable configuration of a C dimer at the lower edge of a (a) A-step and (b) B-step. (c-h) Binding energies of two carbon adatoms with one C atom fixed at the lower step edge and another placed in stable or metastable sites on upper terraces, lower terraces, or at the lower step edges, with increasing distances from the first adatom. Horizontal axis is their separation distance. Vertical dashed line in each panel shows where a C dimer is formed, and horizontal dot-dashed line shows the binding energy of two separate C adatoms on flat surfaces. . . . .	53
3.4 Binding energy difference between a C dimer ( $\Delta E_{\text{dimer}}$ ) and two separate C adatoms ( $2\Delta E_C$ ) with respect to $\Delta E_C$ on close-packed transition metal surfaces. Vertical dashed line corresponds to the binding energy of a C-C double bond (-6.33 eV). . . . .	55

3.5 (a) The formation energies per carbon atom of 1D linear chains and 2D compact islands consisting of 3-13 carbon atoms on Cu(111). (b) Top views of the relaxed 2D compact structures on Cu(111). Small orange and large gray balls represent C and Cu atoms, respectively. (c) Side views of the relaxed 1D nanoarch structures on Cu(111). Red arrows indicate the points where the arch collapses. . . . .	59
3.6 Energy profile and atomic structures (top view) of a 6C hexagonal ring breaking into a 1D chain. Small orange and large gray balls represent C and Cu atoms, respectively. . . . .	62
3.7 (a) and (b) Structural illustrations of the Cu (111) substrate and graphene, where the yellow and red dashed lines show their respective high-symmetry axes. (c) and (d) Illustrations of two geometries where a 7CR carbon cluster is at a HSO on the Cu(111) surface. In (c), the edge C atoms reside at the 3-fold hollow sites; in (d), the edge C atoms are at the bridge sites between two surface Cu atoms. . . . .	66
3.8 Side and top view of a 7CR on the Cu(111) surface, illustrating the domed nature (a) and the rotated nature (b) from the HSO of Fig. 3.7 (c), respectively. . . . .	67
3.9 (a) Structure of the $(\sqrt{3} \times \sqrt{3})$ R30° Mn-Cu(111) superstructurally alloyed surface. (b-d) Three stable geometries of a 7CR adsorbed on the Mn-Cu(111) surface. As indicated by the red dashed lines, (b) and (c) illustrate two HSO configurations, while (d) is rotated from a HSO, and their relative stabilities are indicated by their total energy differences. . . . .	69
3.10 Enlargement of coronene-seeded carbon islands via conventional CVD growth. The individual C adatoms supplied in the second step of the “seed and grow” kinetic pathway diffuse and attach to the nearby islands to fill the opening spaces, resulting in a larger graphene sheet with no GBs. . . . .	71

3.11 (a) Schematic illustration of a Pb wedged island grown on a Si(111) vicinal substrate. (b) The work function of Pb(111) films calculated within DFT as a function of the film thickness. . . . .	75
3.12 Atomic structures and calculated band structures of the two most stable configurations of graphene on 4-ML Pb(111) films [(a) and (b)], a single layer of graphene (c), and a 4-ML Pb(111) film (d). Red and blue balls represent C and Pb atoms, respectively. The Fermi levels are set to zero in the band structure plots, as denoted by blue dashed lines. In the graphene/Pb combined systems (a) and (b), the graphene band structure is highlighted via transparent red curves, and red short bars attached to the energy axis indicate the positions of the graphene Dirac point. . . . .	77
3.13 Band structure of graphene on 4- to 8-ML Pb(111) films [(a)-(e)]. The Fermi levels are set to zero in the band structure plots, as denoted by blue dashed lines. (f) The positions of the graphene Dirac point with respect to the Fermi level as a function of the thickness of the underling 4- to 8-ML Pb films. (g) The correlation between the position of the Dirac point and the work function of the Pb films. . . . .	79
3.14 (a) Schematic illustration of a graphene <i>p-n</i> superlattice formed on a Pb wedged island with an external electric field applied in the surface normal direction. (b) and (c) Evolution of the graphene Dirac point position plotted as a function of the electric field (b) and the Pb film thickness (c). The Fermi level is set to zero in all plots and denoted by green dashed lines. . . . .	80

3.15 (a) Electron screening charge for a graphene layer placed on a 7-ML Pb(111) film. The screening charge density is integrated in the plane parallel to the Pb(111) film and plotted in the perpendicular direction. Red and blue balls indicate the positions of C and Pb layers, respectively. (b) Amount of charge transferred out of the graphene versus the position of the Dirac point. Blue squares ( $\Delta Q_R$ ) are the total screening charge density integrated in real space from the zero point halfway between graphene and the Pb film into the vacuum. Yellow dots ( $\Delta Q_E$ ) are the amount of charge transfer estimated from integrating the graphene DOS in the range swept by the Fermi level. Green diamonds ( $\Delta Q_S$ ) are the summed screen charges of isolated graphene and the isolated Pb film (integrated in the same manner as $\Delta Q_R$ ). . . . . .	83
3.16 (a) A schematic plot of a <i>n-p</i> pair in graphene. H <sub>0</sub> represents a transition metal ( <i>n</i> -type) adsorption site, while S <sub>1</sub> -S <sub>7</sub> represent the positions of a substitutional B dopant ( <i>p</i> -type). (b) Dependence of the binding energy and the magnetic moment of a Fe adatom on its distance from a B dopant. (c) and (d) Enhancement in binding energies and magnetic moments of transition metal atoms on graphene with <i>n-p</i> codoping. . . . .	88
3.17 (a) Configurations of the <i>n-p</i> pairs considered in the calculation of magnetic coupling between two pairs. H <sub>0</sub> -H <sub>6</sub> represent adsorption sites of transition metal atoms, S <sub>0</sub> -S <sub>4</sub> represent the positions of B substitution. The first <i>n-p</i> pair is at the position H <sub>0</sub> -S <sub>0</sub> . (b) The magnetic coupling strength between two <i>n-p</i> pairs versus their separation.	90
3.18 DOS and PDOS plots of the H <sub>0</sub> S <sub>0</sub> -H <sub>3</sub> S <sub>2</sub> configuration shown in Fig. 3.17 (a). . . . .	91



4.3 (a) and (b) PDOS of an Au atom in the top layer of the 2 ML Au film with and without  $\text{Bi}_2\text{Se}_3$  substrate, respectively. In (b) the Au film is fixed in space. The red and black dot-dash lines indicate the positions of  $E_d$  with and without SOC, respectively. (c-e) Illustration of the role of the TSS in molecular adsorption. Blue-valence and conduction bands of the 3DTI support; light green-antibonding states of adsorbed molecules; red-TSS; dark green-metal  $d$  bands. (c) Without the TSS, the support will not be involved in the static electron transfer. (d) and (e) With the TSS, electrons of the molecule-metal system can be transferred either to or from the partially filled metallic surface states, depending on which way can lower the total energy. . . . . 102

4.4 Schematic illustration on tuning the vertical location of the topological surface states (TSS) as a topological insulator (TI) is covered with a layer of conventional insulator (CI). (a) TSS Floating to the top of the CI. (b) Staying put at the CI/TI interface. (c) Diving into the TI. (d) The atomic structure of  $\text{Zn}M/\text{Bi}_2\text{Se}_3$  ( $M = \text{S}, \text{Se}, \text{Te}$ ). The red lines denote the TSS; the arrows indicate the resulting directions of the topological phase transition. . . . . 104

4.5 Band structures of  $\text{ZnS}/\text{Bi}_2\text{Se}_3$  (upper row) and  $\text{ZnSe}/\text{Bi}_2\text{Se}_3$  (lower row) along the K- $\Gamma$ -M direction. The dots indicate the electronic bands contributed by the CI [(a) and (e)], the 1st QL of the TI [(b) and (f)], and the 6th QL [(c) and (g)], respectively; the sizes and colors of the dots also indicate different spectral weights and contributions from different atoms, respectively. (d) and (h) show the charge density distribution of the upper-surface TSS at the  $\Gamma$  point marked by the circle and indicated by  $\text{DP}_U$ . The  $\text{DP}_{U/L}$  stands for the Dirac point at the upper/lower surface. The grey and cyan bars denote the locations of the different QLs and the CI, respectively. . . . . 107



# Chapter 1

## Introduction

Low-dimensional materials generally refer to the systems with their dimension smaller than three, for example, thin films, nanowires, nanoparticles, superlattices, etc. Surfaces of bulk materials and physical entities with strong low-dimensional characters such as surface states can also be included in the general definition of low-dimensional systems. Low-dimensional materials and systems have been the focus of condensed matter physics and material science in the last decades, due to their unique properties and the tunability offered by their boundaries. Since the field of low dimensional systems has been growing into a important constituent of condensed matter physics, and there have already been numerous excellent books and review articles on almost any subfields, we are by no means trying to make this thesis a comprehensive review. Instead, we will focus on the topics that we have been working on in the past few years, and try to convey our strategy of exploiting the rich physics in low dimensions, that is, designing new systems or materials with desired structural, electronic, and magnetic properties, based on the delicate correlation between these factors.

## 1.1 Characteristics of Low-Dimensional Materials

In this section I will give an overview of some of the unique properties of low-dimensional systems that we have been interested in, divided into three categories, i.e, structural, electronic, and magnetic.

### 1.1.1 Structural properties

#### Surface reconstruction

Surface reconstruction and the special case of surface relaxation are fundamental issues in surface physics. They generally refer to the phenomena that the atomic arrangement near the surfaces of crystals are different from that in the bulk, due to the drastically different bonding environment at the surfaces. The behaviors of reconstruction are generally different in metals and in semiconductors. In the former the chemical bonds between metal atoms are essentially not directional and the bonding electrons are delocalized, while in the latter the covalent bonds are highly directional and localized in space [4]. It is therefore expected that surface reconstruction will be more complex in the case of semiconductors. A well known example is the  $7 \times 7$  reconstruction on the (111) surface of silicon.

In addition, for compound semiconductors such as GaAs, the reconstructed surface may have a different stoichiometry from the bulk to satisfy the requirement that the surface region be charge neutral. To account for this mechanism, a simple electron counting (EC) model has been developed [5, 6] and proven to be able to explain a wide variety of surface reconstructions [7–10]. According to the EC model, given the number of available electrons, a surface reconstruction will try to fill all the dangling orbitals on the electronegative elements while leaving those on the electropositive elements empty. For a specific surface, the EC model is used to identify a set of probable reconstructions, and the actual one has to be determined by further experimental or computational techniques.

## Epitaxy and thin film growth

Epitaxy means the registered formation of a crystalline overlayer on the surface of a crystalline substrate [4, 11]. The epitaxial films may come from either gaseous or liquid precursors deposited on the substrate. If the substrate is of the same composition as the overlayer, the epitaxy is called homoepitaxy. Otherwise it is heteroepitaxy. As an important experimental technique to fabricate thin films with good crystalline quality, a great number of studies have been devoted to the physics in epitaxy, especially the dynamics and kinetics in the thin film growth processes [12, 13].

Thin-film growth is typically divided into three regimes: island (Volmer-Weber), layer-by-layer (Frank-van der Merwe), and intermediate (Stranski-Krastanov). In the case of heteroepitaxy, the layer-by-layer growth is usually realized when the deposited adatoms bond to the substrate more strongly than to other adatoms. Therefore the second layer can only start to form after the completion of the first layer. In the opposite extreme, the adatoms strongly bond to each other and start to form three-dimensional clusters from the beginning. The clusters then grow into large islands, which finally merge to form a relatively thick film. In the intermediate regime, the growth starts from a layer-by-layer mode, and quickly transform to island mode after one or two layers are formed, which is primarily a strain effect.

Above arguments are based on simple energetic considerations in thermodynamic equilibrium. However, actual growth is almost always in the nonequilibrium regime, in which kinetics plays a crucial role. Microscopically, growth kinetics is usually determined by a few categories of atomistic rate processes [12], e.g., diffusion on flat surface and hopping across step edges, characterized by different energy barriers, e.g., surface diffusion barriers and the Ehrlich-Schwoebel step-edge barriers [14, 15]. The competition between different atomistic processes, which can be captured by Molecular Dynamics (MD) or Kinetic Monte Carlo (KMC) simulations, will lead to rich and complex growth phenomena.

One special case in thin film growth that requires a fundamentally different mechanism to explain is the quantum stability of metallic thin films on semiconductor substrates [16]. In such systems, the quantum confinement and the interface-induced Friedel oscillations of the delocalized conduction electrons of the metal in the direction perpendicular to the film surface can be the determining factors of the stability of the smooth metal film [17]. An especially interesting example is the Pb(111) films on various substrates [16], which display oscillatory stability of smooth films with thickness in the period of 2 monolayers.

### 1.1.2 Electronic properties

#### Surface states

Surface states are the states emerging as a solid material terminates at a surface, and are usually localized at the atomic layers closest to the surface [11]. The concept of surface states was individually proposed by Tamm [18] and Shockley [19], based on a tight-binding approach and the nearly-free electron approximation, respectively. As a celebrated example, the surface states on the (111) surfaces of simple and noble metals can be well described by a two-dimensional nearly-free electron gas. The electron density oscillations induced by the scattering of these states from surface defects can be probed using the scanning tunneling microscope, and a brilliant demonstration is the standing waves in the so-called quantum corral formed by a ring of Fe atoms on the Cu(111) surface (Fig. 1.1) [1].

Because of the spatial proximity, surface states may strongly influence the surface-related material properties, e.g., dissociation of molecules on metal surfaces [20], reconstructions on semiconductor surfaces [21], or catalytic properties of transition metal carbides [22]. However, surface states are extremely sensitive to local imperfections and can be easily destroyed without well-controlled laboratory environments.

The situation is different in the newly discovered topological insulator (TI) materials [23–25]. In these remarkable materials, strong spin-orbit interaction leads

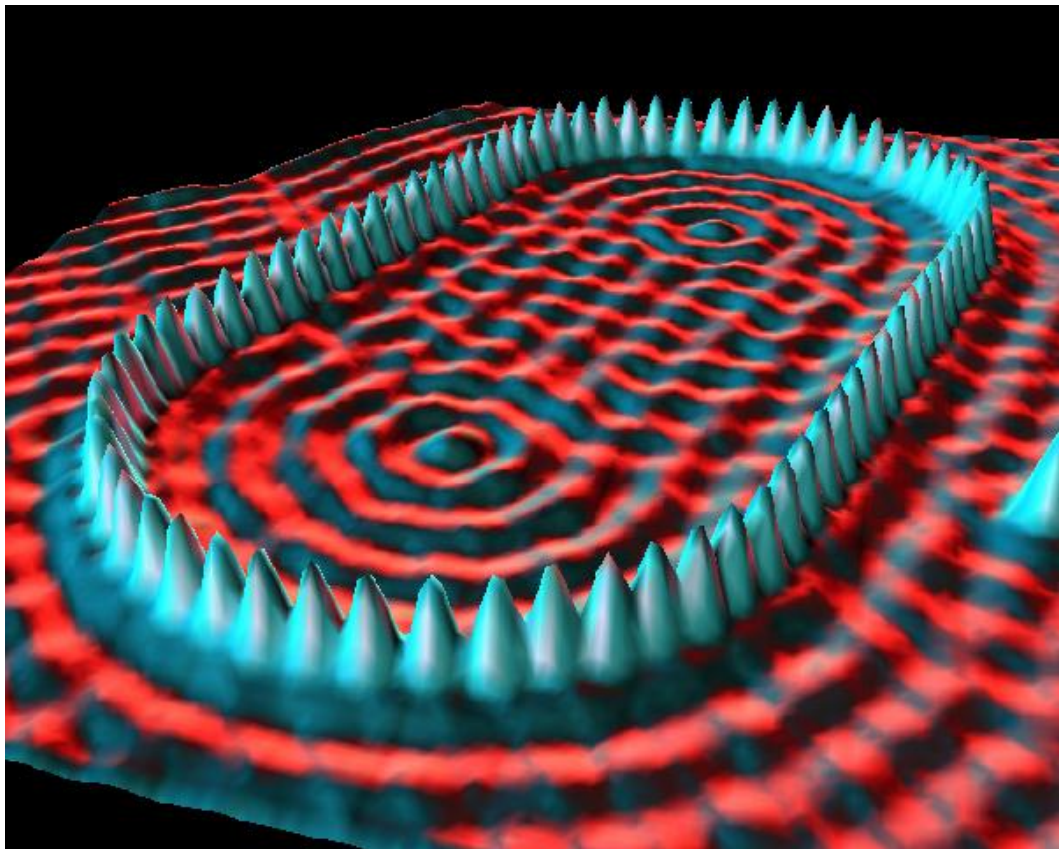


**Figure 1.1:** Quantum corral formed by arranging Fe atoms on Cu(111) surface[1].

to a nontrivial topology of the electron bands, resulting in the formation of robust metallic surface states. Unlike the surface states in conventional materials, these topological surface states (TSS) are insensitive to the structural details at the surfaces, e.g., non-magnetic impurities or defects, different surface orientations and terminations, and will persist as long as the bulk band gap is not closed.

### ***d*-band theory in heterogeneous catalysis**

In heterogeneous catalysis using transition metals as catalysts, the chemical bonding between the reactants and the metal is an important measure of the catalytic activity of the metal catalysts. To explain the different reactivity of different transition metal elements, a simple *d*-band model has been proposed [2, 26]. According to the *d*-band theory, the hybridization between the metal *s* bands and the orbitals of the molecular reactants gives a similar contribution to the total bonding energy for different transition metals. What determines the trend of chemical bonding between the molecules and transition metal substrates is the interaction between the metal *d* bands and the orbitals of the molecules (Fig. 1.2). By hybridization with the metal *d* bands, a molecular state will split into a bonding state and an antibonding state, and the energy gain from this hybridization will be determined by two factors. First, the filling of the antibonding state will lead to a repulsive interaction between the molecule and the substrate. Second, the larger the overlap between the molecular state and the metal *d* band before the hybridization is, the smaller the energy gain will be. Both factors correlate with the position of the *d* band in energy, and the *d*-band theory predicts that the lower the metal *d* band is in energy spectrum, the higher its contribution will be to the total bonding energy.

The *d*-band theory has been very successful in addressing the trend of chemical activity of all transition metals and noble metals in the periodic table. Variations of the *d*-band theory has also been developed to be applied to special locations on metal surfaces such as steps or defects, and nanoclusters. In these cases, the generally

higher chemical activity at the defect sites is also attributed to the energetically higher  $d$ -band centers at these locations [27].

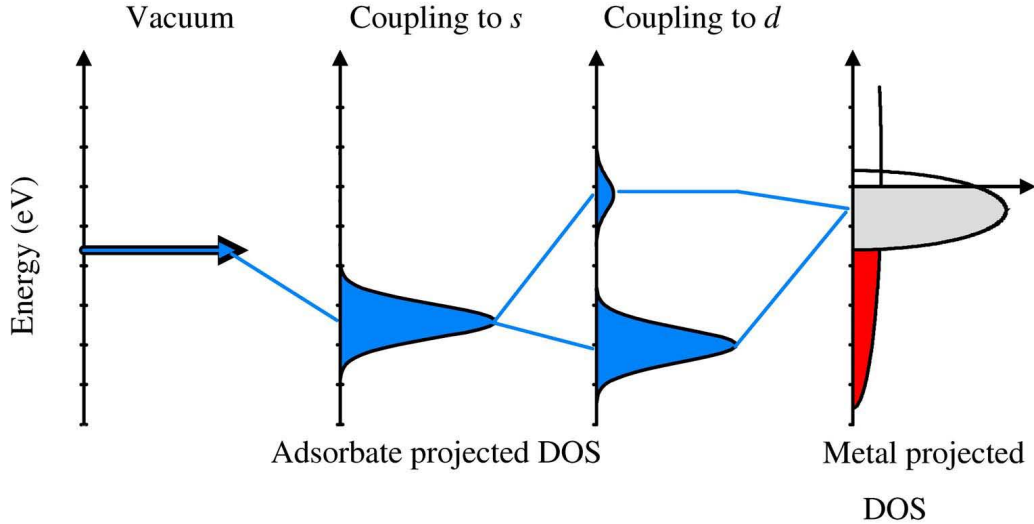


**Figure 1.2:** Schematic illustration of the formation of a chemical bond between an adsorbate valence level and the  $s$  and  $d$  states of a transition metal surface [2].

### 1.1.3 Magnetic properties

#### Ruderman-Kittel-Kasuya-Yosida (RKKY) interaction in low dimensions

In condensed matter physics, RKKY interaction [28–30] generally refers to the indirect exchange interaction between impurity spins in a metal or semiconductor, that is mediated by the charge carriers. RKKY interaction can be obtained from the second-order perturbation theory by treating the impurity spins as perturbations and integrating out the conduction electrons of the bulk material. The form of the RKKY interaction strength is a damped oscillation between ferromagnetic (FM) and antiferromagnetic (AFM) with increasing distance  $r$  between two spins, in which the damping is due to screening while the oscillation is from the finite Fermi wave vector at the Fermi level. Because of the different screening behavior in different dimensions, the form of RKKY interaction will also differ. The asymptotic behavior of RKKY

interaction for free-electron gas is  $\propto r^{-3}$  at large  $r$  in three dimension, and  $\propto r^{-2}$  in two dimension. Nevertheless, the specific form of RKKY interaction can be strongly system dependent even in the same dimensions. For example, the charge carriers of graphene are described by massless Dirac fermions, with the so-called pseudospin locked with the momentum direction. Such chiral nature of graphene charge carriers leads to a  $r^{-3}$  rather than  $r^{-2}$  dependence of the RKKY interaction in graphene [31].

Important applications of the RKKY theory in recent years include the theory of giant magnetoresistance, diluted magnetic semiconductors, and magnetically-doped graphene. In the latter two cases, for potential spintronic applications people generally desire ferromagnetic order induced by the RKKY interaction between the impurity spins. However, because of the structural frustration due to the random arrangement of the spins, and the oscillatory nature of RKKY interaction between FM and AFM, it is generally difficult to obtain a stable ferromagnetic system without significant compromise in other aspects, e.g., structural and electronic properties.

### **Quantum Hall effect and $Z_2$ topological insulators**

Quantum Hall effect is one of the most important phenomena of low-dimensional physics [32]. A general definition of the quantum Hall effect is the quantization of the Hall conductivity of two-dimensional electron systems under strong magnetic fields. For integer quantum Hall effect, the quantization is due to the formation of discrete Landau levels because of the external magnetic field. What is especially interesting is, although the electron system is supposed to be insulating when the Fermi level lies between two adjacent Landau levels, the transverse Hall conductivity is still nonzero. This nonzero conductivity is actually due to the edge states of the quantum Hall system. In a more formal language, the quantum Hall system is characterized by a nonzero topological invariant called first Chern number. Whereas the vacuum is a topologically trivial insulator in the sense that its first Chern number is zero. At the interfaces of topologically nonequivalent insulating systems, gapless edge states must emerge due to the topological phase transition.

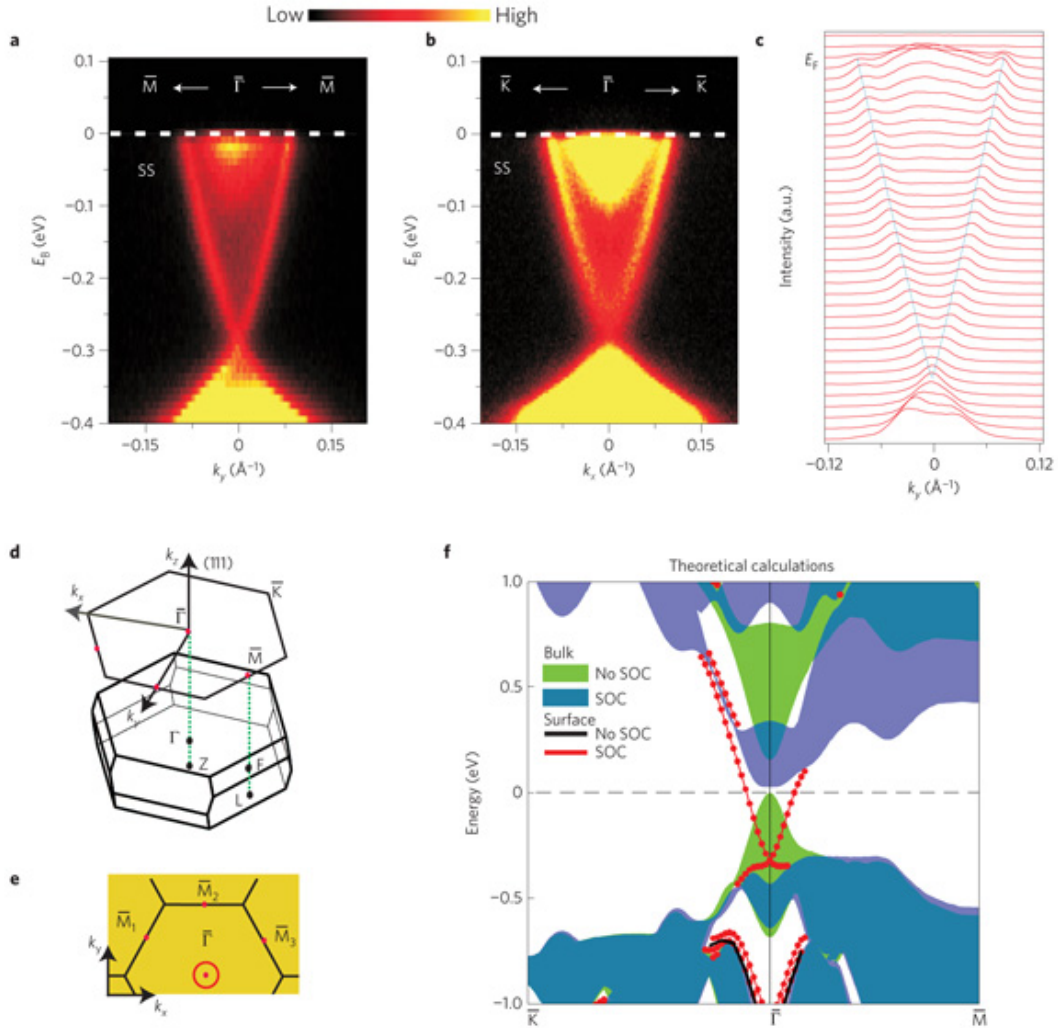


**Figure 1.3:** Topological surface states on  $\text{Bi}_2\text{Se}_3$ . (a-c) ARPES measurements of the surface electronic bands on  $\text{Bi}_2\text{Se}_3(111)$ . (d,e) Brillouin zone and surface Fermi surface of  $\text{Bi}_2\text{Se}_3$ . (f), Band structure from density functional theory calculations [3].

Topological insulators are very similar to quantum Hall systems in the sense that topologically protected gapless surface/edge states emerge at their surfaces/edges (Fig. 1.3) [23–25]. The difference is that the role of strong magnetic fields in quantum Hall systems is replaced by strong spin-orbit coupling in topological insulators, and the topological invariant in the latter is called second Chern number ( $Z_2$ ). What is more interesting in topological insulators is that their surface states have linear Dirac-cone like dispersion, and are spin-momentum-locked, or in other words, helical. The exotic surface states can lead to many interesting phenomena such as Majorana fermions at topological insulator-superconductor interface [33], topological magnetoelectric effect [34], quantized anomalous Hall effect [35], etc.

## 1.2 Designing New Low-Dimensional Materials and Systems

In this section we give an overview of our recent works under the general topic of designing new low-dimensional materials, with a special organization based on the relations between structural, electronic, and magnetic properties. More specifically, we will emphasize how the desired properties of the new systems are realized by understanding and utilizing their dependence on other fundamental material properties.

### 1.2.1 Electronic $\Rightarrow$ Structural

#### Semiconductor surface reconstruction induced by metal adsorbates

Metal growth on semiconductors is indispensable for many important technological applications. At the earliest stages of growth, adsorption of a submonolayer of metal often leads to the appearance of much richer surface reconstruction patterns than that in the corresponding homogeneous case. For instance, at low coverage, alkali metals form one dimensional long chains on III-V(110) surfaces in the [1 -1 0] direction [36].

Deposition of  $\text{Sb}_4$  on  $\text{GaAs}(110)\text{-}\beta2(2\times4)$  surface produces a  $(2\times8)$  reconstruction that turns to a  $(2\times4)$  surface upon annealing [37], whereas adsorption of Mn on the same substrate leads to a smaller  $(2\times2)$  reconstruction [38]. Not only are the atomic structures of these reconstructions interesting in themselves, but they also influence the metal/semiconductor contacts such as the smoothness of the interface, the optimization of the growth of the epitaxial films, the Fermi energy pinning, and the Schottky barrier heights. However, further understanding of the reconstruction patterns is hindered by the complexity of the interactions at the interface induced by the metal adsorbates.

To address this problem, we proposed a generalized electron counting (GEC) rule [21, 39] that is able to explain a wide range of metal-induced compound semiconductor reconstructions. In the GEC rule, the metal adsorbates serve primarily as an electron bath by donating or accepting the right number of electrons, as the host surface chooses a specific reconstruction that obeys the classic EC model. This generalization is rooted in the realization that metal atoms are generally far less demanding in forming directional chemical bonds and are more susceptible to charge transfer. Accordingly the metal adsorbates will play a flexible role in selecting a particular reconstruction. Just like its classic counterpart, the GEC rule can dramatically simplify the task of determining the reconstructions for a specific metal/semiconductor adsorption system by greatly narrowing down the number of possible structures out of many candidate patterns in configuration space.

## Graphene epitaxial growth

The epitaxial growth of graphene on transition metal surfaces is a promising approach to controllably fabricating large graphene sheets [40–53]. However, back in 2009, the detailed growth mechanism of graphene was still unclear. We entered this field by focusing on the nucleation processes of carbon adatoms in the early stages of graphene growth, and carried out a comparative study among three representative metal substrates:  $\text{Ru}(0001)$ ,  $\text{Ir}(111)$ , and  $\text{Cu}(111)$  [54]. Using density functional theory

(DFT) approach, for the first time we revealed that the strong interaction between C adatoms can lead to very different nucleation behaviors compared to conventional epitaxial growth. Specifically, we found that due to the competition between C-C binding and C-metal binding, for strong C-metal binding systems [e.g. Ru(0001) and Ir(111)], C nucleation must start from step edges on the substrates, which agrees with experiments; whereas for weak C-metal binding systems [e.g. Cu(111)], C adatoms should be able to nucleate from everywhere on the substrates.

Following this work, we start to focus on the substrate of Cu, which has been shown to be one of the most promising substrates for mass production of quality epitaxial graphene [45, 51, 55–57]. We reveal an energetic preference for the formation of stable one-dimensional carbon “nanoarches” consisting of 3-13 atoms when compared to two-dimensional compact islands of equal sizes [58]. The reason still lies in the competition between C-C binding and C-Cu binding. Because the latter is much weaker than the former, the dangling  $\sigma$  bonds at the divalent bent vertices of isolated carbon rings cannot be sufficiently saturated, and the energy required to bend the  $sp$  carbon atoms cannot be provided. The stronger C-C bonding also dictates the arched shape of the chains, because the carbon atoms in the middle can only weakly interact with the metal substrate after forming strong C-C bonds with two carbon neighbors.

One standing obstacle in epitaxial growth of graphene on Cu is the prevalence of grain boundaries (GBs) undesirably introduced during growth [59–66]. The presence of GBs has been shown to severely degrade the electronic, transport, and mechanical properties of graphene [59, 64]. To address this problem, we first demonstrate that the abundant orientational disorder of initial carbon islands on Cu(111), which is due to the weak C-Cu interaction, is the underlying reason for the formation of graphene GBs upon island coalescence. Based on this understanding, we propose to use a superstructured Mn-Cu(111) alloyed surface to pin all the carbon islands predominantly at one orientation. Our proposed kinetic pathway invokes the steps of “seed and grow”. In the seeding step, carbon clusters are initiated by depositing

large aromatic hydrocarbon molecules on the superstructured Mn-Cu(111) surface. In the growing step, larger, monolayer graphene is formed by conventional chemical vapor deposition (CVD).[67]

### ***n-p codoping in diluted magnetic semiconductors***

Diluted magnetic semiconductors (DMS) provide a fascinating platform for both fundamental studies of ferromagnetic ordering mechanisms and potential device applications in spintronics [68–74]. One crucial issue in DMS is how to achieve high Curie temperature that is comparable to room temperature. For (III,Mn)V as well as (Mn,IV) systems, both theoretical and experimental investigations indicate that the Curie temperature is very sensitive to the ratio of interstitial to substitutional Mn atoms [73, 75–78]. In these systems, substitutional Mn atoms act as acceptors and provide holes, which are the mediator of magnetic interactions between magnetic moments in these materials. Whereas interstitial Mn atoms are donors and tend to compensate the holes and magnetic moments induced by the substitutional Mn. However, it is found to be difficult to decrease the amount of interstitial Mn using conventional methods such as annealing in (Mn,IV) systems [79–82].

We proposed a novel *n-p* codoping method to enhance the substitutional doping of Mn in Ge and Si [83, 84]. In this method, an additional conventional electronic dopant such as As and P is introduced in the doping process. Using DFT approach, we revealed that the new method can substantially lower the relative energy of Mn at substitutional sites to interstitial, as well as the energy barrier which the Mn ions have to overcome to enter substitutional sites, through the formation of stable *n-p* dopant pairs. The strong thermodynamic stability of the substitutional Mn/*n*-type-dopant pair structure is attributed to the opposite charge states of the two elements in the host semiconductors: A substitutional Mn, acting as a *p*-type double acceptor in bulk Si or Ge, is attracted to a substitutional *n*-type dopant. The codoping is in essence noncompensated, therefore the magnetic interaction in the DMS systems is

largely preserved. The noncompensated  $n$ - $p$  codoping method has also been applied to TiO<sub>2</sub> for solar cell applications [85].

### 1.2.2 Structural $\Rightarrow$ Electronic

#### Graphene $p$ - $n$ superlattice

Due to the novel massless Dirac fermion characters of the charge carriers of graphene, many exotic transport properties of graphene-based structures have been proposed and investigated. One of the most intriguing systems is the graphene  $p$ - $n$  superlattice, in which a number of fascinating phenomena have been predicted, including electron-beam supercollimation [86], anisotropic transmission [87], creation of additional Dirac cones [88, 89], and effective magnetic fields [90], etc. However, the creation of well-ordered and atomically sharp  $p$ - $n$  junctions or superlattices remains challenging in practice.

We devised a novel scheme to create graphene  $p$ - $n$  superlattices by using Pb wedged islands as the substrates of graphene [91]. The Pb wedged islands, with an atomically flat (111) surface and their bottom extending laterally over several atomic steps, have been grown on Si(111) vicinal substrates at room temperature [92]. Previous theoretical and experimental studies have shown that Pb(111) films exhibit a bilayer work function oscillation due to the unique matching between the bulk Pb Fermi wavelength and the Pb(111) interlayer lattice spacing [93–96]. Therefore, when a single layer of graphene is placed on the surface of such a Pb wedged island, the spatial oscillation in the surface work function will induce an oscillatory electronic doping of the graphene. The oscillatory doping can be further turned into  $p$ - $n$  oscillation by applying an external electric field perpendicular to the surface. Therefore the graphene layer becomes a well-defined  $p$ - $n$  superlattice with seamless junctions.

## **Gold-coated topological insulators in heterogeneous catalysis**

Protected by time-reversal symmetry, the topological surface states (TSS) of topological insulators are inherently more robust against surface modifications than conventional surface states. Such robustness makes TSS a perfect platform for investigating the catalytic role of surface states in less constrained environments.

We employ first-principles density functional theory to demonstrate that the TSS can play a vital and elegant role in facilitating surface reactions by serving as an effective electron bath [97], which is reminiscent of the role of metal adatoms in semiconductor surface reconstruction in Sec. 1.2.1. We use CO oxidation on gold-covered topological insulator  $\text{Bi}_2\text{Se}_3$  as a prototype example, and first show that the TSS is preserved when a stable ultrathin Au film is deposited onto a Bi-terminated  $\text{Bi}_2\text{Se}_3$  substrate. Furthermore, we found that the TSS can significantly enhance the adsorption energy of both CO and  $\text{O}_2$  molecules, by promoting different directions of electron transfer. For CO, the TSS accepts electrons from the CO-Au system, thereby decreasing the undesirable occupation of the CO antibonding states. For  $\text{O}_2$ , the TSS donates the needed electrons to promote the molecule towards dissociative adsorption.

## **Heterostructures of topological insulators and conventional insulators**

In integrating topological insulators (TI) with normal materials for device applications, one importance issue is how the TSS will behave in such heterostructures. The model system in the previous subsection is a heterostructure made of TI and metal. For conventional insulators (CI), theory predicts the TSS will always appear at the interface between a TI and a CI [23–25]. However, the prediction is based on continuum models without taking the atomic details at the interface into account. It will be interesting to see what will actually happen at a realistic CI/TI interface, and how the general theories need to be modified to account for any new phenomena.

We investigated a special CI/TI heterostructure, by depositing a single stoichiometric layer of CI ( $\text{ZnM}$ ,  $\text{M} = \text{S}$ ,  $\text{Se}$  or  $\text{Te}$ ) onto a TI substrate ( $\text{Bi}_2\text{Se}_3$  or  $\text{Bi}_2\text{Te}_3$ ). Using first-principles method based on DFT, we discovered novel dual proximity effects at the CI/TI interface, which may help to accurately tune the spatial locations of TSS in the direction perpendicular to the surface [98]. We found that, the TSS can float up to the top surface of the  $\text{ZnM}$  film, stay at the CI/TI interface, or be pushed down one quintuple layer deeper inside the TI substrate. These contrasting behaviors imply a rich variety of possible topological phase transitions in the narrow region immediate to the interface, determined by several material-specific parameters such as spin-orbit coupling (SOC), band gap, and work functions. These discoveries lay the ground for precise manipulation of the real space properties of TSS in TI heterostructures.

### 1.2.3 Structural/Electronic $\Rightarrow$ Magnetic

#### Diluted ferromagnetic graphene via $n$ - $p$ codoping

Graphene is an especially promising candidate for spintronic applications [99], because of the high charge carrier mobility and long spin coherence time. There have been a lot of efforts in trying to introduce long-range ferromagnetic order in graphene [100–104], among which adsorption of transition metal (TM) atoms on graphene is one of the most explored approaches [105–112]. However, rather than that in diluted magnetic semiconductors, dilute ferromagnetism has not been realized in TM decorated graphene. The major reasons include the weak binding between the TM adatoms and graphene, and the strong suppression of the magnetic moments of the TM adatoms upon adsorption on graphene [111, 112].

We demonstrated that the  $n$ - $p$  codoping method, formerly applied in DMS by us (Sec. 1.2.1) [83, 84], can lead to significant enhancement in both the binding of TM adatoms to graphene and their magnetic moments. We first show that the TM adatoms (Fe, Co, and Ni), as  $n$ -type dopants in graphene, will strongly bind to

the substitutional *p*-type dopant B atoms due to electrostatic attraction, therefore suppressing the clustering of the adatoms. Furthermore, the magnetic moments of all the three TM adatoms are found to be enhanced due to the doping effect by B. Particularly, Ni acquires a moment of  $0.57 \mu_B$ . We then find that, although Co-B or Fe-B codoping will likely open a band gap and thus hinder the long-range carrier-mediated magnetic interaction, Ni-B co-doping preserves the Dirac band structure and has RKKY-like long-range magnetic interaction. An estimate of the Curie temperature is finally given using a Monte Carlo approach with DFT input.

### **Electrically-tunable RKKY coupling between magnetic nanoparticles on graphene**

As introduced in Sec. 1.1.3, the periodicity of the FM-AFM oscillation of the RKKY interaction is determined by the Fermi wave vector or the Fermi level. It is thus intuitive that if the magnetic order of a system is built upon the RKKY interaction, the magnetic order should be able to be tuned by changing the Fermi level. However, in normal 3D systems it is usually difficult to change the Fermi level freely, because of the large density of states at the Fermi level. Graphene offers a new hope towards this route, because of its small density of states around the Dirac point. And it has been shown experimentally that the Fermi level of graphene can be easily tuned by an electric gate on top of the graphene [113]. It is therefore possible to realize an electrically-tunable magnetic system based on graphene.

To this end, we have been developing a theory of the carrier-density-dependent coupling between magnetic nanoparticles adsorbed on a graphene sheet. We choose transition metal nanoparticles instead of single adatoms because of the larger magnetic anisotropy energy of the former, which will make the system more susceptible to temperature. A phenomenological Dirac-band model is developed to calculate the RKKY interaction between TM nanoparticles, and the model uses kinetic exchange coupling parameters extracted from DFT calculations. Small system

DFT coupling strength results will be finally compared with that from the model to verify the consistency.

### 1.3 Outline

The remaining part of this thesis is organized as follows. From Chapter 2 to Chapter 4, I will go into more details of the topics summarized in the previous section. The organization of the topics are based on the closeness of their respective fields. Chapter 2 is devoted to the method of *n-p* codoping in diluted magnetic semiconductors [84]. Chapter 3 is on the growth and functionality of graphene, including the microscopic kinetics and dynamics in the initial stages of graphene epitaxial growth on metal surfaces (Secs. 3.1 and 3.2) [54, 58], the proposal to suppress grain boundaries in graphene using a superstructured alloyed substrate and a two-step kinetic pathway (Sec. 3.3) [67], the realization of graphene *p-n* superlattices using Pb wedged islands (Sec. 3.4) [91], and the dilute ferromagnetism in graphene via compensated *n-p* codoping (Sec. 3.5) [114]. Chapter 4 is on the heterostructures of topological insulators, including the “electron bath” effect of topological surface states in promoting surface catalysis (Sec. 4.1) [97], and the dual-proximity effects at the topological insulator-conventional insulator interface (Sec. 4.2) [98]. Finally in Chapter 5 conclusions and perspectives of the works included in this thesis will be given.

# Chapter 2

## Magnetic Properties of *n-p* Codoped Diluted Magnetic Semiconductors

### 2.1 Introduction

Diluted magnetic semiconductors (DMS) have attracted much interest in the condensed matter community not only because of their promising application in spintronic devices [68, 69], but also because of the many new and important theoretical issues which arise from the study of this unique class of disordered magnetic system [70–74]. As for specific materials, besides the most extensively studied (III,Mn)V systems [74, 115], Mn doped group-IV semiconductors such as Ge and Si also show promise for real applications [116–122]. In order to realize this promise, a Curie temperature comparable to room temperature or higher is required. Both theory and experiment indicate that the Curie temperature of the above-mentioned materials is exceptionally sensitive to the ratio of interstitial to substitutional Mn atoms [73, 75–78]. In (III,Mn)V as well as (Mn,IV) systems, substitutional Mn atoms act as acceptors and provide holes which, according to current understanding, are

the mediator of magnetic interactions between magnetic moments in these materials. Interstitial Mn atoms [77] are identified to be donors, and tend to compensate the holes and magnetic moments induced by the substitutional Mn [74]. Furthermore, though annealing is an effective way to decrease the percentage of interstitial Mn while keeping the homogeneity in (Ga,Mn)As, [123, 124] it is less useful for  $Mn_xGe_{1-x}$  and  $Mn_xSi_{1-x}$ , [79–82] which makes it very difficult to get high quality samples of these materials using conventional methods.

In our earlier work [83], a novel way to enhance the substitutional doping of Mn in Ge and Si was proposed. In this method, an additional conventional electronic dopant (e-dopant) such as As or P is introduced in the doping process. Using first-principles electronic structure calculations, we were able to show that the codoping approach can substantially lower the energy of Mn atoms at substitutional sites relative to that at interstitial sites, as well as the energy barrier which the Mn atoms have to overcome in order to be incorporated into substitutional sites. In addition, the assisting e-dopant enhances the magnetic coupling between substitutional Mn atoms.

In this section, we present a detailed *ab initio* investigation of this novel approach by analyzing the kinetic and thermodynamic issues related to the stability of various dopant-host combinations. We then calculate the magnetic coupling between two Mn atoms in bulk Ge and Si, and find that in Ge, the coupling oscillates between positive (ferromagnetic) and negative (antiferromagnetic) values with the Mn-Mn distance. But in Mn/As codoped Ge the coupling parameter remains positive at all distances beyond nearest-neighbors, and this qualitative difference does not change with the doping level. For Mn doped Si, all the couplings except for the nearest neighbor one are positive and do not change much upon codoping. We also carry out Monte Carlo simulations to obtain the Curie temperatures of the codoped materials. We find that in Mn doped Ge no ferromagnetic order exists for Mn concentrations ranging from 3.13% to 6%. Instead, a spin-glass phase transition occurs at  $\sim 5$  K at 5% Mn doping. For Mn/As codoped Ge,  $T_c$  increases nearly linearly with the Mn concentration and reaches 264 K at 5% Mn doping.

## 2.2 Methods

Our spin-polarized first-principles calculations are carried out using the Vienna *ab initio* simulation package (VASP) [125], a density functional theory approach using the projector augmented wave (PAW) method [126, 127] and the generalized gradient approximation (PBE-GGA) [128] for exchange-correlation. A default plane-wave energy cutoff of 269.9 eV is consistently used in all Mn calculations. These choices produce a bulk Ge and Si lattice constants of 5.78 Å(experimental value [129] 5.66 Å) and 5.47 Å respectively (experimental value 5.43 Å).

In our calculations of the codoping process the supercell size is chosen to be a  $2 \times 2 \times 2$  multiple of the conventional cubic cell of the diamond lattice which contains 8 atoms. Hence, there are 64 atoms in one supercell, and one of them is replaced by an Mn atom, corresponding to 1.56% Mn concentration, comparable to what was achieved experimentally [116, 130, 131]. Different supercell sizes were used to study the dependence of calculated results on Mn concentration. Specifically, we used a  $3 \times 3 \times 3$  supercell, which corresponds to 216 atoms, and with one of them replaced by a Mn the concentration is 0.46%. In each calculation of the magnetic coupling between Mn atoms, two Mn atoms are placed in a  $3 \times 3 \times 3$  supercell, corresponding to a 0.926% Mn concentration. We also selectively use a  $2 \times 2 \times 2$  supercell for the magnetic coupling with two Mn atoms in the supercell, corresponding to 3.125% Mn, for comparison. This setup is similar to previous studies of Mn-Mn interactions in pure semiconductors [132–135].

A uniform  $4 \times 4 \times 4$  ( $2 \times 2 \times 2$ ) mesh, including the  $\Gamma$  point (0, 0, 0), is chosen for Brillouin zone sampling in the  $2 \times 2 \times 2$  ( $3 \times 3 \times 3$ ) supercell. Optimized atomic geometries are obtained when the forces on all the unconstrained atoms are smaller in magnitude than 0.01 eV/Å. The “climbing image Nudged Elastic Band” (NEB) method [136] is used to locate the transition state geometries for the calculation of activation energy barriers. Typically four slab replicas between the initial and final geometries are enough to produce a smooth minimum energy path.

For the Monte Carlo simulations we use the Metropolis algorithm and the magnetic energy of the system is calculated using the classical Heisenberg model, in which each magnetic ion is treated as a classical moment and is placed at a randomly chosen site of the supercell. The magnetic coupling parameters are extracted from *ab initio* results of the energy difference between parallel and antiparallel spin configurations of two Mn moments at different separations. At each temperature we use 50000 Monte Carlo steps per moment for the system to relax, and calculate the thermal average in the following 50000 steps. To determine the Curie temperature, we adopt the fourth order cumulant crossing method based on finite-size scaling theory proposed by Binder [137]. In applying this method we choose three supercell sizes:  $8 \times 8 \times 8$ ,  $10 \times 10 \times 10$ ,  $12 \times 12 \times 12$ , and 40 configurations in each case for averaging.

## 2.3 *Ab initio* study of the codoping processes

### 2.3.1 Intrinsic (Mn,IV) without additional dopants

We first consider the equilibrium structure of a single Mn dopant atom in bulk Si and Ge, and show where the difficulty of lowering the percentage of interstitial Mn impurities is coming from. A complete understanding of the microscopic doping process requires detailed knowledge of the energetics as well as the kinetics of dopants in the host material [76]. In fact, an in-depth understanding of the growth kinetics is particularly important, because DMS systems are typically in a metastable state, grown by codoping the magnetic dopants and host semiconductor atoms using molecular beam epitaxy under nonequilibrium conditions [116, 130, 138, 139].

The relative formation energy of a substitutional Mn(Fig. 2.1(a)) and interstitial Mn(Fig. 2.1(b)) atom in Ge or Si is defined as:

$$\Delta E_1 = (E_{\text{subst}} + \mu_{\text{host}}) - E_{\text{inter}}, \quad (2.1)$$

where  $\mu_{host}$  is the chemical potential of the host material. For Ge, our calculation gives  $\Delta E_1 = -0.63\text{eV}$ . Thus, in Ge the substitutional sites have a relatively lower energy and are preferred by Mn atoms. However, for Si the opposite is true and  $\Delta E_1 = +0.58$ . This reversed site preference [140] makes it extremely hard to achieve even a nominal concentration of substitutional Mn in silicon experimentally.

We next consider kinetic aspects of the Mn doping process. In order to get a high ratio of substitutional to interstitial Mn, the process that an interstitial Mn kicks out a host atom and becomes substitutional must take place more often than the reverse process. Accordingly, we calculate the energy difference between the initial (interstitial, (2.1)(b)) and final (substitutional, (2.1)(c)) states of this process:  $\Delta E = E_f - E_i$ , and the energy barriers  $\varepsilon_a$  and  $\varepsilon'_a$  for the reverse process. Our calculation shows that for both Ge and Si  $\Delta E$  is positive (0.82 eV and 2.03 eV respectively). This energy cost for the transition from initial to final state defines the lower bound of the activation energy barrier for the exchange process, which must be lower than  $\sim 0.8$  eV for efficient incorporation (with a standard attempt frequency  $10^{12} \text{ sec}^{-1}$ ). Moreover, the actual energy barrier  $\varepsilon_a$  in either case (1.12eV for Ge and  $>2\text{eV}$  for Si) is higher than the barrier of the reverse process, which is calculated as  $\varepsilon'_a = \varepsilon_a - \Delta E$ , with the latter being lower than 0.8 eV, further facilitating the reverse processes. Thus, kinetically Mn is more stable at interstitial sites rather than at substitutional sites in both Ge or Si.

### 2.3.2 Energetics and kinetics of the codoped systems

Substitutional Mn in Ge is a *p*-type double acceptor [141]. Our proposal for a codoping mechanism is based on the fact that the electrostatic interaction between a *n*-type and a *p*-type dopant in a semiconductor is attractive because of their different charge states (see below). Thus an *n*-type dopant may help to stabilize substitutional Mn atoms.

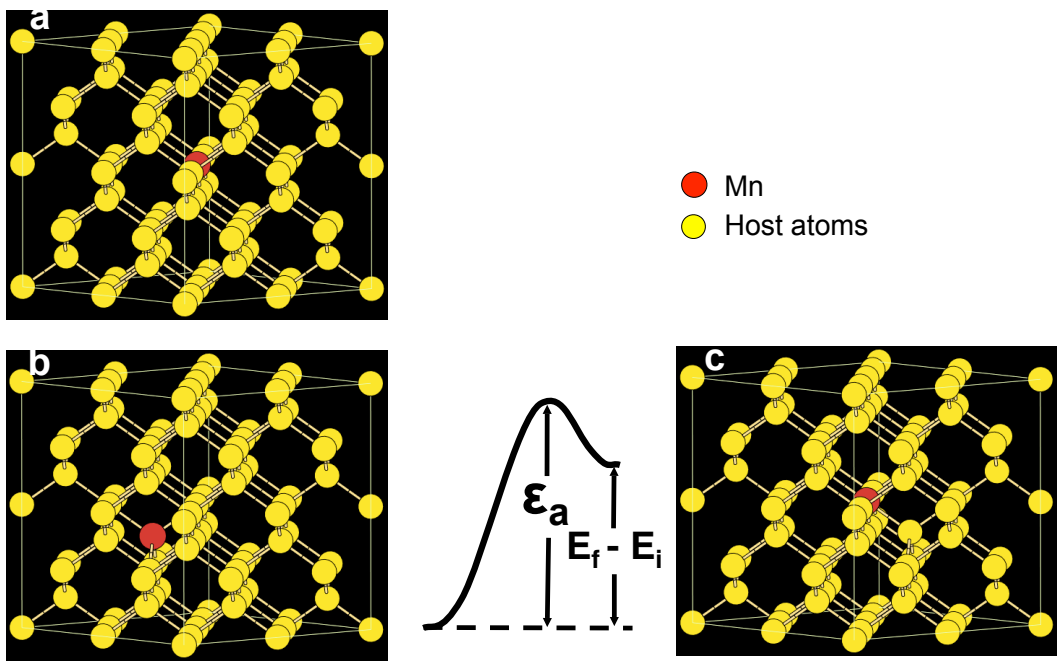


**Figure 2.1:** Different Mn sites in bulk Si or Ge: (a) Mn at a substitutional site. (b) Mn at an interstitial site. (c) Final state of an interstitial Mn kicking out a neighboring host atom to an interstitial site and occupying the left-behind substitutional one.

We start by noting that in Ge or Si there are two kinds of interstitial sites: the hexagonal interstitial site  $I_H$ , which has six nearest neighbors, and the tetrahedral site  $I_T$  with four nearest neighbors. Using first-principles calculations we find that in *n*-type doped Ge and Si, the energy of a Mn sitting at the  $I_H$  site is different from that at the  $I_T$  site. For P, As and Sb doped Ge, the energy differences are 0.14, 0.09 and 0.04eV, respectively, where a positive sign means the  $I_H$  occupation has lower energy and is preferred. In the case of either *n*- or *p*-doped Si as well as *p*-doped Ge,  $I_T$  is preferred to  $I_H$ . This codopant dependent preference can be qualitatively explained by the local strain effect. Namely, a Mn atom and an *n*-type codopant favor a relatively short bonding distance, which is accommodated by Mn occupying the  $I_H$  site rather than the  $I_T$  site in Ge (the  $I_H$  site has a shorter distance to its nearest neighbors than the  $I_T$  site). To show that this is indeed the case, we reduce the lattice constant of Ge to the value of Si and calculate the energy difference again. Then the results show that the preference for Mn is changed to the  $I_T$  site, because in this case the distance between the  $I_H$  Mn and *n*-type codopant becomes too short (compressive), whereas at the  $I_T$  site the Mn/*n*-type codopant bond length is close to its optimal value. We have also checked to confirm that if we increase the lattice constant of Si to that of Ge, the preference for Mn is changed to the  $I_H$  site for the *n*-type doped systems.

In the following we examine two possible kinetic processes of an interstitial Mn atom becoming substitutional. These processes share the same initial state with Mn occupying either the  $I_H$  or  $I_T$  sites with a neighboring *n*-type or *p*-type codopant. From our calculation of the total energy of a Ge-supercell with an interstitial Mn and a substitutional codopant as a function of their separation, shown in Fig. 2.2, we find that shorter separation is energetically preferred. Thus, the choice of neighboring Mn/codopant pair configuration is reasonable.

In the first process, denoted as Process I, we consider an interstitial Mn directly exchanging position with its substitutional codopant neighbor. In the final state, the codopant is pushed to an adjacent interstitial site and the Mn atom moves into

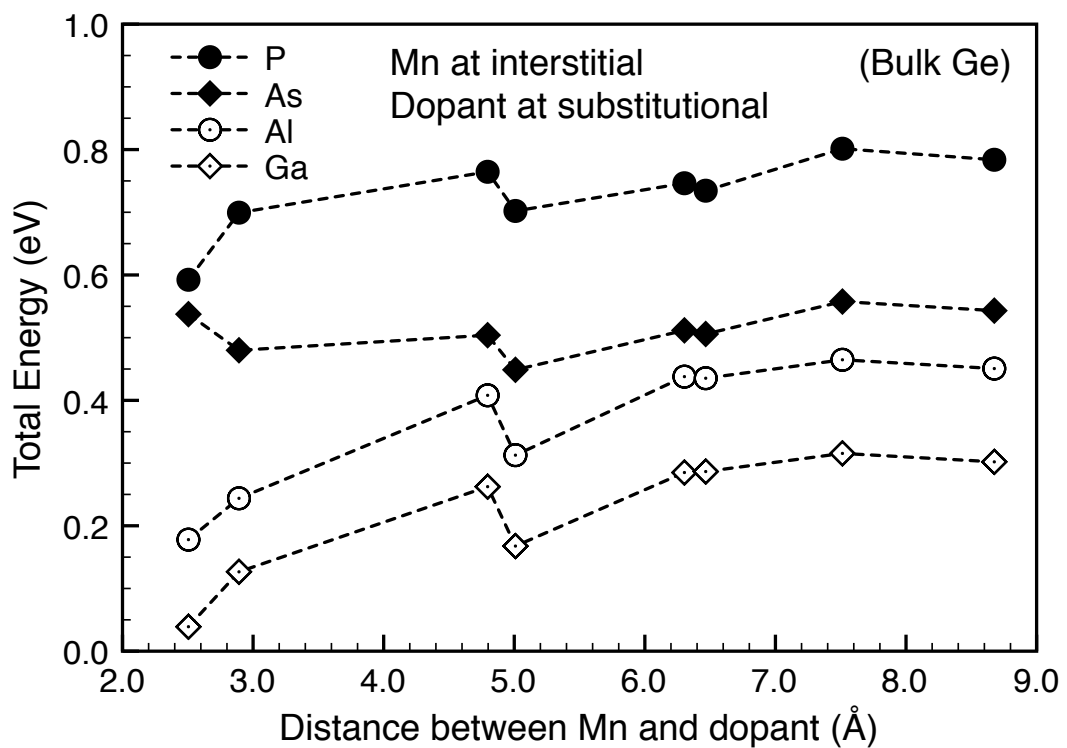


**Figure 2.2:** Calculated relative total energy as a function of the distance between an interstitial Mn and a substitutional codopant in bulk Ge.

**Table 2.1:** Calculated energy differences  $\Delta E = E_f - E_i$  (in eV) between the final and initial states of Process I and Process II.  $\varepsilon_a$  (in eV) is the activation energy for a transition from the initial to final state. Results highlighted in bold correspond to processes for which  $\Delta E$  or  $\varepsilon_a$  or both are  $< 0.8$  eV. All the results are for Mn concentration of 1.56%; results for selected cases with Mn concentration of 0.46% are given in brackets.

Bulk Si				Bulk Ge			
X	$\Delta E = E_f - E_i$		X	$\Delta E = E_f - E_i$		$\varepsilon_a$	
	Proc.I	Proc.II		Proc.I	Proc.II	Proc.I	Proc.II
<b>Si</b>	2.03		<b>Ge</b>	0.82[1.46]			
<b>P</b>	1.46	0.89	<b>P</b>	<b>0.33[0.59]</b>	<b>0.03[0.17]</b>	0.88	<b>0.34</b>
<b>As</b>	1.55	1.09	<b>As</b>	<b>0.42[0.66]</b>	<b>0.05[0.34]</b>	0.98	<b>0.25</b>
<b>Al</b>	1.24	2.05	<b>Al</b>	0.94		1.54	
<b>Ga</b>	1.79	2.43	<b>Ga</b>	1.05		1.52	

the substitutional site left behind, as shown in Fig. 2.3. Table 2.1 summarizes the calculated energy differences  $\Delta E$  between the final and initial states for *n*-type and *p*-type codopants in Si and Ge. We find that only the P or As doped Ge (with  $\Delta E=0.33$  eV and 0.42 eV respectively) can fulfill the requirement that  $\Delta E < 0.8$  eV. However, further examination of the activation energy barriers for incorporation in these two cases gives  $\varepsilon_a = 0.88$  eV and 0.98 eV respectively, which means this process is unlikely to happen in both cases. Moreover, the reverse processes with  $\varepsilon'_a = 0.55$  eV and 0.56 eV, respectively, are more likely to occur.

Nevertheless, there is one possibility for the Mn atom to stay at the substitutional site, that is, the kicked-out codopant atom diffuses away rapidly so that the reverse process cannot happen. This is ruled out by our calculation of the energy of a Mn/codopant pair as a function of their separation, shown in Fig.2.4, which shows that the codopant cannot diffuse away because the energy increases with increasing separation.

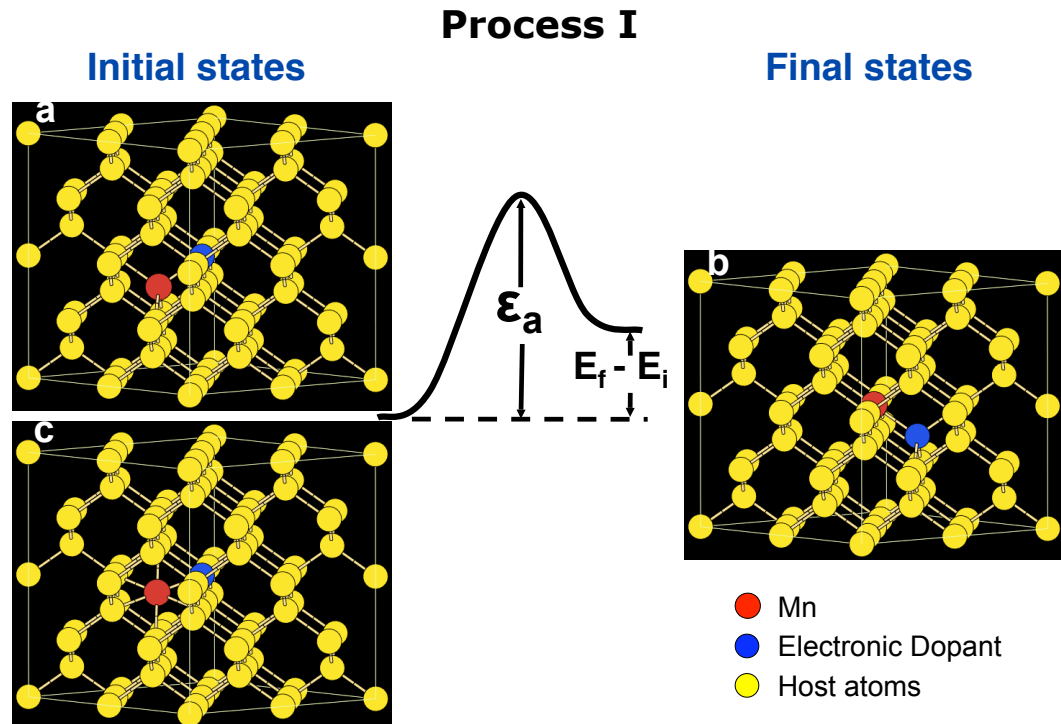


**Figure 2.3:** Atomic structures and schematic energy profiles for Process I: (a) Initial state with Mn in the  $I_T$  position (except for  $n$ -type doped Ge); (b) Final state; (c) Initial state for  $n$ -type doped Ge with Mn at the  $I_H$  position.

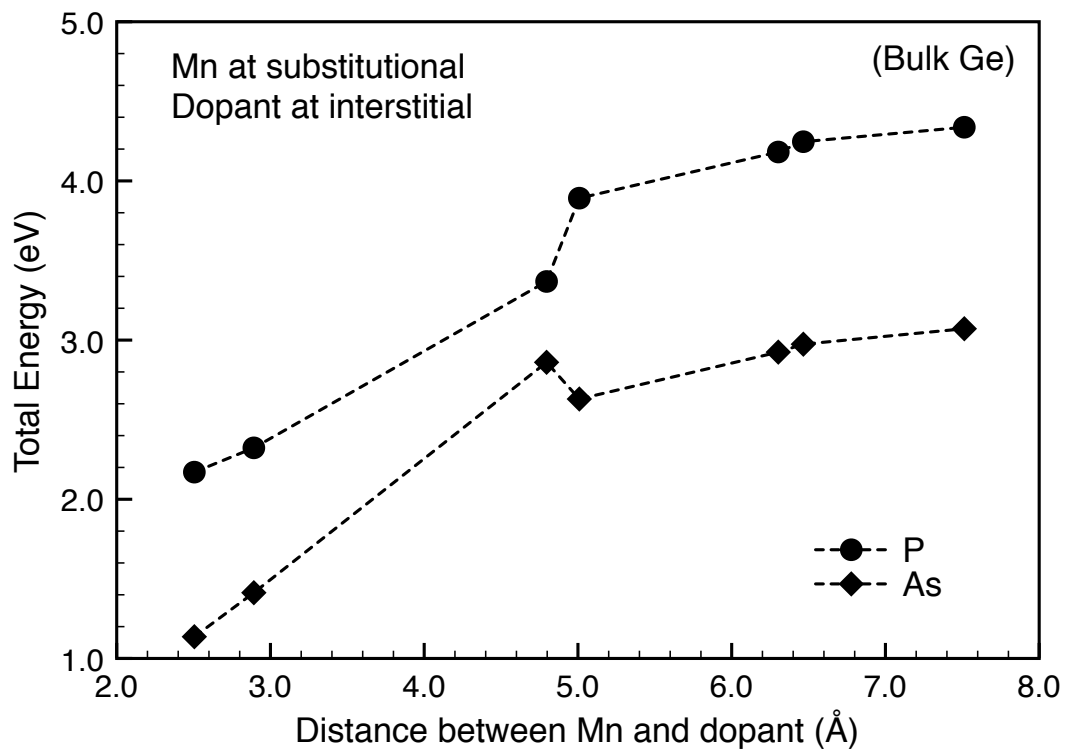


**Figure 2.4:** Calculated relative total energy as a function of the distance between a substitutional Mn and an interstitial *n*-type codopant in bulk Ge.

We then consider a different process (Process II), which starts from the same initial configuration as in Process I, but instead of exchanging with the codopant, the Mn atom now pushes out a host atom next to the codopant to an interstitial site, and then occupies the substitutional site left behind. The final state is shown in Fig. 2.5, in which the kicked-out interstitial host atom, the substitutional Mn and the codopant are nearly collinear. The calculated  $\Delta E$  and  $\varepsilon_a$  for various *n*-type and *p*-type codopants in Si and Ge is also shown in Table 2.1. For *n*-type doped Ge these values are substantially lower than in Process I, and considerably below the threshold value of 0.8 eV. For P and As doped Ge,  $\Delta E$  is actually quite low. Furthermore, the activation barriers  $\varepsilon_a$  for all the three *n*-type codopants is less than 0.4eV. Qualitatively, this substantial change in the energetic and kinetic characters originates from the electrostatic attraction between the Mn atom, which behaves like a *p*-type dopant, and *n*-type codopants. Therefore, Process II, leading to substitutional Mn atoms proximate to *n*-type codopants, is more likely to happen in reality.

To check whether the final state is thermodynamically stable, we calculate the energy difference between interstitial Mn and substitutional Mn defined as

$$\Delta E_2 = (E_{pair} + \mu_{host}) - E_{inter}. \quad (2.2)$$

Here  $E_{inter}$  is the total energy of a Mn/codopant pair, with the Mn sitting at an interstitial site, while  $E_{pair}$  is that with the Mn occupying a substitutional site. The calculated interstitial-substitutional energy difference  $\Delta E_2$  is shown in Table 2.2. Compared to the results without *n*-type codopants, the substitutional Mn in Ge becomes much more stable with the neighboring *n*-type codopant. Moreover, the site preference of Mn in Si is reversed from interstitial to substitutional.

We next calculate the total energy of a Ge-supercell doped by a substitutional Mn/codopant pair at different separations. The trend of the total energy with increasing distance between the Mn atom and the codopant is shown in Fig. 2.6. The interaction between Mn and codopant is attractive for *n*-type codopants (P and

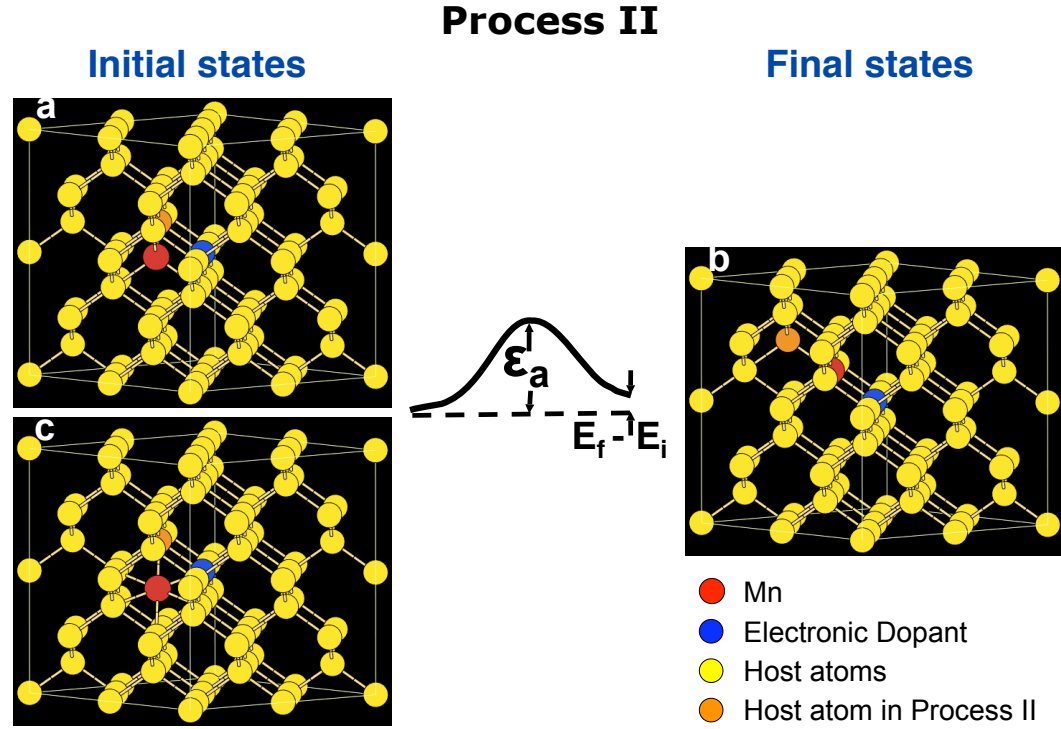


**Figure 2.5:** Atomic structures and schematic energy profiles of Process II: (a) Initial state with Mn in the  $I_T$  position (except for  $n$ -type doped Ge); (b) Final state; (c) Initial state for  $n$ -type doped Ge, with Mn at the  $I_T$  position.

**Table 2.2:** Relative formation energy of substitutional and interstitial Mn in the presence of a neighboring substitutional  $n$ -type codopant, defined as:  $\Delta E_2 = (E_{pair} + \mu_{host}) - E_{inter}$  (in eV). Negative values indicate higher stability of the substitutional configuration over the interstitial. The relative energy of substitutional and interstitial Mn in pure Si or Ge are included for comparison.

	P	As	Undoped
Si	-0.84	-0.87	+0.58
Ge	-1.35	-1.42	-0.63

As) and repulsive for *p*-type codopants (Al and Ga). This suggests that the picture of electrostatic interaction between Mn and codopants that we proposed at the beginning of this section is valid.

In short, we have shown that in the presence of a neighboring *n*-type codopant, the substitutional sites are energetically preferred by Mn atoms to interstitial sites and are kinetically accessible. From now on we will call the *n*-type electronic codopants directly by donors.

## 2.4 Magnetic properties of the codoped systems

### 2.4.1 Magnetic coupling between Mn moments

To see how the donors will influence the magnetic interaction between Mn atoms, we first calculate the magnetic coupling energy of a Mn-Mn pair with different separations, which can be represented by the total energy difference  $\Delta E$  between the antiferromagnetic (AFM) and the ferromagnetic (FM) states of the pair [132–135]. In the present case, each Mn atom has an donor neighbor, which leads to more spatial configurations with the same Mn-Mn distances. To be precise, a substitutional Mn atom has four nearest neighbors, that is, four possible sites for the donor atom, and thus there are 16 possible configurations for a given Mn-Mn distance. The number of nonequivalent configurations for each of 12 Mn-Mn separations in the range 2.4 - 9.5 Å in Si (2.5 - 10.0 Å in Ge) is 2, 6, 16, 4, 7, 16, 4, 7, 16, 10, 7 and 5 respectively, with increasing distance.

With these considerations, our results for Mn/As codoped Ge and Mn/P codoped Si are shown in Fig. 2.7. We first note that in the case of two Mn atoms in pure Ge ((a) and (b) of Fig. 2.7), the behavior of the AFM-FM energy difference  $\Delta E$  is oscillatory between positive and negative values as a function of distance (but monotonically decreasing along different directions, see below). In contrast, the average interaction

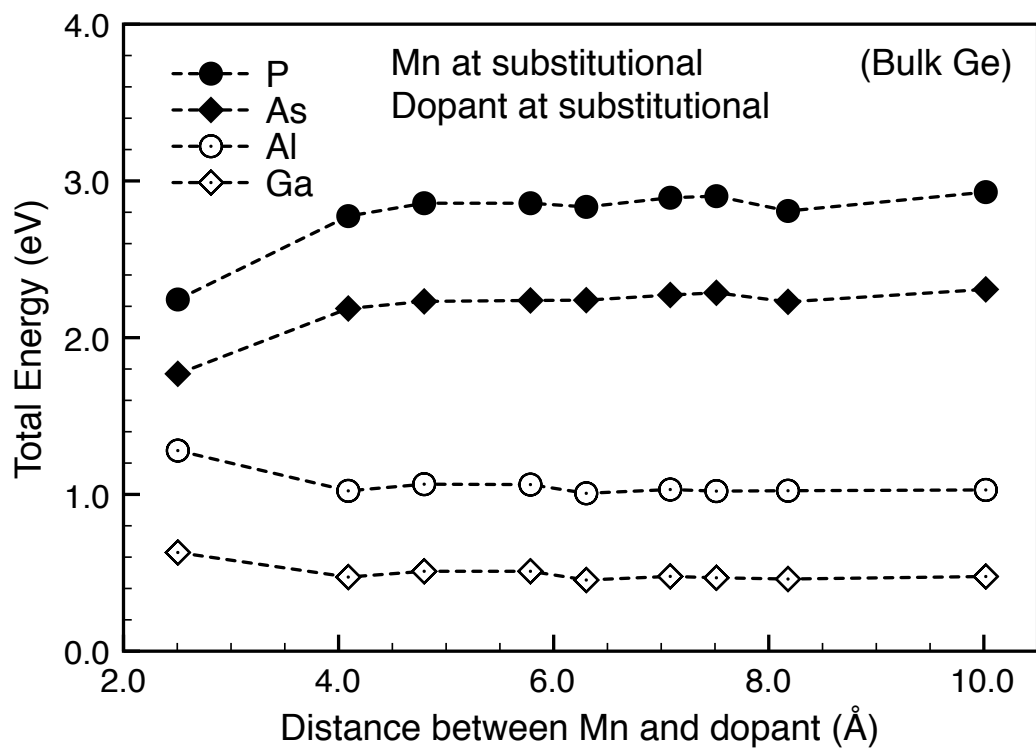


**Figure 2.6:** Relative total energy as a function of the distance between a substitutional Mn and a substitutional codopant in bulk Ge.

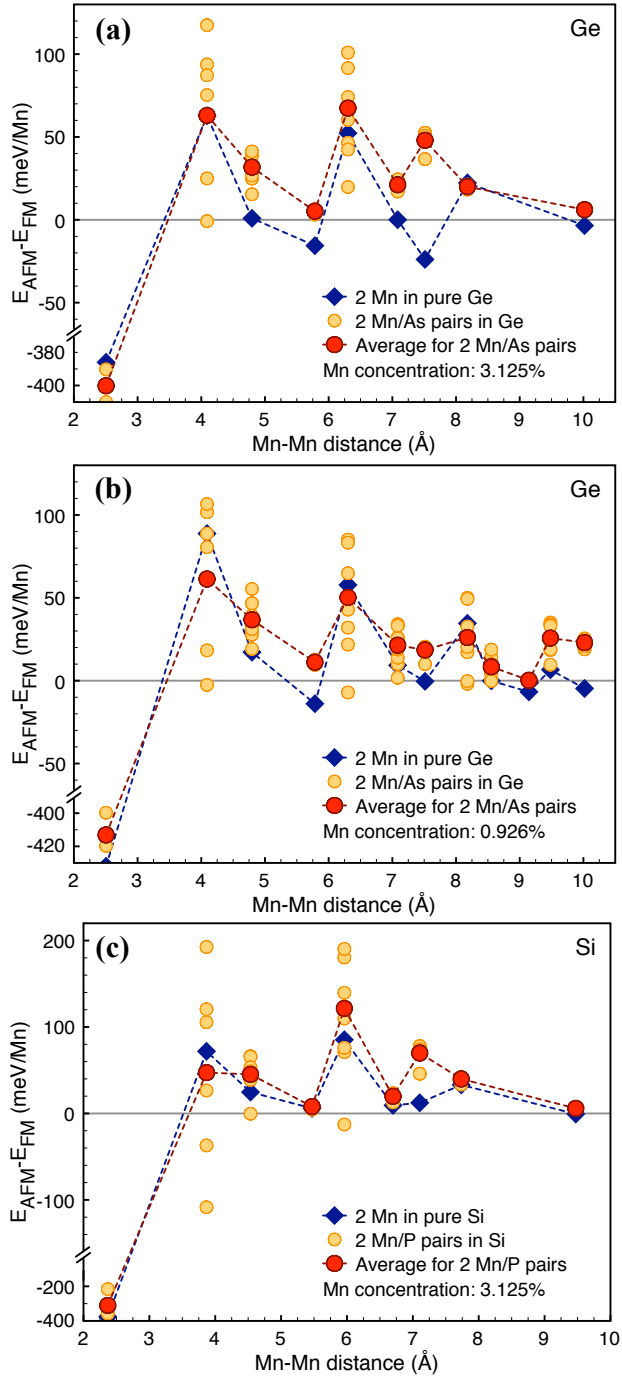


**Figure 2.7:** Total energy difference between AFM and FM states of two Mn atoms versus Mn-Mn separation for Mn/As doped Ge at (a) 3.125% and (b) 0.939% Mn concentration; (c) for two Mn/P pairs doped Si, represented by small orange dots. The large red dots are averages over the small orange dots for a given Mn-Mn distance. For comparison, the results for the systems doped with only two Mn impurities are shown as blue diamonds.

between the two Mn/As pairs in Ge always favors FM coupling except at the nearest-neighbor Mn-Mn distance, and this characteristics does not change with doping level (compare Fig. 2.7(a) of 3.125% Mn and Fig. 2.7(b) of 0.926% Mn). In the case of Si as host, Mn atoms favor FM coupling except for nearest neighbor distance, and this feature does not change upon codoping.

Though usually it is assumed that the hole-mediated magnetic interaction in dilute magnetic semiconductors is RKKY-like, we find that the FM-AFM oscillation displayed in Fig. 2.7 should not be treated as a manifestation of the RKKY interaction [132–135]. Fig. 2.8(a) shows the magnetic coupling between Mn ions along different lattice directions, which is similar to the design in Mahadevan’s work [135], where it is evident that the oscillatory behavior is replaced by monotonic decrease in magnitude. On the other hand, for the doping levels considered here, the period of RKKY oscillation is much larger than the lattice constant [142, 143], as in the case of GaAs. Thus, the oscillation here is merely due to magnetic anisotropy, rather than a manifestation of RKKY-type interaction. In Fig. 2.8(b), we plot the coupling along a close-packed atom chain, which also shows monotonic decrease with distance except for the nearest neighbor value. Moreover, through comparison with Fig. 2.7(b), one can find that the magnetic coupling is strongest along this chain. This finding leads us to suggest that Mn ions in Ge are magnetically coupled through some paths consisting of covalently-bonded Ge atoms, a hypothesis which deserves to be checked by more detailed investigations. And a similar suggestion has been made for Mn doped GaAs [144].

### 2.4.2 Curie temperature

To study the macroscopic magnetic properties of the codoped DMS materials using our *ab initio* results, we turn to the classical Heisenberg model:

$$H = - \sum_{i,j} J_{ij} \sigma_i \cdot \sigma_j, \quad (2.3)$$

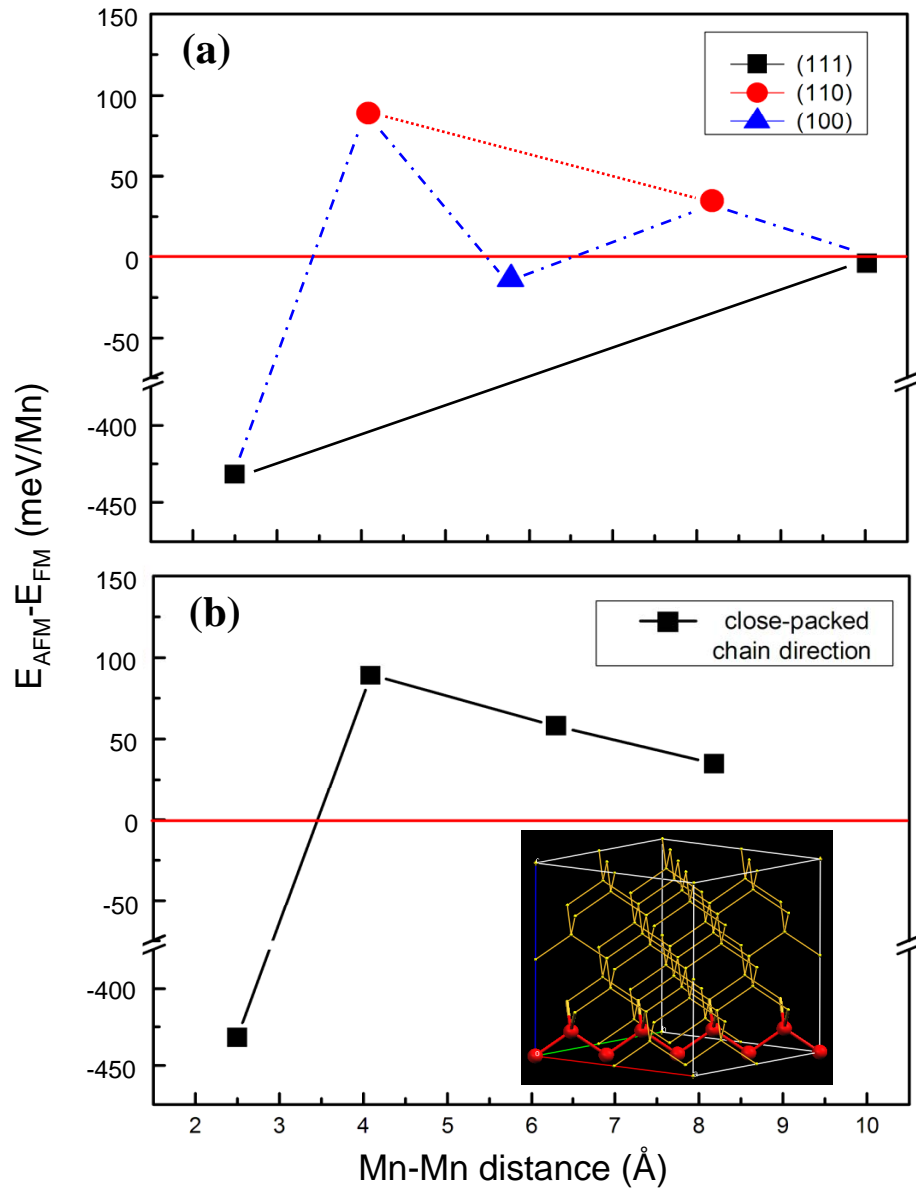


**Figure 2.8:** Magnetic coupling along different crystal directions. Black squares are for the (111) direction, red dots for the (110) direction and blue triangles for the (100) direction. Magnetic coupling along a close-packed chain is illustrated in the inset.

where  $J_{ij}$  is the magnetic coupling constant between moment  $i$  and  $j$ , and  $\sigma_i$  is a unit vector representing the direction of spin  $i$ . Then the AFM-FM energy difference  $\Delta E$  calculated in previous section is given by:

$$\Delta E = E_{AFM} - E_{FM} = 4J_{12}, \quad (2.4)$$

with 1 and 2 the indices of the two moments in the supercell. With given coupling parameters, we then use Monte Carlo simulations to address the statistical mechanics of the DMS systems at finite temperatures. To eliminate finite size effects, the cumulant crossing method [137] is used to determine the Curie temperature. This two-step approach has the distinct advantage over the ordinary mean field approach, that both disorder and percolation effects are naturally and precisely taken into account [145, 146].

We use three supercell sizes:  $8 \times 8 \times 8$ ,  $10 \times 10 \times 10$  and  $12 \times 12 \times 12$ , where the unit length is the edge length of a fcc cube. The number of spin in a supercell is calculated by  $x \cdot 8L^3$ , where  $x$  is the spin concentration. Take the case of  $x = 5\%$  as an example, we have 205, 400 and 691 spins respectively in the three corresponding supercells. In our simulations these numbers are large enough to give a reliable result of  $T_c$ . For disorder averaging in evaluating the Curie temperature, we use 40 randomly generated spin configurations for each supercell size. To check the accuracy we also increase the number of configurations to 100, and no obvious deviations are detected.

Using the *ab initio* coupling parameters for  $Mn_xGe_{1-x}$ , we first find that MC does not yield identifiable  $T_c$  up to  $x = 6\%$  (see below). Nevertheless, after codoping with As, MC shows that the system has high  $T_c$ , as summarized in Fig. 2.9, in which we also include the results from the mean field approximation (MFA) using the formula [147]

$$T_c = \frac{1}{k_B} \cdot \frac{2x}{3} \sum_{i \neq 0} J_{0i}. \quad (2.5)$$

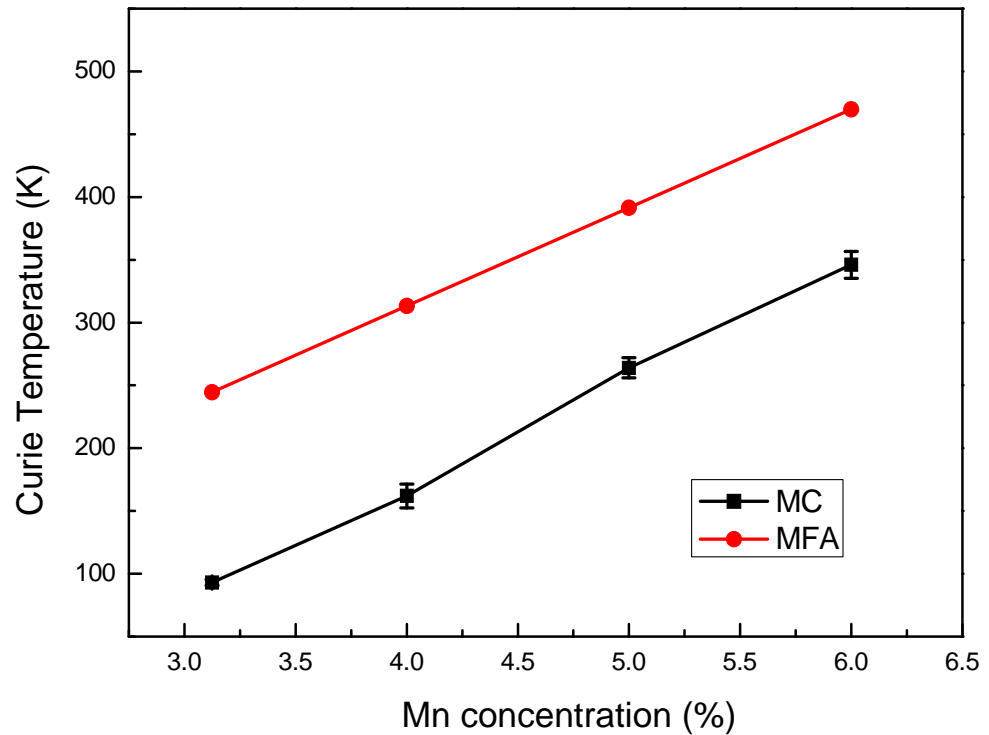


**Figure 2.9:** Comparison between Curie temperatures calculated by the Monte Carlo approach (MC, black squares) and those obtained by the mean field approximation (MFA, red dots).

These results show that the MFA greatly overestimates the Curie temperature, as established before [145–147]. At  $x = 5\%$ ,  $T_c$  is evaluated to be 264K through MC, which is much higher than the 118K of 5% Mn doped GaAs [148]. At the 6% Mn concentration, MC gives a  $T_c$  higher than room temperature. However, considering that  $x=6\%$  is already a relatively high concentration, it may not be appropriate to approximate the magnetic interaction to be pairwise any more. Nonetheless, arsenic doping can still be expected to dramatically change the magnetic properties of Mn doped Ge, namely, from no finite  $T_c$  to a potentially high  $T_c$  DMS material.

The dependence of the Curie temperature on Mn concentration, as obtained from the MC results, is almost linear. This behavior is partly due to the approximation of pairwise interaction we used, meaning that the strength of magnetic coupling does not depend on Mn concentration. The only influence of concentration on  $T_c$  is the average number of magnetic impurity atoms on each coordination shell. Thus, after the configurational average, we expect that the dependence of  $T_c$  on  $x$  resembles the linear one obtained within the MFA (Eqn. 2.5). Another reason for this linearity is that the concentrations we studied are higher than the magnetic percolation threshold of this system [147].

The presence of AFM couplings and the absence of  $T_c$  in the case of pure Mn doped Ge suggests the possibility of a spin-glass ground state for this system. Jaeger *et al.* [149] claimed that at low temperatures  $Mn_xGe_{1-x}$  exhibits spin-glass-like behavior and the critical temperature of the spin-glass phase transition is 12K and 15K, for Mn concentrations  $x = 0.04$  and  $x = 0.2$ , respectively. To examine whether this is the case, we first study the spin-spin correlation function of 5% Mn doped Ge, at  $T = 0.01K$ . The result is shown in Fig. 2.10, along with a plot for Mn/As codoped Ge, for comparison. The correlation function of  $Mn_xGe_{1-x}$  decays very fast with increasing distance and approaches to zero, indicating the absence of FM order even at low temperatures. We then use the Edwards-Anderson spin-glass order

parameter [150], defined as

$$q = [\langle S_i \rangle_T^2]_{av}, \quad (2.6)$$

and calculate the spin-glass cumulant of 5% Mn doped Ge using the two-replica algorithm developed by Bhatt and Young [151]. After averaging over 100-200 configurations for each supercell size, our Monte Carlo simulations yield a transition temperature  $\sim 5\text{K}$ , a value in semi-quantitative agreement with the results of Jaeger *et al.* [149].

## 2.5 Dicussion and conclusion

$\text{Mn}_x\text{Ge}_{1-x}$  has been attractive within the DMS community because of its easy incorporation into the current semiconductor industry. The mechanism of valence hole mediated ferromagnetism for  $(\text{Ga,Mn})\text{As}$  was proposed years ago [71, 142, 152] and has been extensively accepted ever since, but there is still no definitive theory for  $\text{Mn}_x\text{Ge}_{1-x}$  [74]. One major reason is the difficulty of decreasing the percentage of interstitial Mn dopants. The other important point is the hard-to-control inhomogeneity of this system, which has been realized only in recent years. The high Curie temperature formerly reported in  $\text{Mn}_x\text{Ge}_{1-x}$  [116, 153] is now thought to be due to the formation of Mn-rich regions in the host semiconductor [74, 130, 149, 154, 155]. For example, Mn-rich nanodots [156] and nanocolumns [81, 157, 158] in  $\text{Mn}_x\text{Ge}_{1-x}$  have been reported by many experimental groups, and later reproduced in Monte Carlo simulations [159].

Despite the seemingly unavoidable precipitation or spinodal decomposition [155] present during the growth of  $\text{Mn}_x\text{Ge}_{1-x}$  samples, the study on homogeneously doped  $\text{Mn}_x\text{Ge}_{1-x}$  has never stopped. Work by Li *et al.* [130, 154] indicates that the long-range FM order in  $\text{Mn}_x\text{Ge}_{1-x}$  only exists at low temperatures ( $\leq 12\text{K}$ ). Jaeger *et al.* [149] claimed that even at low temperatures  $\text{Mn}_x\text{Ge}_{1-x}$  shows spin-glass-like behavior,

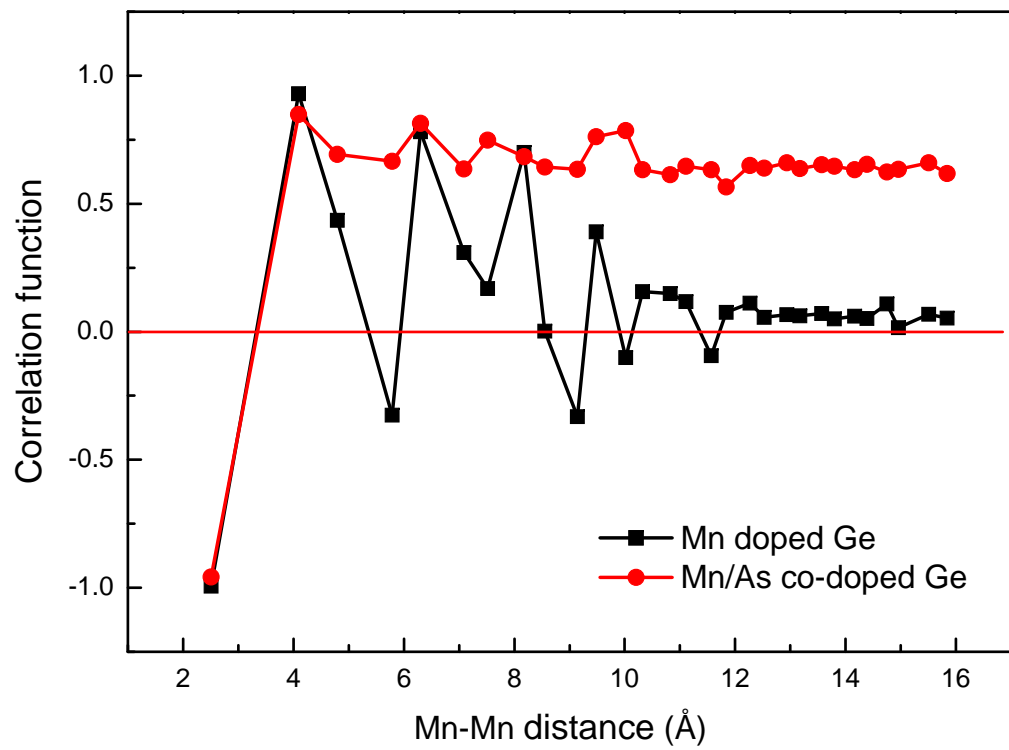


**Figure 2.10:** Spin-spin correlation function obtained from the Monte Carlo simulations.

and proposed that this is due to the intercluster frustration between FM Mn-rich clusters. Zeng *et al.* [122], using a newly developed subsurfactant epitaxy method, successfully grew cluster-free  $\text{Mn}_x\text{Ge}_{1-x}$  samples with a Mn doping level of 0.25%. Surprisingly, this low doping level (by normal DMS standards, where 1% to 5% is typical) led to a Curie temperature as high as over 400 K.

The results in the present work provide a viewpoint that may resolve the seemingly conflicting experimental results discussed above. Specifically, we showed that the magnetic coupling between Mn ions in  $\text{Mn}_x\text{Ge}_{1-x}$  oscillates between FM and AFM with increasing Mn-Mn distance and that homogeneous  $\text{Mn}_x\text{Ge}_{1-x}$  exhibits spin glass behavior. Thus, the FM order observed in experiments could be due to spatially ordered structures, which are formed due to precipitation or spinodal decomposition. The high transition temperatures are expected because of the large concentration of magnetic moments within the clusters. On the other hand, the AFM frustration in this case only manifest itself in the inter-cluster interaction, and thus leads to the spin-glass behavior at low temperatures.

The unexpected high  $T_c$  in Zeng's work requires more discussion. Upon codoping with donor As, the AFM coupling between Mn ions is absent, and a high Curie temperature emerges. We thus speculate that the high transition temperature in this case originates from this codoping effect, and the unexpected donor here is most probably oxygen. Indeed, a recent study on the role of oxygen defects in  $\text{Mn}_x\text{Ge}_{1-x}$  by Continenza and Profeta [160] supports this scenario, namely that oxygen acts as an *n*-type codopant and facilitates the substitutional Mn doping. It is also reasonable to expect a positive influence of oxygen on the Mn-Mn magnetic coupling, which, together with the possible existence of Mn-rich regions, can lead to a high Curie temperature.

Finally, this work suggests that the enhancement of substitutional Mn concentration in group-IV DMS can be achieved in epitaxial growth by codepositing with the donors. More specifically, this codoping method can be integrated in the recently developed subsurfactant epitaxial growth [122], where pure Ge layers epitaxially grow

on a Ge(100) substrate pre-covered with a submonolayer of Mn. During the growth process, the Mn atoms tend to diffuse upward to the subsurface layer, as predicted in a previous theoretical study [161]. When the growth is slow enough, a small fraction of the Mn atoms can be trapped in substitutional sites, which leads to homogeneous substitutional Mn doping with all the interstitial Mn floating at the subsurface layer. However, the resulting Mn concentration is still pretty low (0.25%). Here we propose that by codepositing Ge with another donor, with very low depositing rates, the growth front could mimic the subsurfactant growth mode, but with more efficient substitutional trapping of Mn. The Mn trapping rate can be controlled by changing the concentration of the donor. Experimental confirmation of this codoping scheme is highly desirable.

In conclusion, our *ab initio* DFT calculations show that in DMS materials *n*-type electronic codopants (donors) can serve to enhance the substitutional doping of *p*-type magnetic dopants such as Mn in the host group IV semiconductors Si and Ge. The donors suppress to a large extent the charge and magnetic-moment compensating effects from interstitial Mn, which is detrimental to FM order. We calculate the magnetic coupling between moments associated with Mn atoms and find that the coupling oscillates between ferromagnetic (FM) and antiferromagnetic (AFM) with increasing Mn-Mn distance in the Mn-doped Ge. Whereas in As/Mn *n-p* codoped Ge the coupling values at Mn-Mn separations up to the 12th coordination shell are all FM, except for the nearest-neighbor one. We find that the FM-AFM oscillatory behavior in  $Mn_xGe_{1-x}$  is due to anisotropy rather than being the result of a RKKY-type interaction. The magnitude of Mn-Mn ferromagnetic couplings is also enhanced upon codoping donors. Our Monte Carlo simulations, using magnetic coupling parameters obtained from the *ab initio* calculations, indicate a high Curie temperature in Mn/As-Ge of 264K at 5% Mn doping. On the other hand, no FM order is observed in  $Mn_xGe_{1-x}$  (without codoping) as Mn concentration ranges from 3.13% to 6%. Thus, the homogeneously doped  $Mn_xGe_{1-x}$  is most likely a generic spin glass, with a spin-glass transition temperature of 5K at 5% doping, also obtained

from our Monte Carlo simulations. Accordingly, we suggest that the high Curie temperature observed experimentally in  $\text{Mn}_x\text{Ge}_{1-x}$  is either due to the formation of Mn-rich spatially ordered regions, or to *n-p* codoping effects from the *n*-type oxygen impurities, or a combination of both.

# **Chapter 3**

## **Graphene: Growth and Functionality**

### **3.1 Contrasting Behavior of Carbon Nucleation in the Initial Stages of Graphene Epitaxial Growth on Stepped Metal Surfaces**

#### **3.1.1 Introduction**

Since its first isolation, graphene has attracted rapidly growing research interest because of its various intriguing properties and potential applications in future electronics [162, 163]. However, a route towards scalable mass production of quality graphene for industrial use is still lacking. Among many newly developed techniques, epitaxial growth of graphene on metal surfaces offers a promising avenue [40–53]. Large size and good quality graphene samples have been prepared on various metal surfaces [40–46, 164]. The success in transferring the epitaxial graphene grown on Ni and Cu surfaces to insulating substrates makes this method even more attractive [44, 45]. Additionally, various aspects about the growth mechanisms of graphene have been revealed in recent studies of representative carbon/metal systems. For

example, the growth of graphene on Ir(111) and Ru(0001) substrates is fed by the supersaturated two-dimensional (2D) gas of carbon adatoms, and a multi-carbon cluster attachment mechanism has been proposed [47–49], with minimal effect of hydrogen [48, 50]. On a Cu substrate, graphene is found to grow through a surface adsorption process, while on Ni it is by carbon segregation or precipitation [51].

Despite these achievements, very little has been revealed about the growth kinetics, especially in the initial nucleation stages of carbon adatoms. Experimentally it has been found that carbon nucleation starts from the lower edges of steps on Ir(111) [164] and Ru(0001) [47] surfaces, but it is still unclear why nucleation at the step edges is preferred over terraces. Previous studies of C nucleation on stepped metal surfaces were primarily based on consideration of preferred binding sites of C monomers. For example, the observed C nucleation at the step edges on Ni(111) was attributed to the strong binding of C monomers to the lower step edges [165, 166]. Determination of nucleation sites is crucial in improving both the quality and quantity of epitaxial graphene. In the growth of graphene on Ru(0001), multiple nucleation on terraces can easily degrade the quality of graphene because defects will form at the interfaces of separately nucleated graphene islands [48]. In graphene growth on Ir(111), the nucleation sites must not be too sparse, because otherwise rotated graphene domains are more likely to grow at the boundaries of the major phase of the islands that are aligned with the substrate [52, 53]. Quantity-wise, in order to eventually achieve mass production for industrial applications, it is more desirable for nucleation of graphene islands to take place over the entire substrate rather than only at the edges of preexisting steps. In light of these aspects, a general guiding principle of determining the nucleation sites on different substrates will be highly beneficial.

In this section, we present a comparative study of the energetics and kinetics in the initial stages of epitaxial graphene growth on three representative stepped metal surfaces, using first-principles calculations within density functional theory (DFT). We find the traditional monomer-based picture of epitaxial growth cannot explain the experimentally observed step edge nucleation of C on Ir(111) and Ru(0001),

because the steps on these substrates cannot effectively trap C monomers. Instead, a novel dimer-based picture is proposed, in which the substrate steps can readily facilitate the formation of C dimers at their lower edges. Moreover, the interaction between two adatoms is found to be repulsive on flat Ir(111) and Ru(0001), making ad-dimer formation improbable, whereas it is attractive on flat Cu(111), leading to easy ad-dimer formation. We rationalize these contrasting kinetic behaviors of carbon adatoms based on the delicate competition between the C-C bonding and C-metal bonding, and generalize this picture to predict the initial growth stages of graphene on different metal substrates.

### 3.1.2 Methods

In our studies, we use the Vienna *ab initio* simulation package (VASP) [125] with PAW potentials [126] and the generalized gradient approximation (PBE-GGA) [128] for exchange-correlation potential. All the metal surfaces are modeled by a 6-layer slab, with atoms in the lower 3 layers fixed in their respective bulk positions. We use (322) and (332) surfaces to model the stepped Ir(111) and Cu(111) surfaces, which contains  $\{100\}$  (A-type) and  $\{111\}$  (B-type) microfacets, respectively. The stepped Ru(0001) surface is modeled by a vicinal surface with its normal along the  $\langle 0\bar{1}110 \rangle$  direction, which contains alternating A- and B-type steps. All the terrace widths are  $\sim 11\text{-}12 \text{\AA}$ . The k-point mesh used in the calculations is  $1 \times 3 \times 1$  for stepped Ru(0001), and  $3 \times 3 \times 1$  for all the other cases [167]. We use the climbing image nudged elastic band (CINEB) method [136] to determine the energy barriers of the various kinetic processes.

### 3.1.3 Dynamics and kinetics of single carbon atoms on metal surfaces

We first study the adsorption and diffusion of isolated carbon atoms (monomers) on flat metal surfaces. We considered the fcc hollow (with an atom directly below in the

third layer), hcp hollow (with an atom directly below in the second layer), subsurface octahedral, and subsurface tetrahedral sites for a given system. The most stable adsorption sites and the corresponding binding energies, defined by  $\Delta E_C = E_{C/\text{subst}} - E_C - E_{\text{subst}}$ , on Ir(111), Ru(0001) and Cu(111) are hcp (-7.44 eV), hcp (-7.66 eV) (in agreement with previous calculations [47, 48]), and subsurface octahedral (-5.66 eV), respectively. The stronger binding on the other two substrates and the weaker binding on Cu(111) are consistent with the *d*-band model [26]. On Ir(111) and Ru(0001), the energy in the metastable fcc sites are 0.25 eV and 0.74 eV higher, respectively. On Cu(111), the metastable sites (fcc, hcp, bridge, subsurface tetrahedral) are less stable than the subsurface octahedral sites by  $\sim$ 0.6 eV. The surface diffusion barriers ( $\varepsilon_a$ ) of a C monomer between a stable and the nearest metastable states are 0.75 eV and 0.87 eV on Ir(111), Ru(0001), respectively. On Cu(111), the calculated C monomer diffusion barrier (0.55 eV) is for hopping between octahedral subsurface sites via a tetrahedral subsurface site.

We next investigate the adsorption and diffusion of single C adatoms at step edges of Ir(111) and Ru(0001). As shown in Fig. 3.1, the calculated binding energies at step edges are not much larger than those on flat surfaces. The same is true for the kinetic barriers. Considering the high growth temperatures in experiments ( $\sim$ 1000 K), we arrive at the conclusion that the substrate steps do not serve as effective traps for single C adatoms. The absence of large step-crossing barriers and deep wells at step edges, in contrast to the traditional Ehrlich-Schwoebel (ES) picture [14, 15, 168], is attributed to the difference in passivation of the substrate atoms near step edges by C adatoms [169]. We also note that when compared with the cohesive energy of carbon atoms in freestanding graphene (-7.94 eV, in agreement with [47, 170]) or graphene adsorbed on metal surfaces (slightly higher, [171]), the above energy values for C monomer binding on terraces or around the steps suggest that there is always a strong driving force on the C monomers toward growing into larger graphene sheets if such carbon islands or adsorbed graphene sheets could first be formed on the surfaces.

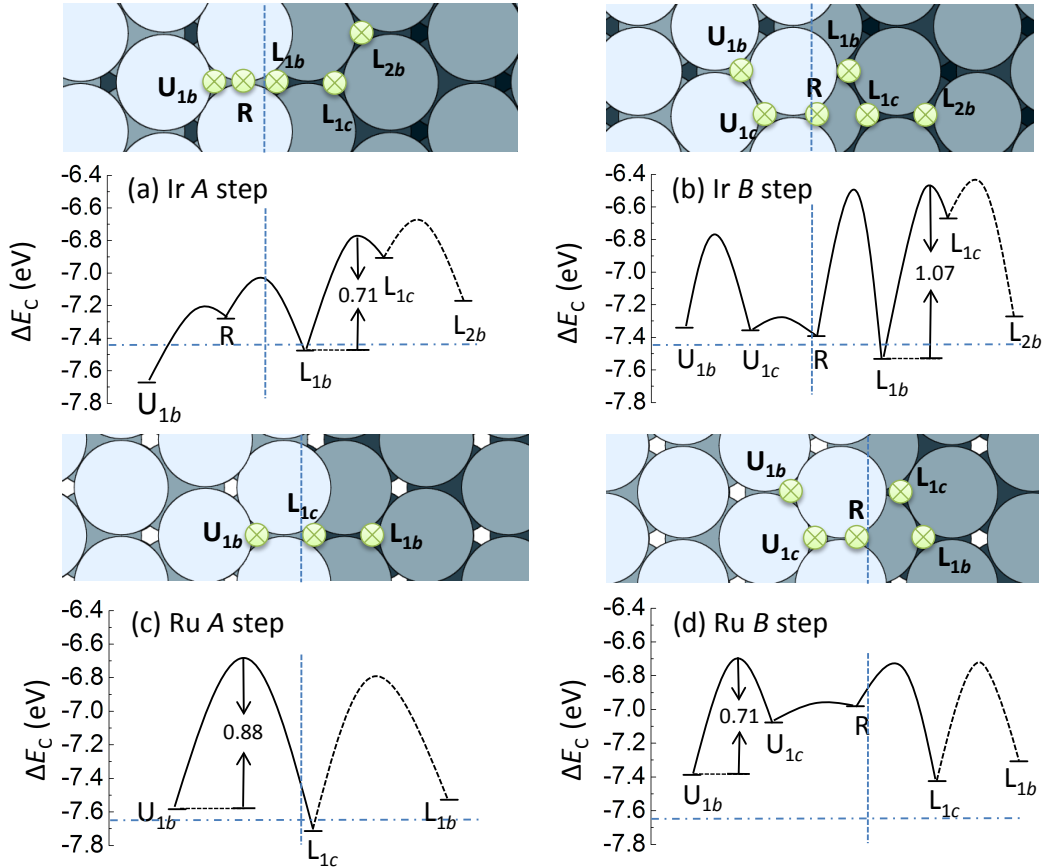


**Figure 3.1:** Top views of adsorption sites and binding energies of a C adatom around (a) Ir A-step, (b) Ir B-step , (c) Ru A-step, and (d) Ru B-step. The solid curves represent C diffusion profiles. The vertical dashed line represents the position of step edge, and the horizontal dot-dashed line indicates the C binding energy on flat surfaces. Definition of labels: U - upper terrace, L - lower terrace, R - ridge site where C only binds to atoms in the ridge of a step edge; b - hcp site, c - fcc site.

### 3.1.4 Formation of carbon dimers on metal surfaces

Where should nucleation of carbon adatoms occur if they are not effectively trapped anywhere on the substrates of Ir and Ru? The above results indicate that knowing the behavior of non-interacting single carbon adatoms is insufficient to answer this question. Specifically, since carbon adatoms are known to form strong covalent bonds with one another when they nucleate to form graphene, it is necessary to take the carbon-carbon interaction into account. We therefore next study the formation of C dimers as the first step of nucleation on the metal substrates. Fig. 3.2 shows the trend of binding energies of two carbon adatoms on the flat metal surfaces, defined by  $\Delta E_{2C} = E_{2C/\text{subst}} - 2E_C - E_{\text{subst}}$ , as a function of the separation distance. One can immediately notice that on Ir(111) and Ru(0001) the formation of C dimers is energetically unfavorable, but on Cu(111), dimers are much more stable than separate C adatoms by over 2 eV. Moreover, the energy barrier of forming a dimer for two neighboring C adatoms is only 0.32 eV on Cu(111), which is much smaller than those on Ir(111) (1.37 eV) and Ru(0001) (1.49 eV). These findings suggest that on Ir(111) and Ru(0001), C adatoms are mutually repulsive and cannot form dimers, whereas on Cu(111) they strongly attract each other, leading to the formation of dimers and larger islands.

We next show that, even though on flat Ir and Ru surfaces C dimerization is not preferred, it can be readily facilitated by the step edges. In Fig. 3.3 we plot the binding energies of two C adatoms on stepped metal surfaces with their separation. In all cases, there is a deep potential well upon the formation of a C dimer at lower step edges. This exceptional tendency towards dimerization at substrate step edges is related to the special local bonding geometry of a C dimer at those sites, which is shown in Figs. 3.3 (a) and (b). By comparing those with a C dimer on flat surfaces shown in the inset of Fig. 3.2, one can observe that the bonds in the latter case are severely twisted. Since the covalent bonds are highly directional and it is energetically

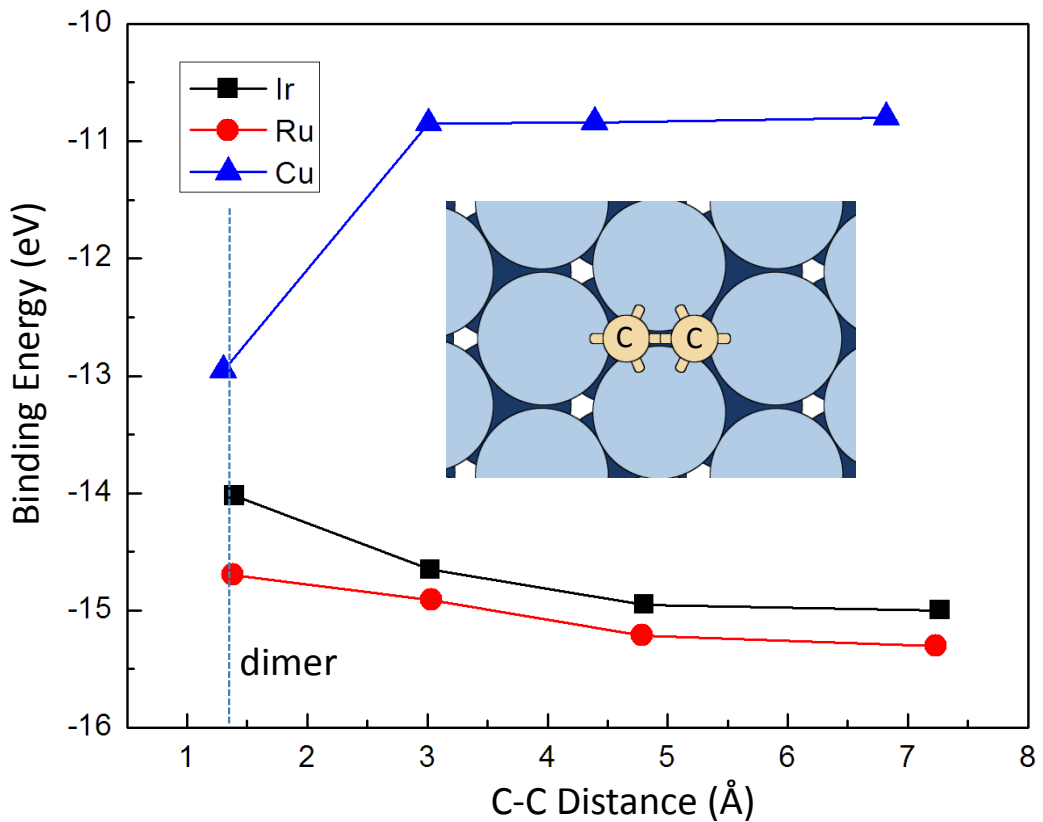


**Figure 3.2:** Binding energies of two C adatoms on flat metal surfaces as a function of their separation distance. Data points around the vertical dashed line correspond to the formation of C dimers. Inset shows the top view of a C dimer on a close-packed metal surface. Kinetic barriers are not shown.

costly to change the relative bond angles, the relaxation of the covalent bonds by the step geometry leads to the extra stability of the C dimers.

Above results have shown that on Ir(111) and Ru(0001), nucleation of C adatoms first occurs at substrate step edges, in agreement with existing experiments [47, 164]; whereas on Cu(111), our results predict that C adatoms should nucleate everywhere on the surface. We note that, once formed on the flat surface of Cu(111), a carbon dimer can also diffuse relatively freely with an activation barrier of  $\sim 0.5$  eV [170] to reach a step edge, where it binds more strongly (see Figs. 3.3 (g) and (h)). However, at desirable growth conditions, such C dimers can collect additional carbon monomers or coalesce to form larger carbon fragments, and quickly lose their mobility, again leading to fast growth of graphene everywhere on Cu(111).

The contrasting behavior of the interacting C adatoms on flat close-packed Ir(111), Ru(0001), and Cu(111) surfaces can be attributed to the competition between the C-C and C-metal interactions. The C-C bond lengths of carbon dimers on flat Ir(111), Ru(0001) and Cu(111) surfaces are 1.397 Å, 1.376 Å, and 1.299 Å, respectively, which are very close to the length of a C-C double bond (1.34 Å). A double bond requires two bonding electrons from each C adatom, but one carbon adatom has only four valence electrons and three nearest metal neighbors on the surface. So intuitively, the formation of a C dimer will weaken the C-metal bonding because of less bonding electrons. Therefore, if the C-metal bonds are very strong, which is the case of Ir and Ru, the dimer formation is not energetically favorable. Conversely, in the case of Cu where C-metal bonding is weak, formation of a dimer is preferred for two C adatoms.

### 3.1.5 Generalization to other metal substrates

Next we show that the above picture is not limited to the three representative cases, but can be generalized into a simple guiding principle. To this end, we compare the binding energies of C adatoms and C dimers on the close-packed surfaces of various transition metals, as shown in Fig. 3.4. It is apparent that the weaker the

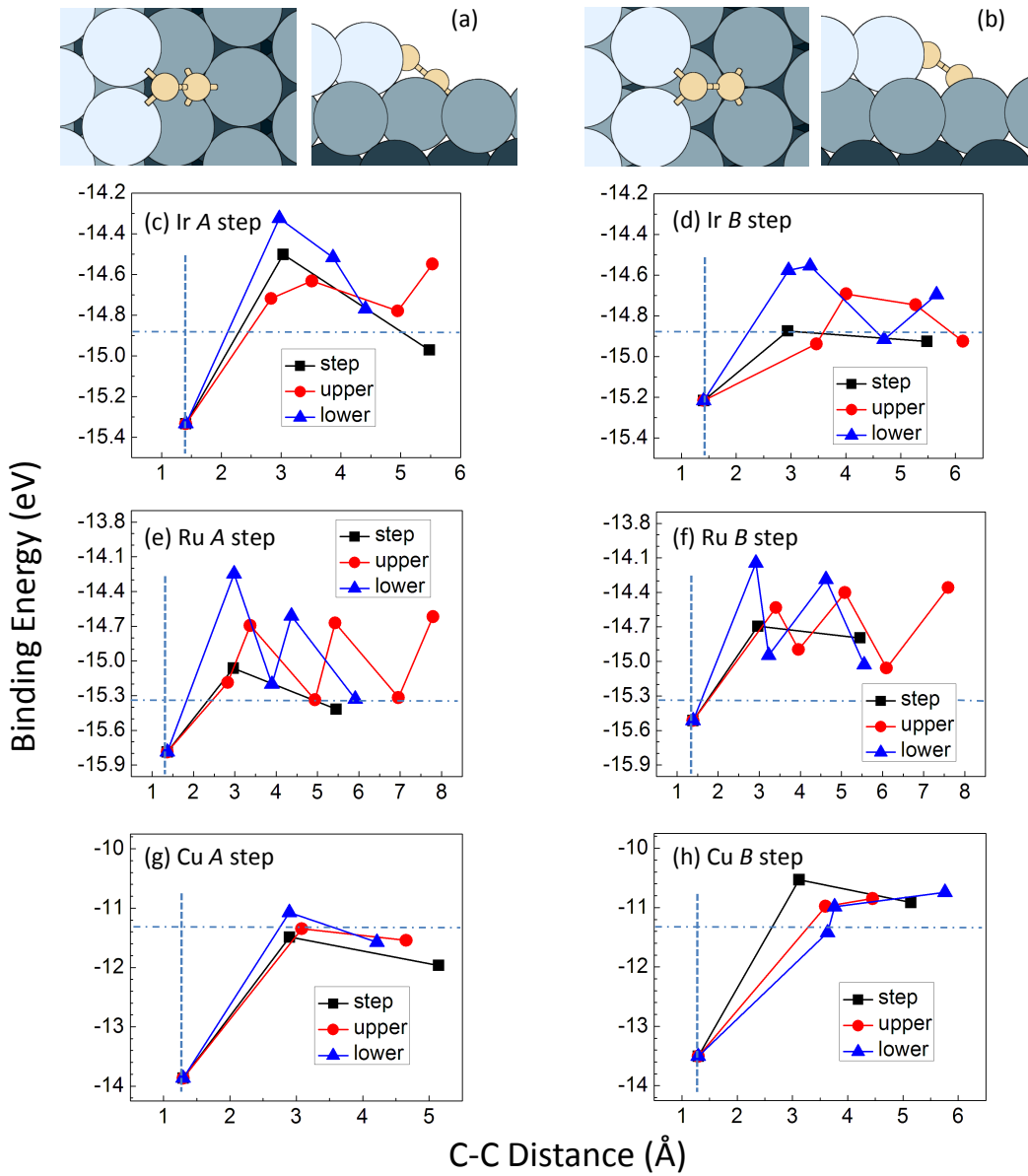


**Figure 3.3:** (a) and (b) Top- and side-view of the most stable configuration of a C dimer at the lower edge of a (a) A-step and (b) B-step. (c-h) Binding energies of two carbon adatoms with one C atom fixed at the lower step edge and another placed in stable or metastable sites on upper terraces, lower terraces, or at the lower step edges, with increasing distances from the first adatom. Horizontal axis is their separation distance. Vertical dashed line in each panel shows where a C dimer is formed, and horizontal dot-dashed line shows the binding energy of two separate C adatoms on flat surfaces.

C-metal interaction is, the more preferred the C dimers are. In all the cases of noble metals, which have closed *d*-shells and strong free-electron like surface states, C dimerization is preferred. The dimer-preferred and dimer-not-preferred systems are essentially separated by the vertical dashed line corresponding to the energy of a C-C double bond (-6.33 eV). The deviation from this trend may be, for example, because of the variation in bonding nature or geometrical effects. Based on the results presented earlier and the prototypical nature of the systems we have studied therein, we can further conclude that for those systems in which C dimers are not preferred on terraces, C nucleation should first occur at substrate step edges. Thus, our study makes it possible to predict where the initial nucleation should happen armed solely with the knowledge of the binding energy of C adatoms to the metal substrate.

This generic principle can lead to many strong predictions. For example, in the strong C-metal binding regime, a flat substrate with scarce steps may not result in growth of quality graphene because of the simultaneous nucleation at multiple sites on the terraces [47], a somewhat counterintuitive conclusion. In the weak C-metal binding regime, epitaxy on single-crystal flat Cu(111) is more likely to yield graphene with the desired high quality and potential mass production, because C adatoms prefer to nucleate everywhere, and the mismatch of graphene with Cu substrate is very small.

### 3.1.6 Conclusion

In summary, we have performed a comparative study of the energetics and kinetics of carbon adatoms on stepped Ir(111), Ru(0001) and Cu(111) surfaces, with intriguing predictions. The present work establishes that one must go beyond the standard monomer-based nucleation and growth picture by explicitly considering where a C-C dimer would prefer to nucleate in uncovering the underlying atomistic mechanisms of growth of carbon nanostructures on metal surfaces, and the predicted behaviors

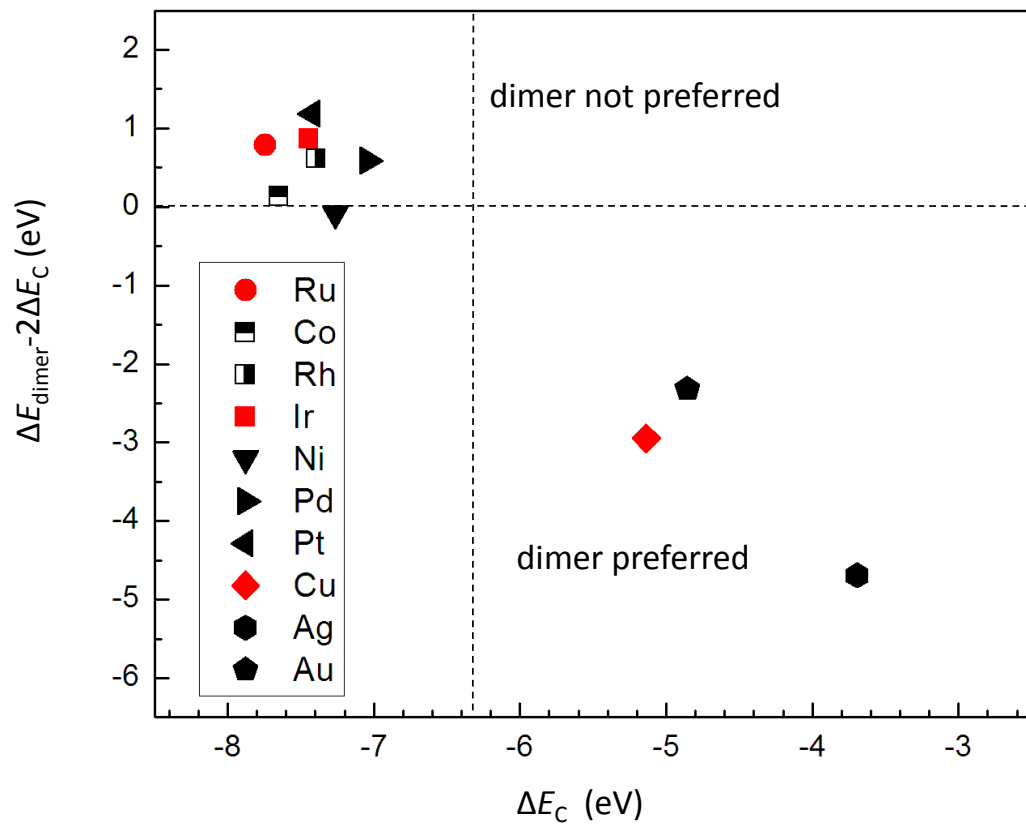


**Figure 3.4:** Binding energy difference between a C dimer ( $\Delta E_{\text{dimer}}$ ) and two separate C adatoms ( $2\Delta E_{\text{C}}$ ) with respect to  $\Delta E_{\text{C}}$  on close-packed transition metal surfaces. Vertical dashed line corresponds to the binding energy of a C-C double bond (-6.33 eV).

in the early stages of epitaxial graphene growth are expected to be instrumental in achieving mass production of high quality epitaxial graphene.

## 3.2 Stable Carbon Nanoarches in the Initial Stages of Epitaxial Growth of Graphene on Cu(111)

### 3.2.1 Introduction

As discussed in the previous section, epitaxial growth of graphene on metal substrates is one of the most promising approach for mass production of quality graphene. Especially, growth of graphene by chemical vapor deposition (CVD) on Cu foils and Cu(111) single crystal [45, 51, 55–57] has been demonstrated to produce up to hundreds of square inches of reasonable quality graphene sheets (monolayer with regions of bi- and trilayer) with high electron mobility and superb thermal conductivity [57]. The high yield of reasonable quality graphene and the relative cheapness of Cu may make Cu an ideal catalyst for graphene production. As for the growth mechanism, graphene growth on Cu was shown to proceed by a surface catalyzed process rather than a precipitation or segregation process because of the low solubility of C in Cu [51]. Despite these achievements, graphene samples grown on Cu still display considerable imperfections such as wrinkles and grain boundaries, indicating significant room for improvement of the growth process and the need for a deeper understanding of the nucleation of graphene monolayers.

Nucleation from carbon monomers to dimers [54, 170] is a crucial step in the formation of larger graphene islands. Previous density functional theory (DFT) calculations have shown that a division can be made between metals for which dimers form on the terraces and those for which dimers are only energetically favored to form at step edges [54]. Cu(111) is one of the metal substrates predicted to belong to the former category. Also, experiments combined with theoretical calculations revealed dome-shaped graphene islands for the sizes of  $N = 13 - 54$  carbon atoms on Ir(111)

[50], which is expected to be a common feature in graphene epitaxial growth on other metal substrates. The present work intends to bridge the gap between carbon dimers and larger islands. In this section, we will show the energetic preference for the formation of stable one-dimensional (1D) carbon nanoarches consisting of 3–13 atoms when compared to two-dimensional (2D) compact islands of equal sizes through a systematic first-principles study. The monatomic 1D carbon chains have been long pursued due to their predicted exceptional physical and chemical properties [172–174]. However, little has been experimentally demonstrated mainly due to the lack of a reliable and effective fabrication method [175–179]. The present work suggests that such 1D carbon chains can be formed via self-assembly on Cu(111) substrates.

### 3.2.2 Methods

Calculations were conducted using the Vienna *ab initio* Simulation Package (VASP) [125] implementation of DFT with projector-augmented wave [126, 127], Perdew-Burke-Ernzerhof [128] (PAW-PBE) pseudopotentials and a  $3 \times 3 \times 1$   $k$ -point mesh. For smaller clusters (three to six atoms), we used a  $5 \times 6$  supercell with six atomic layers. For larger compact islands we reduced the number of atomic layers to five and for larger chains we used a  $4 \times 8$  supercell (long axis along the chain’s linear dimension) with five atomic layers. Comparisons between the five- and six-layer supercells for the same cluster showed a negligible difference in formation energy and structure. Carbon atoms were placed on various adsorption sites (atop, hcp, and fcc) depending on the structure, and optimized atomic geometries were obtained when the forces on all the unconstrained atoms were smaller in magnitude than  $0.02 \text{ eV}\text{\AA}$ . The formation energy per atom is calculated by the formula:  $E_{form} = (E_{tot} - E_{Cu(111)} - N \times E_{C,alone})/N$ , where  $E_{tot}$  is the total relaxed energy,  $E_{Cu(111)}$  is the energy of the relaxed Cu(111) surface alone, and  $E_{C,alone}$  is the energy of an isolated carbon atom.

### 3.2.3 Energetic preference of linear carbon nanoarches for small clusters

Results for the energetics of the relaxed 1D and 2D structures are summarized in Fig. 3.5. For carbon trimers (3C) we calculated a triangle and a linear chain. For the chain we relaxed for several starting configurations, each consisting of three adjacent binding sites. There are four nearly degenerate metastable configurations indicating that the specific binding sites are not likely to significantly affect our results. All the linear configurations are heavily favored over the triangle. For 4C-13C clusters we compared one linear configuration with one compact. For 4C and 5C a rhombus and a pentagon, respectively, were used for the compact clusters. For 6C and larger, configurations of hexagonal rings were used for compact structures. There is a clear trend of decreasing difference between the formation energies per atom of the compact and linear structures. However, this trend does not appear for 4C and 8C. For 4C it is likely because forming a rhombus requires a carbon atom close to an atop site, which is a heavily unfavorable binding site. For 8C, the deviation from the trend is likely due to a lack of completion of a hexagonal carbon ring. In all the cases considered, a linear configuration is favored over a compact one. Here we note that since *sp*-hybridized carbon atoms prefer linear configuration, isolated ring structures with many highly bent divalent carbon atoms are highly unfavorable. Because C-Cu binding is weak, the dangling  $\sigma$  bonds at the divalent bent vertices of isolated rings cannot be sufficiently saturated, and the energy required to bend the *sp* carbon atoms cannot be provided. This is in contrast to the situation on Fe or Ni surfaces, where carbon-metal binding is stronger. Another observation from Fig. 3.5 is longer chains are energetically more favorable than shorter chains, which is also because of the much weaker C-Cu binding at the ends of the chains compared to the C-C binding in the middle of the chains.

Aside from energetics, Fig. 3.5 also depicts several distinct structural aspects of the clusters: the relaxed linear clusters form nanoarches with increasing arch height

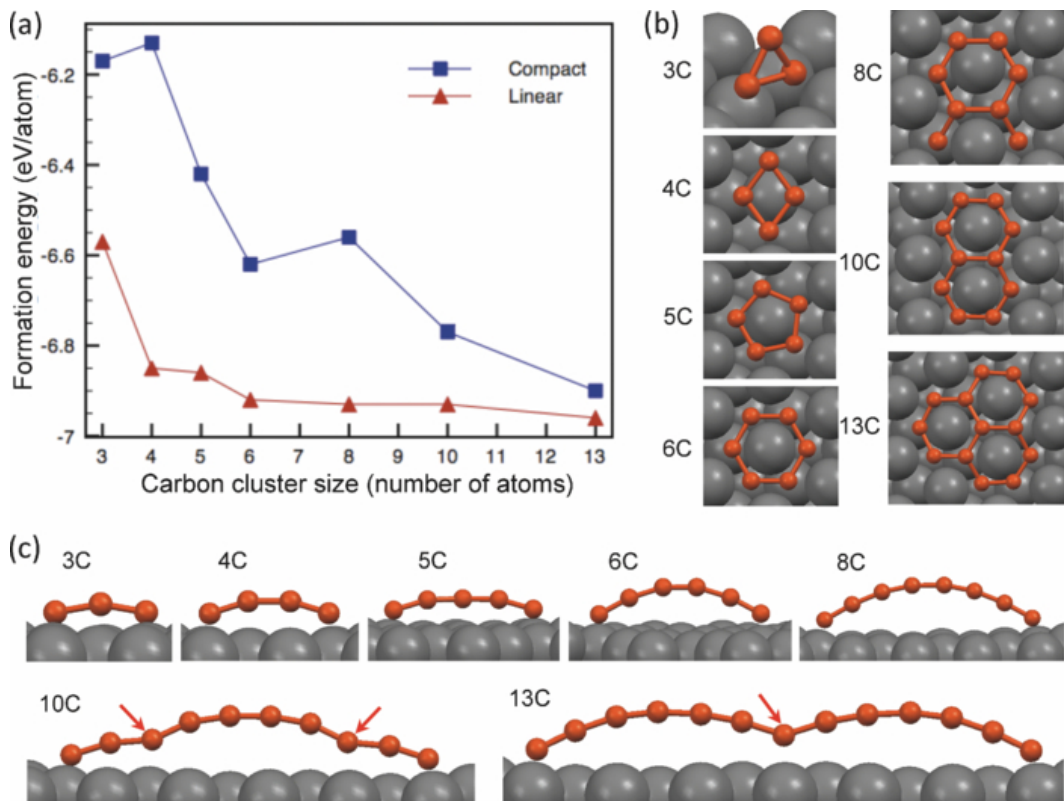


**Figure 3.5:** (a) The formation energies per carbon atom of 1D linear chains and 2D compact islands consisting of 3-13 carbon atoms on Cu(111). (b) Top views of the relaxed 2D compact structures on Cu(111). Small orange and large gray balls represent C and Cu atoms, respectively. (c) Side views of the relaxed 1D nanoarch structures on Cu(111). Red arrows indicate the points where the arch collapses.

from 3C to 8C, while at 13C a double arched structure is formed, with 10C being intermediate between these two shapes. An explanation for a single arch to double arch transition may be furnished by an analogy with a previous molecular dynamics study comparing Au and Ni atom chains on an Au(110) surface [180]. This earlier study found that, for Ni, for which a mismatch between the binding site distance and the Ni adatom spacing in a chain is large (five Ni adatoms for every four binding sites), dissociation preferentially occurs in the middle of Ni chains of length greater than 4. This is in contrast with the Au chains where the mismatch is minimal and the dissociations preferentially occur at the ends of the chains. In the present case, we find that the mismatch results in  $\sim$ 7 C adatoms for every 6 binding sites. This leads to a collapse of the arch where this dislocation is likely to occur. In [180], dissociation of the long Ni chains at finite temperature occurred at the dislocation site, followed by the formation of 2D compact islands. By analogy, although the 13C double arched structure is energetically favored over the 13C three-ring island, at the high growth temperatures of graphene the arches are expected to dissociate into shorter chains or transform to 2D compact islands. Here again, we stress a distinctive feature of the carbon nanoarches from the previously reported metal chains, namely, the carbon nanoarches have only two ends standing on the substrate, whereas for the metal chains the whole structure lies on the substrate.

### **3.2.4 Transformation from linear nanoarches to compact carbon islands**

Though the nanoarch structure is energetically favored over the entire size range of our study, an actual growth situation at finite temperatures would likely support the coexistence of both 1D chains and 2D islands. In order to get a sense of the metastability of a 2D island on the surface, we use the climbing image nudged elastic band (CINEB) method [136] to determine the activation energy needed to break a hexagonal ring, expected to be the smallest metastable 2D island according to

Fig. 3.5(a). We found a barrier of 0.66 eV (Fig. 3.6), which would be easily overcome at typical growth temperatures. Since any rings that happen to form would easily be broken, we predict that linear chains will dominate on the surface when cluster sizes are less than about ten adatoms. Once there are 10C compact clusters with two closed rings, two bonds would have to be broken in order to form a chain, which is much less likely. Though the energetics shows that a nanoarch is favored through a 13C cluster, entropically there are many more ways to form a 13C island from smaller linear chains than a 13C nanoarch. In a real growth situation 13C compact islands will form and once formed will likely stay intact, because three bonds would have to be broken to disassemble it. This observation, combined with the evidence for dissociation of 10C and 13C chains, points to a relatively short lifetime of these chains and the likely dominance of 2D islands around a typical cluster size of  $\sim$ 10-13 atoms.

### 3.2.5 Discussion and conclusion

Despite the dominance of 1D linear chains observed in various metal-on-metal systems [180–183], the underlying formation mechanisms involved are very different from that in the present case. In conventional metal-on-metal systems, the formation of linear chains is mainly due to the anisotropy of lattice mismatch between the substrate and the deposited metal atoms. The metal adatoms prefer to have as many neighbors as possible and therefore the chains always grow along the directions where the mismatch is minimal. In the present carbon-on-metal systems, the formation of 1D carbon chains is the result of the competition between C-C bonding and C-metal bonding [54]. The stronger C-C bonding also dictates the arched shape of the chains, because the carbon atoms in the middle can only weakly interact with the metal substrate after forming strong C-C bonds with two carbon neighbors. In this sense, the 1D carbon nanoarches are very similar to the 2D nanodomes [50], and are expected to be a common feature in the growth process of graphene on metal substrates [47, 184, 185].

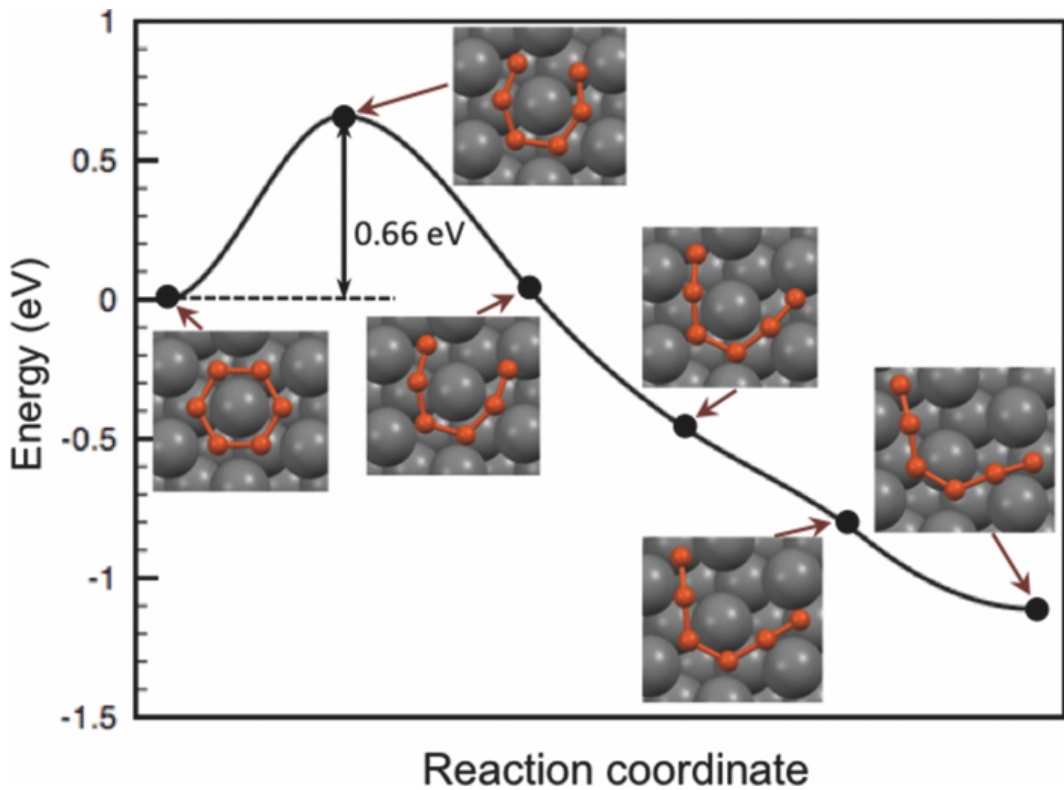


**Figure 3.6:** Energy profile and atomic structures (top view) of a 6C hexagonal ring breaking into a 1D chain. Small orange and large gray balls represent C and Cu atoms, respectively.

In summary, we have carried out a systematic first-principles study of carbon nucleation during the early stages of graphene growth on Cu(111). Our calculations have revealed an energetic preference for the formation of novel, stable 1D carbon nanoarches consisting of 3-13 atoms when compared to 2D compact islands of equal sizes. We have also predicted the critical sizes for 1D to 2D transitions under realistic experimental growth conditions and we expect our findings will stimulate future experimental investigations.

### **3.3 Suppression of Grain Boundaries in Graphene Growth on Superstructured Mn-Cu(111) Surface**

#### **3.3.1 Introduction**

As mentioned in the previous section, one standing obstacle facing the community of epitaxial graphene on Cu is the prevalence of grain boundaries (GBs) undesirably introduced during growth [59–66]. A grain boundary refers to the junction region of two crystalline grains with different orientations. The detailed atomic structures of the GBs in epitaxial graphene have been investigated extensively [59, 61–66], and their presence has been shown to severely degrade the electronic, transport, and mechanical properties of graphene [59, 64]. Experimental efforts have also been made to suppress their creation during growth [59, 186, 187], but so far with limited success, partly because the underlying formation mechanism of the GBs is still unclear. Existing experimental observations suggest that the GBs can form in the initial nucleation stage when several graphene grains emanate from one nucleation site [64]; alternatively, they can be formed in the later growth stage when different graphene grains with relative misorientations coalesce [56, 59, 66].

In this section, we first demonstrate that, because of the inherently weak C-Cu interaction, orientational disorders of carbon islands on Cu(111) will be abundant in the early stages of nucleation and growth. Such disorders cannot heal themselves with the enlargement of the islands, leading to the prevalence of graphene GBs upon island coalescence. Based on this understanding, we propose to use a functionalized Cu(111) surface to lift the energy degeneracy in the early stages of nucleation and growth, thereby suppressing orientational disorders of the islands and the subsequent GBs. Our proposed kinetic pathway invokes the steps of “seed and grow” [188]. In the seeding step, carbon clusters are initiated by depositing coronene on a  $(\sqrt{3} \times \sqrt{3})$  R30° Mn-Cu(111) alloyed surface [189, 190], which effectively helps the islands to select predominantly only one orientation on the superstructurally alloyed surface. In the growing step, larger, monolayer graphene is formed by conventional chemical vapor deposition (CVD).

### 3.3.2 Methods

Our density functional theory (DFT) calculations are carried out using the Vienna *ab initio* simulation package (VASP) [125] with PAW potentials [126, 127] and the generalized gradient approximation (PBE-GGA) [128] for the exchange-correlation functional. The lattice constant of Cu is obtained via structural optimization. The generic Cu(111) surface is modeled by a slab of 5 atomic layers, and the Mn-Cu(111) surface is realized by substituting Cu atoms by Mn atoms at ordered positions in the first layer. The vacuum layers are more than 13 Å thick to ensure decoupling between neighboring slabs. During relaxation, atoms in the lower 2 atomic layers are fixed in their respective bulk positions, and all the other atoms are allowed to relax until the forces on them are smaller than 0.01 eV/Å. A  $2 \times 2 \times 1$   $k$ -point mesh is used for the  $6 \times 6$  surface unit cell and  $3 \times 3 \times 1$  for the  $4 \times 4$  surface unit cell [167]. The calculations with Mn atoms are spin-polarized. We consider the ferromagnetic configuration of

the Mn-Cu(111) surface, because of the triangular arrangement of the Mn atoms. The binding energies are calculated as  $\Delta E = E_{\text{adsorbate}} + E_{\text{substrate}} - E_{\text{adsorbate+substrate}}$ .

### 3.3.3 Formation of graphene GBs on Cu(111) surface

Crystalline Cu has a face-centered cubic (fcc) structure, and its (111) surface exhibits a hexagonal packing of surface atoms. As shown in Figs. 3.7 (a) and (b), both the Cu(111) surface and graphene have atomic arrangements with six-fold symmetry. Therefore, if carbon clusters nucleated at different sites are all oriented at the *same* high-symmetry orientation (HSO) of the Cu(111) surface (e.g., Fig. 3.7 (c) *or* (d)), their structural coherence will be ensured by the Cu substrate and there will be no GBs when they merge. However, when a simple six-fold symmetric carbon cluster composed of seven 6-carbon rings (7CR) is placed on the Cu(111) surface, our detailed DFT calculations reveal that the energetically most stable geometry deviates from the HSO of Fig. 3.7 (c) by  $11^\circ$  (Fig. 3.8 (b)). The carbon cluster also has a dome-like structure (Fig. 3.8 (a)), with the central C atoms  $\sim 2.30\text{\AA}$  from the Cu surface. Therefore, the cluster remains strongly bonded to the substrate only at the periphery while the interaction between the central C atoms and the substrate is rather weak, similar to the domed structure on Ir(111) [50]. Each of the 12 edge C atoms has two C neighbors, and prefers to reside at the bridge sites between two surface Cu atoms, because these edge atoms are closer to  $sp^3$  hybridization than  $sp^2$ , thereby providing the driving force for the rotation of the island away from the HSO.

Now we go from the early stages of island nucleation and growth to island enlargement and coalescence. Since a small cluster such as the one shown in Fig. 3.8 is not oriented at the HSO, there will be a degenerate mirror geometry with respect to the symmetry axis of Cu(111), indicating that islands with relative misorientations can coexist. As a cluster grows larger, more edge C atoms will be involved in determining its preferred orientation by adjusting their bonds with the underlying Cu atoms. Therefore, there will be more nearly degenerate orientations, thus broadening

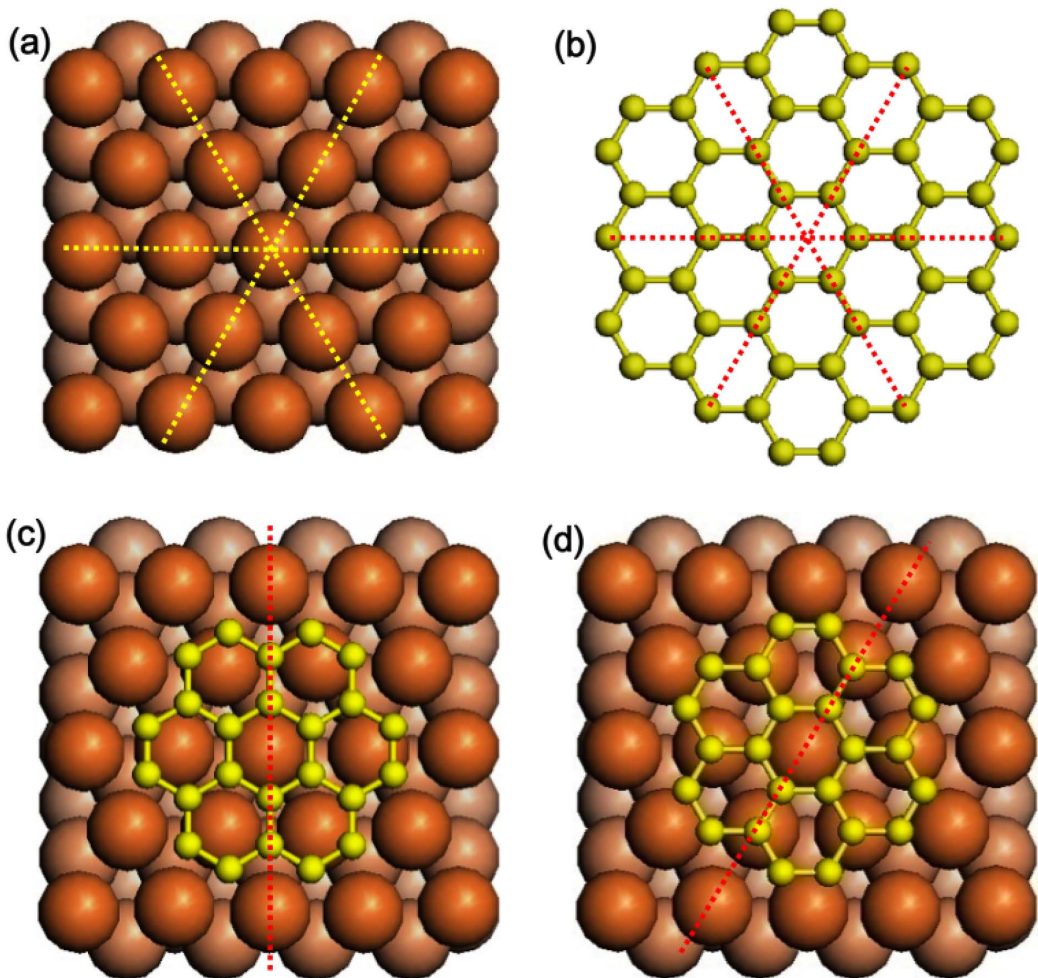


**Figure 3.7:** (a) and (b) Structural illustrations of the Cu (111) substrate and graphene, where the yellow and red dashed lines show their respective high-symmetry axes. (c) and (d) Illustrations of two geometries where a 7CR carbon cluster is at a HSO on the Cu(111) surface. In (c), the edge C atoms reside at the 3-fold hollow sites; in (d), the edge C atoms are at the bridge sites between two surface Cu atoms.

the orientational disorder of the carbon clusters. When a cluster has grown large enough such that the edge atoms contribute only minimally to the total binding energy, the cluster is either still in an energetically stable orientation different from the HSO, or is too large to adjust its orientation to an energetically more favorable HSO. When two such clusters with a relative misorientation coalesce, a larger island containing a GB is formed, with a characteristic angle defined by the initial misorientations of the merging clusters and the local structural adjustment within the boundary. This scenario is qualitatively consistent with existing experimental observations, and the detailed distribution of the GB angles may also depend on the specific growth conditions [64–66].

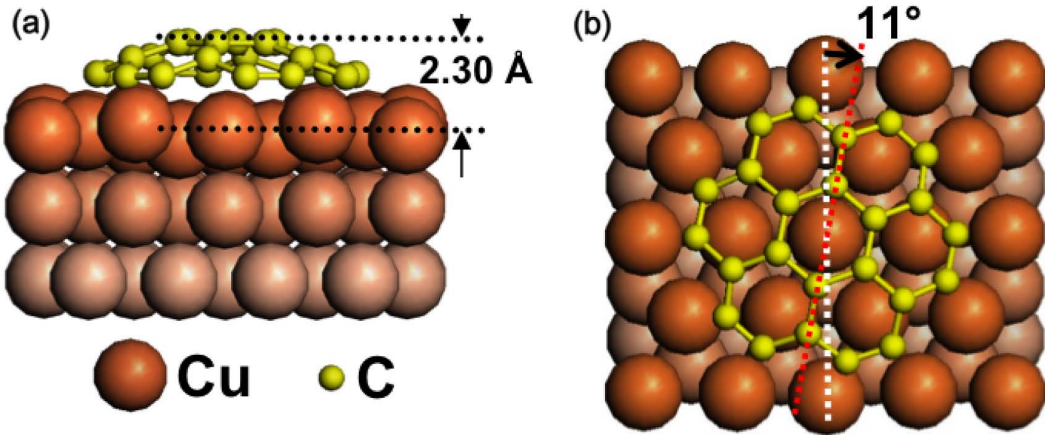


**Figure 3.8:** Side and top view of a 7CR on the Cu(111) surface, illustrating the domed nature (a) and the rotated nature (b) from the HSO of Fig. 3.7 (c), respectively.

### 3.3.4 Suppression of graphene GBs using a superstructurally alloyed substrate and a two-step kinetic pathway

Next we search for ways to lift the energy degeneracy in island nucleation and growth via Cu(111) surface modification. Fig. 3.9 (a) illustrates a  $(\sqrt{3} \times \sqrt{3})$  R30° X-Cu(111) superstructurally alloyed surface, which has transition metal atoms X substituting Cu at ordered positions. The choice of X is guided by the requirements that, (a) C binds

more strongly to X than to Cu, so that the nucleated carbon clusters will prefer a HSO in maximizing their interaction with the X atoms; and (b) the alloyed X-X atoms are repulsive. We find that a number of transition metals (X= Ru, Fe, Co, Ni, Mn) have unfilled *d* orbitals and bind more strongly with C, but only Mn atoms are mutually repulsive when alloyed into the top layer of Cu(111), indicating that Mn could form a superstructured surface alloy with Cu. Indeed, experimentally the formation of a  $(\sqrt{3} \times \sqrt{3})$  R30° superstructured Mn-Cu(111) surface has been observed [189], whereas the other metals only form islands or overlayers on Cu surfaces [191].

Still choosing 7CR as the testing baby graphene, we then calculate the total energies of 7CR with different orientations on the  $(\sqrt{3} \times \sqrt{3})$  R30° Mn-Cu(111) alloyed surface. We find three stable or metastable configurations of a 7CR island through structural optimization, differentiated by placing the center of the 7CR above a Mn or Cu atom, as shown in Fig. 3.9. Two of them (Figs. 3.9 (b) and (c)) are at HSO, but only the HSO in Fig. 3.9 (b) is the most stable, while the energy of the other two configurations is higher by 0.32 eV and 0.45 eV, respectively. Therefore, the Mn atoms alloyed into the Cu(111) surface indeed successfully help to pin the 7CR at the HSO. To see the underlying atomistic reason, we note that in all the three cases, the island has a dome-like geometry similar to that on a pure Cu(111) surface, indicating the predominant interaction with the substrate at its edge. Moreover, in the most stable configuration, the 7CR maximizes its contact with the Mn atoms at the periphery. The calculated binding energy per edge C atom of 7CR is 0.63 eV on Cu(111) and 0.89 eV on Mn-Cu(111).

To take advantage of the superstructural Mn-Cu(111) surface and effectively suppress the possible disorders induced in the initial nucleation process, we propose the use of coronene as a good candidate to seed the initial carbon clusters. As a polycyclic aromatic hydrocarbon, coronene is just like the 7CR island, but with a hydrogen atom on each edge C atom. We have compared the dehydrogenation process of coronene to that of benzene, which has been used for low temperature graphene growth on Cu [192]. In free space, the C-H bond dissociation energies of benzene and

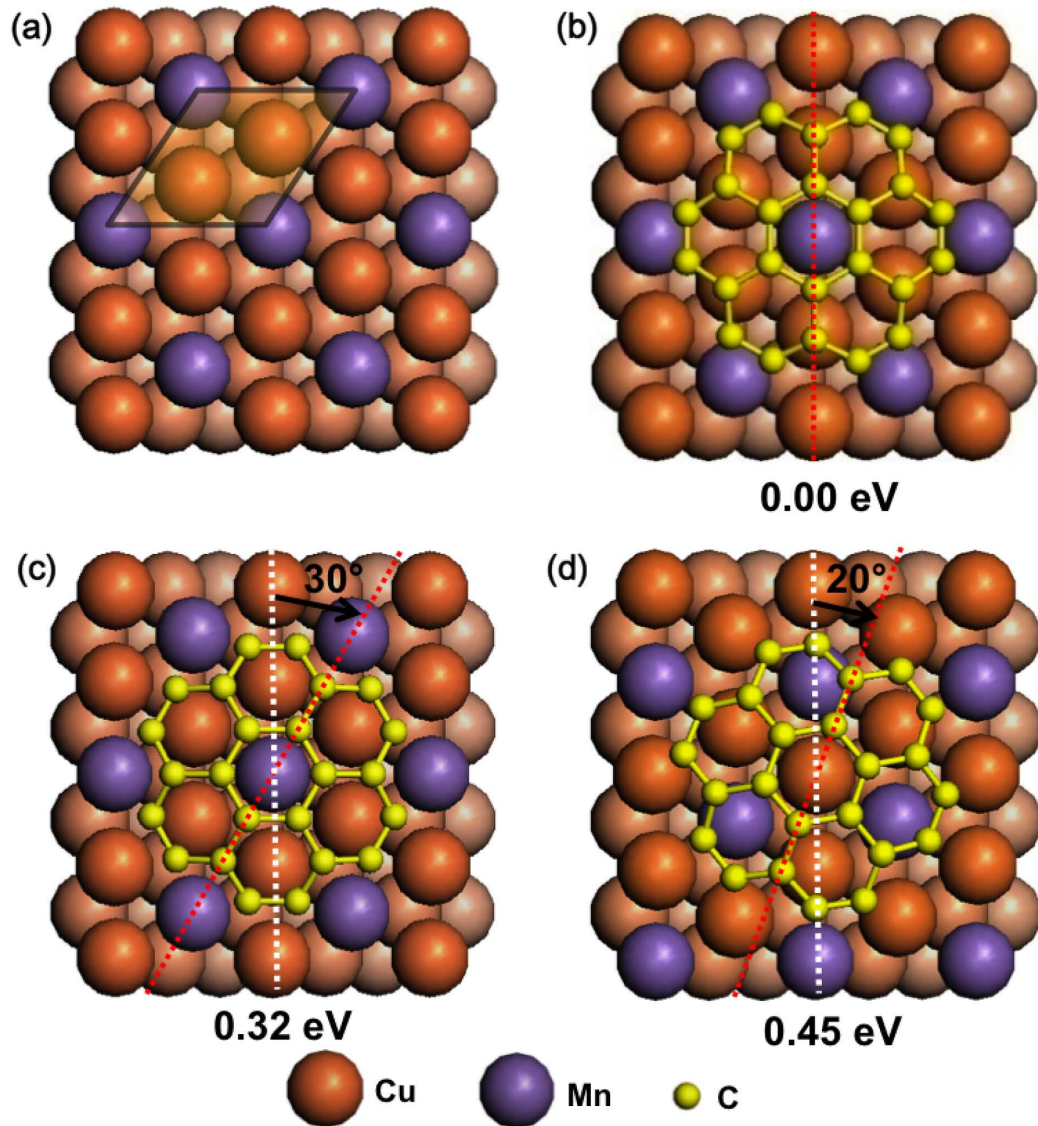


**Figure 3.9:** (a) Structure of the  $(\sqrt{3} \times \sqrt{3})$  R30° Mn-Cu(111) superstructurally alloyed surface. (b-d) Three stable geometries of a 7CR adsorbed on the Mn-Cu(111) surface. As indicated by the red dashed lines, (b) and (c) illustrate two HSO configurations, while (d) is rotated from a HSO, and their relative stabilities are indicated by their total energy differences.

coronene are very close [193], as verified also by our DFT calculations. Considering the effect of the catalytic substrates, the energy difference between the initial state, where a coronene is adsorbed onto the Mn-Cu alloyed surface, and the final state, where all the edge hydrogen atoms are dissociated in the form of H<sub>2</sub>, is 1.23 eV per H atom, which is 0.16 eV lower than that of benzene on Cu(111). Therefore, the alloyed surface will be more catalytic in dehydrogenating adsorbed coronene than Cu(111) in dehydrogenating benzene [192]. We therefore propose to use coronene as the first-step carbon source to seed carbon clusters on the patterned surface.

After the deposition and dehydrogenation of coronene on Mn-Cu(111) surface, all the adsorbed 7CR islands will have the same orientation. In particular, when two such 7CR islands coalesce to form a larger graphene cluster, no GB is formed (Fig. 3.10). In order to achieve a continuous sheet of graphene, we invoke a second step of growth to supply C atoms to fill the openings between the carbon clusters. We notice that, in contrast to Cu(111), on which C adatoms are energetically much more favorable to nucleate than to stay apart [54], here on Mn-Cu(111) the carbon adatoms are less strongly inclined to nucleate. The energy difference between a C dimer and two C monomers on the substrate, calculated as  $\Delta E = E_{\text{monomer+substrate}} \times 2 - E_{\text{substrate}} - E_{\text{dimer+substrate}}$  is 2.92 eV on Cu(111) and becomes 1.70 eV on Mn-Cu(111). Therefore, the conventional CVD growth using methane or ethylene could be applied here to supply carbon adatoms to diffuse and attach to the nearby coronene-seeded and correctly-oriented carbon islands (Fig. 3.10), rather than to nucleate new islands, which is similar to the enhanced layer-by-layer growth of Ag on Ag(111) via a two-step kinetic pathway [188]. Eventually, the 7CR-seeded islands will be enlarged and connected to achieve a single-crystal graphene sheet with no or greatly suppressed GBs.

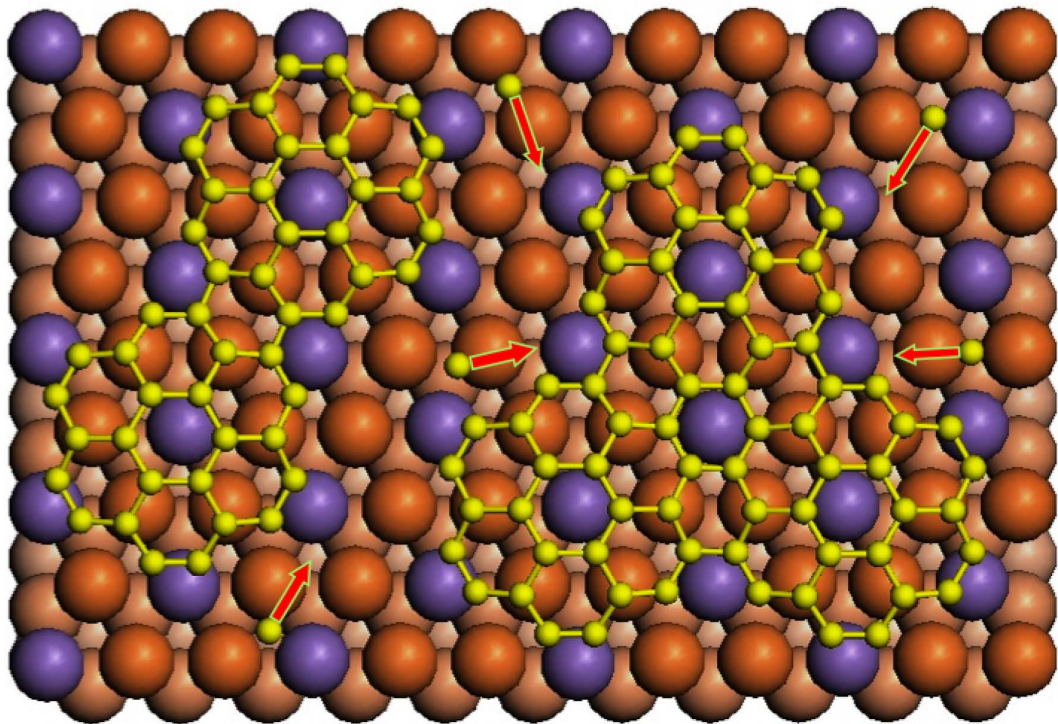


**Figure 3.10:** Enlargement of coronene-seeded carbon islands via conventional CVD growth. The individual C adatoms supplied in the second step of the “seed and grow” kinetic pathway diffuse and attach to the nearby islands to fill the opening spaces, resulting in a larger graphene sheet with no GBs.

### **3.3.5 Discussion and conclusion**

It is important to note that, when a 7CR seed grows larger, the carbon clusters will still be at or close to the HSO, because an edge C atom prefers to reside at the bridge site between a Mn and a Cu atom. Because all the islands have nearly the same orientation and dome-like geometry, they will be able to make minimal local adjustments when they meet, and coalesce to form a single larger graphene sheet without GBs. Because of the lattice mismatch and its stronger interaction with the Mn-Cu(111) surface than with pure Cu(111), graphene may have a corrugated geometry, similar to that on Ru [194]. Finally, the playground of using patterned substrates is not necessarily limited to the Mn-Cu(111) surface; other superstructured surface alloys with different transition metals beyond the ones already considered here are also worth exploring. The present study of graphene growth on patterned substrates via a two-step kinetic process thus opens the door towards a new and viable approach for mass production of single crystalline monolayer graphene.

## **3.4 Formation of Graphene *p-n* Superlattices on Pb Quantum Wedged Islands**

### **3.4.1 Introduction**

As conventional silicon-based semiconductor technology approaches its fabrication and operation limits, the demand for new materials and devices becomes increasingly pressing [195]. Graphene, owing to its simplicity and remarkable electronic transport properties, has recently emerged as a promising candidate material for future post-silicon electronics [196]. Its unusual linear energy dispersion gives rise to giant charge carrier mobility and a Dirac-like transport behavior, thereby enabling both fundamental studies of relativistic quantum phenomena and new device applications [162, 163, 197]. Notable exotic relativistic quantum phenomena, such as Klein

tunneling [198, 199], Veselago lensing [200], and guided plasmons [201], have been theoretically predicted in graphene *p-n* junctions. More recently, it has also been predicted that a graphene *p-n* superlattice structure can lead to a number of fascinating new phenomena, including electron beam supercollimation [86], anisotropic transmission [87], creation of additional Dirac cones [88, 89], and effective magnetic fields [90]. However, the creation of well-ordered and atomically sharp *p-n* junctions or superlattices remains practically challenging—though some prototype graphene *p-n* junctions have been experimentally demonstrated via local gating with costly and time-consuming e-beam lithographic techniques [202–204], spatially selective chemical doping [205], or electrostatic modification of the gate insulator surface [206]. Recent theoretical studies on the interaction between graphene and a series of metals indicate that metal-induced changes to the electrostatic potential in the graphene layer can result in net *n*- or *p*-type doping, depending on the work function of the metal surface [207, 208]. Experimentally, epitaxial growth of high quality graphene has been successfully demonstrated on a variety of metal substrates, which may serve as a rational synthesis route for producing macroscopic single-crystalline graphene [40, 42, 43, 45, 46, 48, 51, 209].

In this section, we report on a novel scheme to create graphene *p-n* superlattices on Pb wedged islands by taking advantage of the spatial oscillations in the surface work function. The Pb wedged islands, schematically illustrated in Fig. 3.11 (a), can be grown on Si(111) vicinal substrates at room temperature [92]. These islands have an atomically flat top oriented in the [111] direction driven by surface energy minimization [210, 211], but their bottom extends laterally over several atomic steps on the Si vicinal substrate. Thus each Pb wedged island contains striped regions consecutively increasing in thickness, and, more importantly, the width of the stripes is solely determined by the experimentally tunable terrace width of the underlying Si vicinal substrate. Such wedged islands provide an ideal platform for studying the influence of quantum size effects on the physical and chemical properties of the materials adsorbed on top of the quantum wedge [212–215]. Previous first-principles

calculations and scanning tunneling spectroscopy (STS) measurements have shown that Pb(111) films exhibit a bi-layer work function oscillation (see Fig. 3.11 (b)), which arises from the unique matching between the bulk Pb Fermi wavelength and the Pb(111) interlayer lattice spacing [93–96]. Here, we use first-principles calculations within density functional theory (DFT) to demonstrate that when a single layer of graphene is placed on the surface of such a Pb wedged island, the spatial oscillations in the surface work function will induce a corresponding oscillation in the position of the graphene Dirac point relative to the Fermi level of the system. Furthermore, by applying an external electric field of 0.5 V/Å perpendicular to the surface the graphene Fermi level can be globally tuned to an appropriate position, such that the whole graphene layer becomes a well-defined graphene *p*-*n* superlattice with seamless junctions.

### 3.4.2 Methods

Our first-principles DFT calculations were carried out using the VASP code [125], with the projector augmented wave (PAW) method applied to describe the electron-ion interactions [126, 127]. The local density approximation (LDA) [216] was used to approximate electron exchange and correlation—as it provides a much better description of the graphene-metal binding energy and equilibrium separation than the generalized gradient approximation (GGA) [208]. The plane-wave kinetic-energy cutoff was set at 400 eV. The lattice constants of bulk Pb and graphene determined with these computational approximations are 4.879 Å and 2.446 Å, respectively, which are in good agreement with the experimental values of 4.95 Å and 2.46 Å. The Pb films were modeled by periodic slabs consisting of 4-8 monolayers (MLs), separated by a vacuum region of 18 Å. To match graphene on the Pb films, we constructed a  $2 \times 2$  Pb(111) surface cell and placed a  $3 \times 3$  graphene layer on top, resulting in a mismatch of around 6%. We set the in-plane lattice constant of Pb(111) at its optimized LDA value and adapted the lattice of graphene accordingly. In optimizing

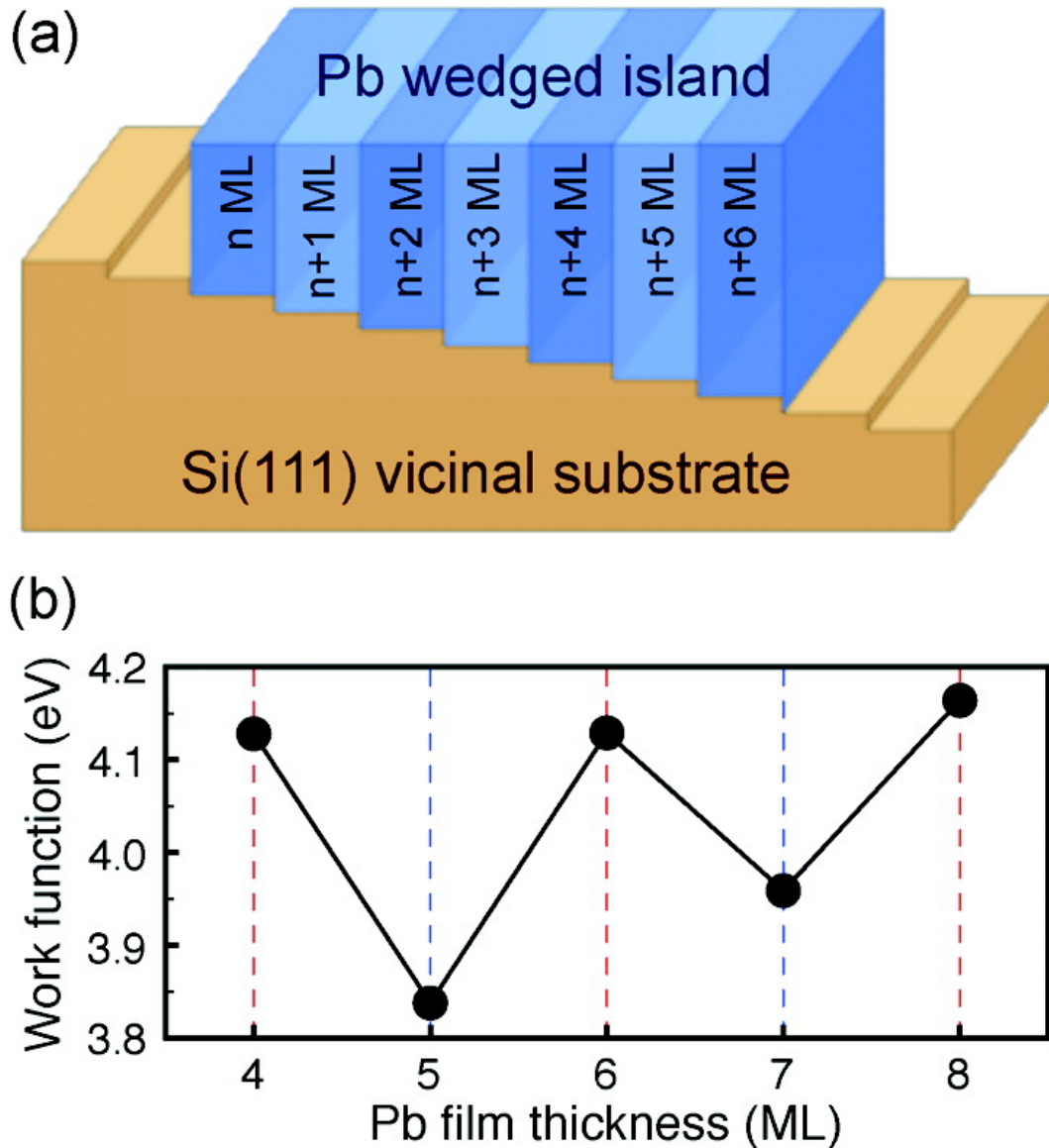


**Figure 3.11:** (a) Schematic illustration of a Pb wedged island grown on a Si(111) vicinal substrate. (b) The work function of Pb(111) films calculated within DFT as a function of the film thickness.

the geometry, the bottom monolayer Pb atoms were fixed at their bulk positions and all other atoms were allowed to relax until the forces on all the unconstrained atoms were smaller in magnitude than 0.01 eV/Å. To include the effect of an external electric field, an artificial dipole layer was placed in the middle of the vacuum region far away from either side of the slab [217, 218].

### 3.4.3 Oscillatory electron doping of graphene on Pb wedged islands

We begin this study by searching for the stable adsorption geometries of graphene on Pb(111) films. To this end, a number of possible configurations have been considered in our study. Figs. 3.12 (a) and (b) show the two most stable structures, which are nearly degenerate in energy. Their relative stability depends on the Pb film thickness, but their total energy difference is less than 0.02 eV for all the cases studied. Even with the most stable structures, graphene is weakly adsorbed (physisorbed) on the Pb(111) films; the calculated binding energies are around 0.026 eV per carbon atom and the average equilibrium separation between graphene and the Pb(111) surface is around 3.6 Å for all film thicknesses [207, 208].

To identify changes in the electronic structure of graphene occurring upon Pb(111) adsorption, we have calculated the band structure of graphene atop a 4-ML Pb(111) film at both of the stable adsorption geometries [as illustrated in Figs. 3.12 (a) and (b)]. The energy bands arising from graphene can be identified in the combined system by comparing the band structure of free-standing graphene [see Fig. 3.12 (c)] with that of an isolated 4-ML Pb(111) film [see Fig. 3.12 (d)]. Since a  $3 \times 3$  graphene unit cell is used in the calculations, the  $1 \times 1$  unit cell  $K$  points in reciprocal space are folded onto the  $\Gamma$  point. The absorbed graphene band splitting at the  $\Gamma$  point results from the periodic substrate induced corrugation, which introduces electronic coupling between the two distinct Dirac cone valleys of flat graphene. Nevertheless the Dirac cone of graphene is largely preserved, since flat strained graphene adsorbed

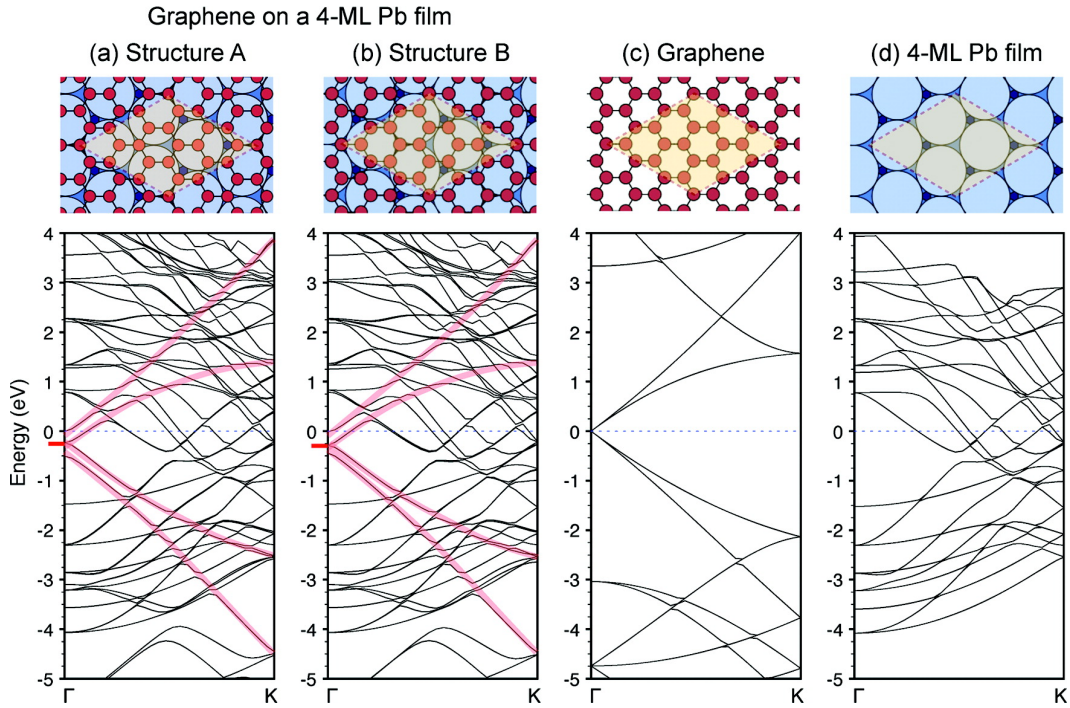


**Figure 3.12:** Atomic structures and calculated band structures of the two most stable configurations of graphene on 4-ML Pb(111) films [(a) and (b)], a single layer of graphene (c), and a 4-ML Pb(111) film (d). Red and blue balls represent C and Pb atoms, respectively. The Fermi levels are set to zero in the band structure plots, as denoted by blue dashed lines. In the graphene/Pb combined systems (a) and (b), the graphene band structure is highlighted via transparent red curves, and red short bars attached to the energy axis indicate the positions of the graphene Dirac point.

on Pb(111) films and the two relaxed minimum structures give nearly identical shifts in the graphene Dirac point with respect to the Fermi level of the system. Similar calculations have also been carried out for 5-8 ML Pb(111) films. Figs. 3.13 (a-e) show the band structure of graphene atop 4-8 ML Pb films, respectively. Since the two stable adsorption geometries have nearly identical band structures, only the plots for the structure A [see Fig. 3.12 (a)] are presented in Fig. 3.13 for comparison. In Fig. 3.12 (f), the position of the graphene Dirac point is plotted as a function of the Pb(111) substrate film thickness, a clear bi-layer oscillation in the Dirac point is evident (due to the work function oscillation in the underlying Pb films). A linear relationship between the position of the graphene Dirac point and the work function of the Pb films is revealed in Fig. 3.12 (g). However, the graphene Dirac point lies below the Fermi level at all film thicknesses, meaning the graphene is *n*-type doped by the Pb substrate. This can be attributed to the relatively small work function of Pb(111) ( $\sim 4$  eV). Previous calculations indicate that the crossover from *n*-type to *p*-type doping occurs for a metal work function of  $\sim 5.4$  eV [207, 208].

### 3.4.4 Realization of graphene *p-n* superlattice with the help of electric gating

To achieve a graphene *p-n* superlattice, the Fermi level of graphene needs to be shifted downward. One possible way to achieve this is through an external electric field applied perpendicular to the surface, as schematically illustrated in Fig. 3.14 (a), such that some screening electrons on graphene are forced back into the Pb substrate and consequently shift the graphene Fermi level downward. To quantitatively determine the critical magnitude of the electric field required to form a graphene *p-n* superlattice on a Pb wedged island, we have included an electric field in the surface normal direction ranging from 0.1 V/ $\text{\AA}$  to 0.8 V/ $\text{\AA}$  in our first-principles calculations. The results for film thicknesses from 4 to 8 MLs, presented in Fig. 3.14 (b), indicate that the Dirac point position is elevated approximately linearly with respect to the external

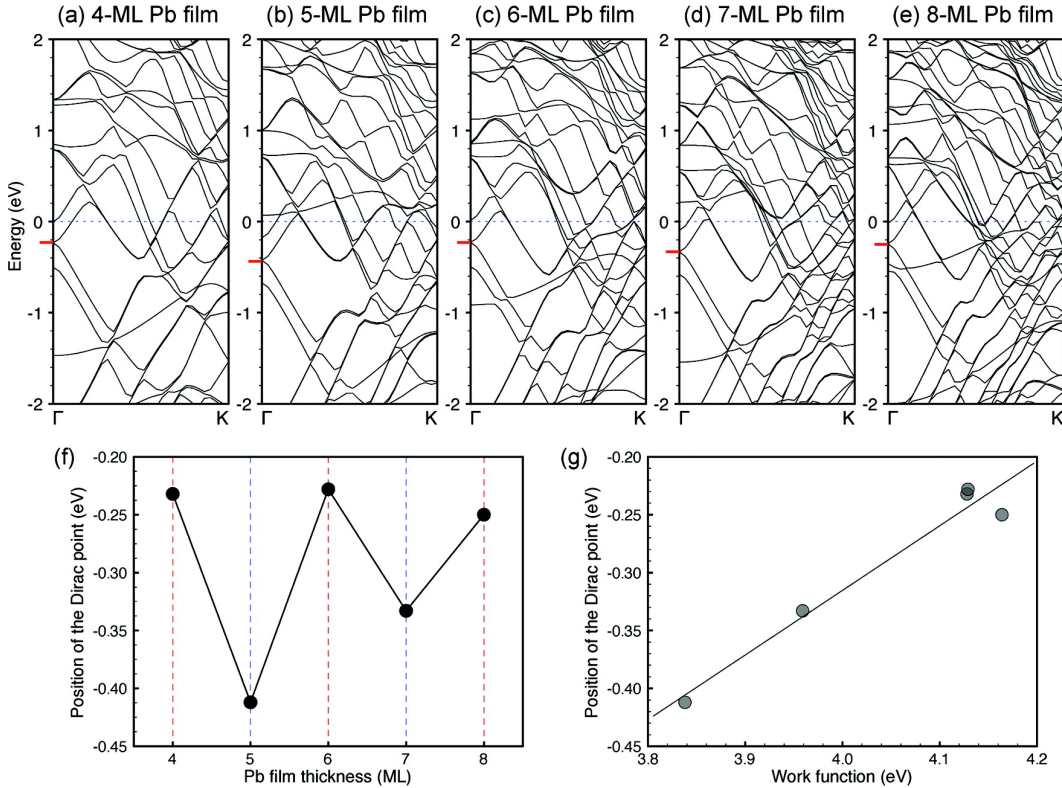


**Figure 3.13:** Band structure of graphene on 4- to 8-ML Pb(111) films [(a)-(e)]. The Fermi levels are set to zero in the band structure plots, as denoted by blue dashed lines. (f) The positions of the graphene Dirac point with respect to the Fermi level as a function of the thickness of the underlying 4- to 8-ML Pb films. (g) The correlation between the position of the Dirac point and the work function of the Pb films.

electric field magnitude. To better illustrate the evolution of the Dirac point shifts and identify the critical magnitude of the electric field required to achieve a graphene *p-n* superlattice, the same set of data is plotted as a function of the Pb film thickness at different electric fields [see Fig. 3.14 (c)]. From this plot, it is evident that the graphene Dirac points (for all film thickness) are simultaneously pushed upwards by the applied field and that a critical electric field of around  $0.5 \text{ V}/\text{\AA}$  is required to form a graphene *p-n* superlattice on a Pb wedged island—which is comparable to the field strength applied to open a bandgap in bilayer graphene as recently demonstrated experimentally [113].

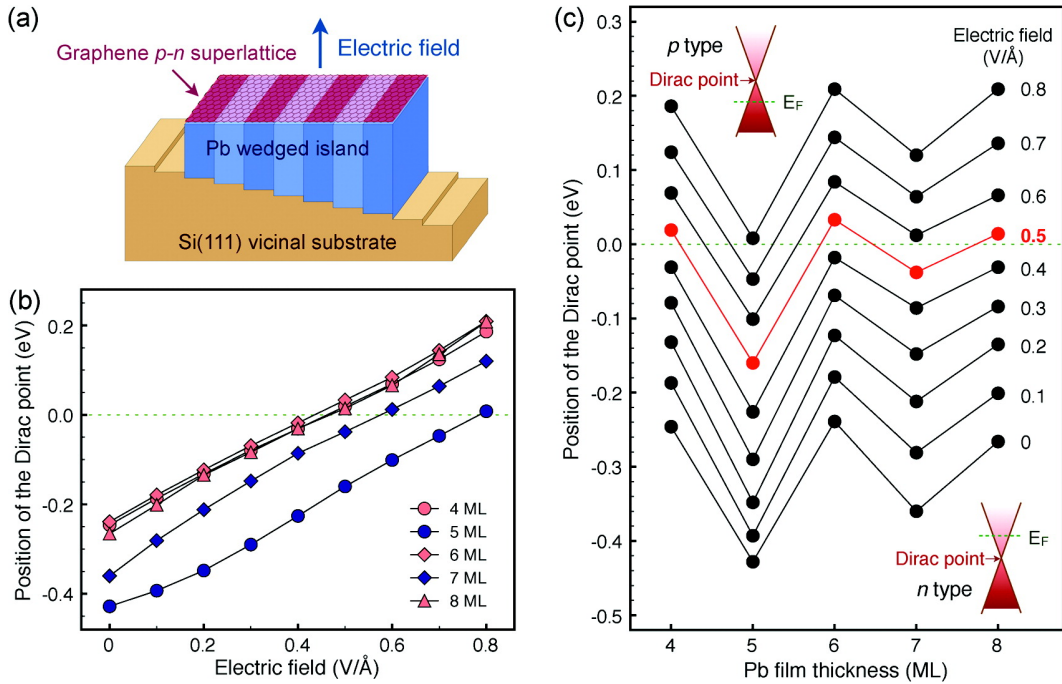


**Figure 3.14:** (a) Schematic illustration of a graphene *p-n* superlattice formed on a Pb wedged island with an external electric field applied in the surface normal direction. (b) and (c) Evolution of the graphene Dirac point position plotted as a function of the electric field (b) and the Pb film thickness (c). The Fermi level is set to zero in all plots and denoted by green dashed lines.

The correlation between the graphene Fermi level position and the external electric field magnitude can be understood using a phenomenological parallel plate capacitor model, such as that given in Refs. [207, 208]. There, the work function difference

between graphene and the substrate is balanced by (1) the classical capacitance of the capacitor (i.e. the potential difference developed due to charge redistribution between two plates) plus the charging energy of each plate, and (2) the quantum capacitance of graphene (i.e. the Fermi level shift relative to the Dirac point). In Refs. [207, 208], the authors take the charge redistribution in (1) equal to the amount calculated by integrating the graphene density of states in the range swept by the Fermi level. However, in the following we point out that this parallel plate picture is not entirely accurate when graphene and the substrate are in direct contact, such that the overlap between the “spilled-out” charge is non-negligible.

To clearly visualize the charge redistribution upon application of an external electric field, we plot the plane-integrated electron density screening charge of graphene on a 7-ML Pb film in Fig. 3.15 (a) at various electric field intensities. As expected, the applied electric field pushes electrons from graphene to Pb, and this screening charge transfer increases with the applied electric field magnitude. We then integrate screening charge in Fig. 3.15 (a) from the zero point halfway between graphene and Pb to the vacuum above graphene where the screening charge density vanishes. This amount of charge  $\Delta Q_R$  ( $R$  for real space) is physically “on” the plate of graphene and is analogous to the charge redistribution between two parallel plates in a classical capacitor. For comparison we also calculated  $\Delta Q_E$  ( $E$  for energy space) by integrating the graphene density of states in the range swept by the Fermi level (upon applying an external field). The results are depicted in Fig. 3.15 (b) and one can see that  $\Delta Q_E$  significantly underestimates the charge redistribution in the real space. This is because  $\Delta Q_E$  does not take into account the tail of the spilled-out charge from Pb, which extends over the gap region between graphene and Pb and contributes to screening the external field inside the gap. To better support our statement, we separately calculated the screening charge redistribution of both graphene and the 7-ML Pb film in isolation (with their respective geometries fixed). We then properly combine the two isolated screening charge densities and perform integration in the same spatial range as we did for  $\Delta Q_R$ . Within the graphene-Pb gap

this charge counting scheme is analogous to a phenomenological WKB model. The resulting  $\Delta Q_S$  quantity (S for spilled-out charge correction) is also shown in Fig. 3.15 b) and agrees well with  $\Delta Q_R$ .

### 3.4.5 Discussion and conclusion

It should be noted that instead of modeling a Pb wedged island we used flat Pb films of different thicknesses and performed the calculations separately. On a real Pb wedged island, it is expected that some charges will accumulate at the interfaces between the Pb stripe regions with different work functions. Such interface charge accumulation will create a local electric field at the interface and thereby balance the Fermi level difference between two adjacent regions. However, at a particular small region the shift of the graphene Dirac point relative to the local Fermi level is solely determined by the local work function of the Pb surface and the uniform external electric field. Therefore, given the short screening length of Pb as a metal [ $\sim 0.75$  nm as shown in Fig. 3.15 (a)], as evident from the experimental STS work function measurements [95, 96], the interface charge accumulation is not expected to invalidate our proposed scheme of creating graphene *p-n* superlattices on Pb wedged islands, as long as the width of each Pb stripe region is much larger than the screening length of Pb [95, 96].

The proposed graphene *p-n* superlattice mechanism in this work relies on the spatial oscillation of the surface work function of *metallic* Pb wedged islands. Hence with respect to graphene transport measurements, such *metallic* islands can form an electrical short and are therefore only appropriate for ballistic conduction measurements when the islands are not connected to the electron source or drain injecting electrons/holes into graphene. The absence of Pb electronic states at the graphene Dirac point and the weakness of the graphene-Pb physisobtion interaction imply minimal electronic coupling between conducting graphene electrons and Pb (see Figs. 3.12 and 3.13) [219]. Therefore, the probability of electrons injected directly

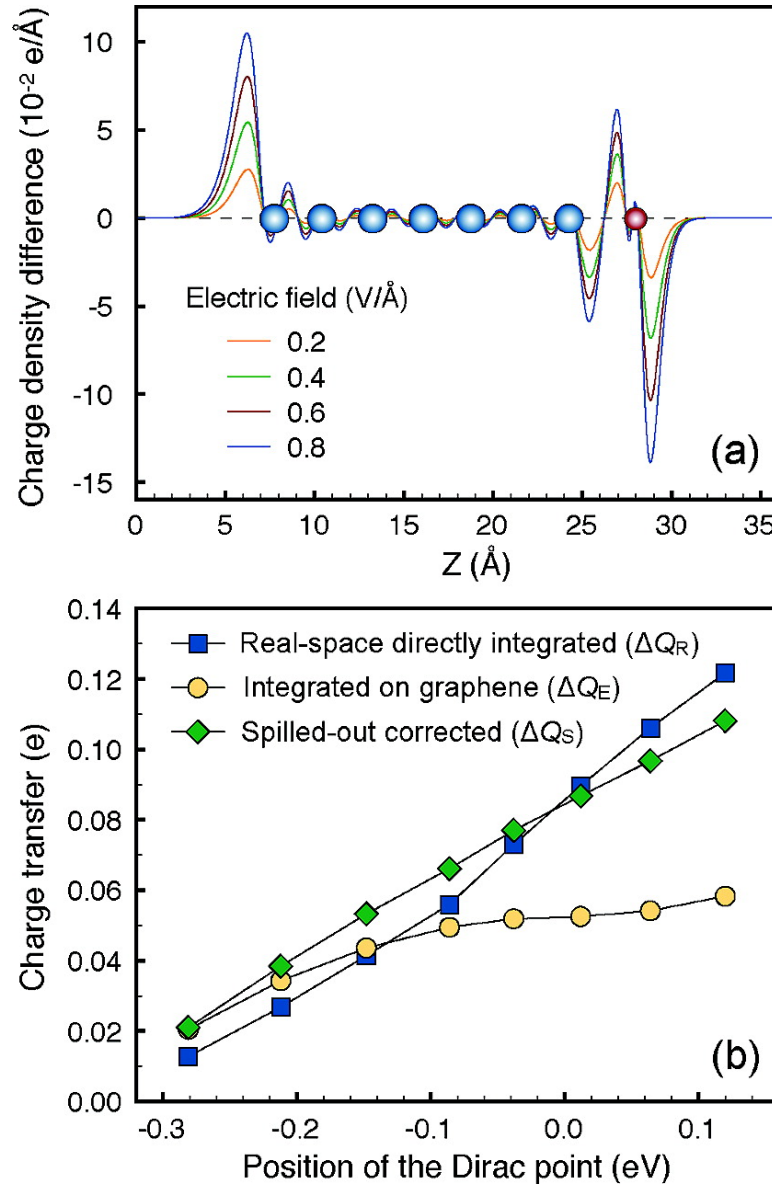


**Figure 3.15:** (a) Electron screening charge for a graphene layer placed on a 7-ML Pb(111) film. The screening charge density is integrated in the plane parallel to the Pb(111) film and plotted in the perpendicular direction. Red and blue balls indicate the positions of C and Pb layers, respectively. (b) Amount of charge transferred out of the graphene versus the position of the Dirac point. Blue squares ( $\Delta Q_R$ ) are the total screening charge density integrated in real space from the zero point halfway between graphene and the Pb film into the vacuum. Yellow dots ( $\Delta Q_E$ ) are the amount of charge transfer estimated from integrating the graphene DOS in the range swept by the Fermi level. Green diamonds ( $\Delta Q_S$ ) are the summed screen charges of isolated graphene and the isolated Pb film (integrated in the same manner as  $\Delta Q_R$ ).

into graphene (and not into Pb) subsequently scattering into an isolated Pb(111) donor/acceptor substrate can be made negligible at sufficiently low temperatures (where inelastic scattering into Pb is minimized) and at distances less than a mean free path [220].

Additionally, we propose that this superlattice structure might possibly be preserved through delicate chemical modifications. Previous experimental studies have demonstrated that the surfaces of Pb(111) wedged islands exhibit spatial oscillatory chemical reactivity [213] and adsorbate binding [215], due to the same quantum size effects highlighted in this work. Similar tunable chemical behavior may also exist on the surface of a graphene *p-n* superlattice when it is placed atop a Pb wedged island. Once such a graphene layer is chemically modified, via selective reactions or adsorbate bindings within the oscillatorily doped regions, the superlattice structure might then be preserved even after it is lifted from the Pb wedged island for further chemical modifications to create other types of graphene-based superlattices, as a new way of achieving graphene band engineering. This strategy is similar to a recent proposal to create hydrogenated graphene superlattices via selective H adsorption on strain-engineered nanoripples [221]. The validity of this speculation requires further extensive studies to confirm.

In summary, we have demonstrated a novel scheme to create atomically sharp graphene *p-n* superlattices on Pb quantum wedged islands induced by an external electric field. To achieve such a graphene *p-n* superlattice, a critical external electric field of  $\sim 0.5$  V/ $\text{\AA}$  has been estimated based on first-principles DFT calculations. The relationship between the graphene Fermi level position and the external electric field magnitude has been quantitatively analyzed using a phenomenological parallel plate capacitor model. This finding may provide an effective approach to virtually divide a single graphene layer into stripe regions with distinctive electronic and chemical properties of well-controlled width, offering a novel route to potentially create graphene-based superlattices with innovative applications such as electron beam supercollimation [86].

## 3.5 Diluted Ferromagnetic Graphene via Compensated *n-p* Codoping

### 3.5.1 Introduction and methods

The high charge carrier mobility due to suppression of backscattering [163], and long spin coherence time because of weak intrinsic spin-orbit coupling, make graphene a promising material for spintronic applications [99]. A crucial issue in realizing graphene-based spintronics is how to introduce magnetic order, or most ideally, long-range ferromagnetism, in graphene. A number of mechanisms that can make graphene magnetic have been proposed in the past few years, including zigzag edges in graphene nanoribbons or quantum dots [100], carbon vacancies [101], hydrogenation [102, 103], and doping with transition metal (TM) atoms [104], etc. Among them, adsorption of TM atoms on graphene is one of the most explored approaches [105–112] due to its many unique advantages, such as easy observation and manipulation using scanning tunneling microscope, and relatively small influence to the crystalline quality of graphene. However, dilute ferromagnetism has not been realized in TM decorated graphene, mainly due to the following reasons: First, individual TM adatoms bind to graphene weakly. Therefore they will quickly diffuse and nucleate into sparsely distributed large clusters even at low temperatures, making it difficult to reach the magnetic percolation threshold. Second, upon adsorption on graphene, the magnetic moments of the TM atoms will be strongly suppressed, and in the case of Ni the moment is completely quenched [111, 112].

In this section, using first-principles approach based on DFT, we demonstrate that the *n-p* codoping method that we have shown in Chapter 2 [83–85, 222], can lead to significant enhancement in both the binding energy of TM adatoms to graphene and their magnetic moments. We first show that the TM adatoms (Fe, Co, and Ni), as *n*-type dopants in graphene, will strongly bind to the substitutional *p*-type dopant B [223–226] atoms due to electrostatic attraction, therefore suppressing the clustering

of the adatoms. Furthermore, the magnetic moments of all the three TM adatoms are found to be enhanced due to the doping effect by B. Particularly, Ni acquires a moment of  $0.57 \mu_B$ . We then find that, although Co-B or Fe-B codoping will likely open a band gap and thus hinder the long-range carrier-mediated magnetic interaction, Ni-B codoping preserves the Dirac band structure and has RKKY-like long-range magnetic interaction.

First-principles calculations were performed within the framework of DFT using the projector-augmented wave method as implemented in the Vienna *ab initio* simulation package code [125–127]. Generalized gradient approximation (PBE-GGA) was adopted [128] for treating exchange correlation interactions. The atomic structures were fully optimized until the Hellmann-Feynman forces on each ion were smaller than  $0.01 \text{ eV}/\text{\AA}$ . A plane-wave energy cut-off of 500 eV, a  $k$ -point grid of  $9 \times 9 \times 1$ , and the Gaussian smearing method with a smearing width of 0.1 eV were used in structure relaxation. A  $k$ -point grid of  $12 \times 12 \times 1$  was applied for final total energy calculations.

### 3.5.2 Enhancement in binding energies and magnetic moments of TM adatoms on graphene via $n$ - $p$ codoping

The adsorption energy  $E_{ad}$  of TM adatoms on graphene is defined as

$$E_{ad} = E_{TM} + E_G - E_{tot}, \quad (3.1)$$

where  $E_{TM}$  is the energy of an isolated TM atom,  $E_G$  is the energy of graphene (either pure or B-doped), and  $E_{tot}$  is the total energy of graphene with TM adsorption. As shown in Fig. 3.16 (a), for the adsorption sites of TM adatoms we only consider the hexagon-hollow sites [227, 228], denoted by  $H_n$ , whereas the sites of B substitution are denoted by  $S_n$ . In Fig. 3.16 (b) we show  $E_{ad}$  of an Fe adatom to graphene versus its distance from a B dopant. It is clear from the figure that the Fe adatom prefers

to stay close to the B dopant, which is due to the electrostatic attraction between the two dopants as revealed in the DMS case in the previous section. In Fig. 3.16 (c) we show the change in adsorption energy of three TM adatoms Fe, Co, and Ni on graphene after codoping with B. In all the three cases, the adsorption energies are significantly enhanced with B codoping, from 1.19, 1.32, and 1.55 eV [105, 107] to 2.17, 2.37, and 2.36 eV, respectively. Therefore the *n-p* codoping method can indeed help the TM adatoms to be more stabilized on graphene.

We next study the influence of B codoping on the magnetic moments of the TM adatoms. In Fig. 3.16 (d) the moments of TM adatoms on graphene before and after B codoping is shown. Again one can see that in all cases the moments are enhanced. For Fe and Co, the moment goes up from 2.03 and 1.12  $\mu_B$  to 2.82 and 1.92  $\mu_B$ , respectively. What is more interesting is the case of Ni, which has no magnetic moments if deposited alone on graphene, but acquires a moment of 0.57  $\mu_B$  with B codoping. In Fig. 3.16 (b) the magnetic moment of a Fe adatom versus its distance from a B dopant is also shown. The negligible dependence of the Fe moment on the separation between the Fe-B pair suggests that the moment enhancement is an doping effect rather than from the direct interaction between the *n-* and *p*-dopants.

### 3.5.3 Magnetic coupling between two *n-p* pairs

Now that large and stable magnetic moments from TM adatoms on graphene can be realized through B codoping, we next turn to the question that whether dilute ferromagnetism can be established in such *n-p* codoped graphene. Fig. 3.17 (b) shows the magnetic coupling strength between two *n-p* pairs, defined as the energy difference between ferromagnetic and antiferromagnetic configurations of the two moments. The positions of the *n-* and *p*-dopants are labeled in Fig. 3.17 (a), with one pair fixed at  $H_0-S_0$  and the other pair staying at  $H_1-S_1$ ,  $H_2-S_2$ ,  $H_3-S_2$ , etc. From Fig. 3.17 (b), two B-Fe pairs are antiferromagnetically coupled except at the nearest neighbor distance. Whereas two B-Co pairs are always antiferromagnetically coupled. Thus it is less

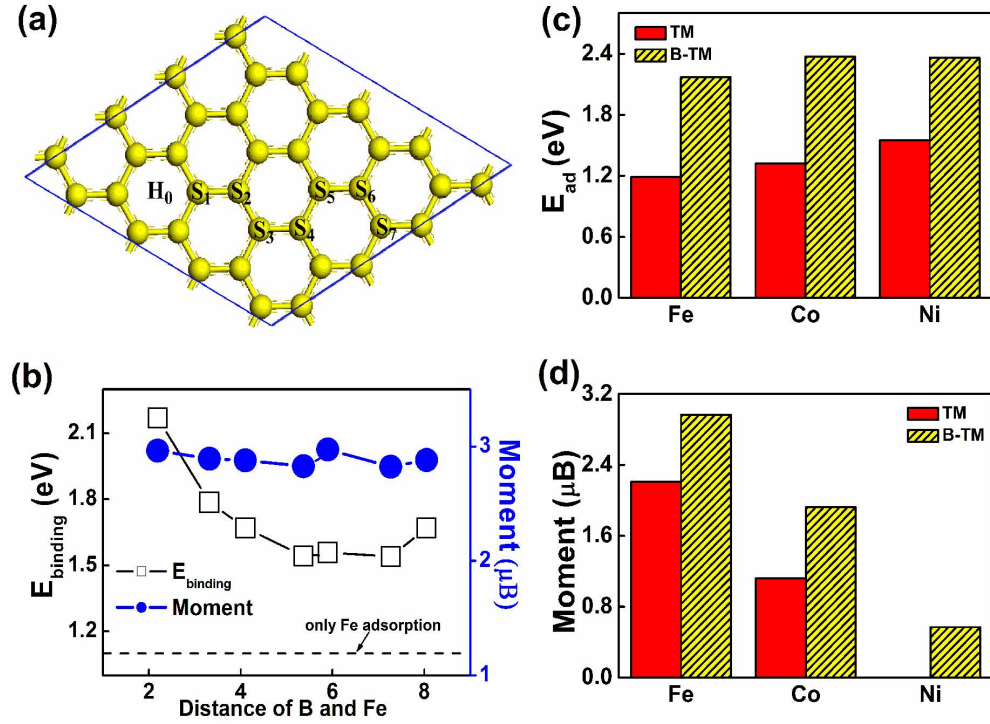


**Figure 3.16:** (a) A schematic plot of a  $n$ - $p$  pair in graphene.  $H_0$  represents a transition metal ( $n$ -type) adsorption site, while  $S_1$ - $S_7$  represent the positions of a substitutional B dopant ( $p$ -type). (b) Dependence of the binding energy and the magnetic moment of a Fe adatom on its distance from a B dopant. (c) and (d) Enhancement in binding energies and magnetic moments of transition metal atoms on graphene with  $n$ - $p$  codoping.

likely to achieve long-range ferromagnetic order in Fe-B or Co-B codoped graphene. However, for the case of Ni, the coupling oscillates between FM and AFM, and is FM in a relatively large range of separation between the two Ni-B pairs. Therefore, based on the experience from our study in the DMS systems, there is a hope to realize dilute ferromagnetism in Ni-B codoped graphene.

To better understand the magnetic interaction between the Ni-B pairs, in Figs. 3.18 we plot the density of states (DOS) of the FM configuration of two Ni-B pairs located at H<sub>1</sub>-S<sub>1</sub> and H<sub>1</sub>-S<sub>1</sub> as shown in Fig. 3.17 (a). Several observations are in order: First, the Dirac point still stays intact, and the Fermi level is still in the linear DOS region, which is desired for application utilizing the exotic Dirac charge carriers of graphene. The moderate *p*-doping, despite the large concentration of the Ni and B dopants, is due to the compensation nature of the *n-p* codoping approach. Second, there is a strong hybridization between the 2*p* orbitals of the C atoms and the 3*d* orbitals of the Ni adatoms, which indicates the strong exchange interaction between the graphene charge carriers and the *d* electrons of Ni, which is the origin of the magnetic moments. The strongly *p-d* hybridization is the origin of the long-range RKKY-like interaction between the Ni-B pairs. Third, the local DOS around a B dopant is very similar to that around a C atom in graphene, which indicates that B-doping can largely preserve the novel electronic structure of graphene. Therefore, the Ni-B codoped graphene is not only a promising system for realizing dilute ferromagnetism, but also largely preserves the Dirac-electron character of the charge carriers of graphene, which is ideal for spintronic applications.

### 3.5.4 Ongoing work

Similar to the previous section, we can also estimate the Curie temperature of the Ni-B codoped graphene, using a Monte Carlo approach based on a 2D diluted Heisenberg model with the magnetic coupling parameters calculated from DFT. Another problem to be addressed is why the Ni-B codoped graphene is different from the Fe-B or Co-B

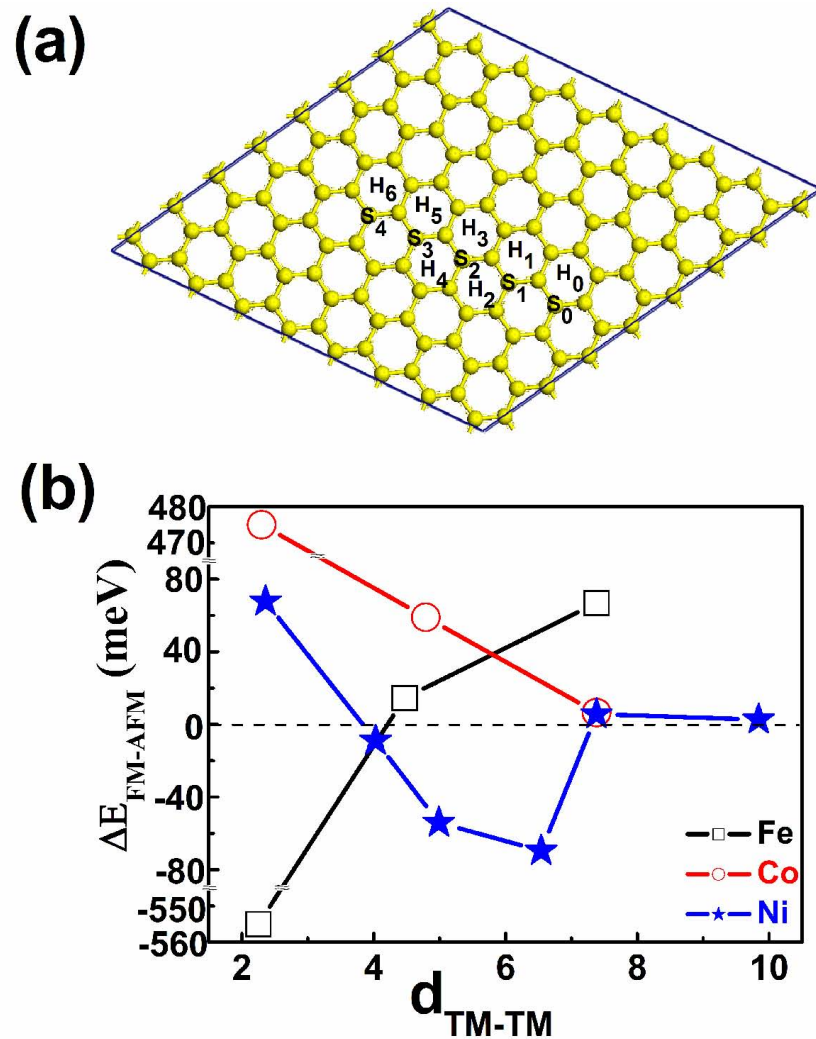


**Figure 3.17:** (a) Configurations of the  $n-p$  pairs considered in the calculation of magnetic coupling between two pairs.  $H_0-H_6$  represent adsorption sites of transition metal atoms,  $S_0-S_4$  represent the positions of B substitution. The first  $n-p$  pair is at the position  $H_0-S_0$ . (b) The magnetic coupling strength between two  $n-p$  pairs versus their separation.

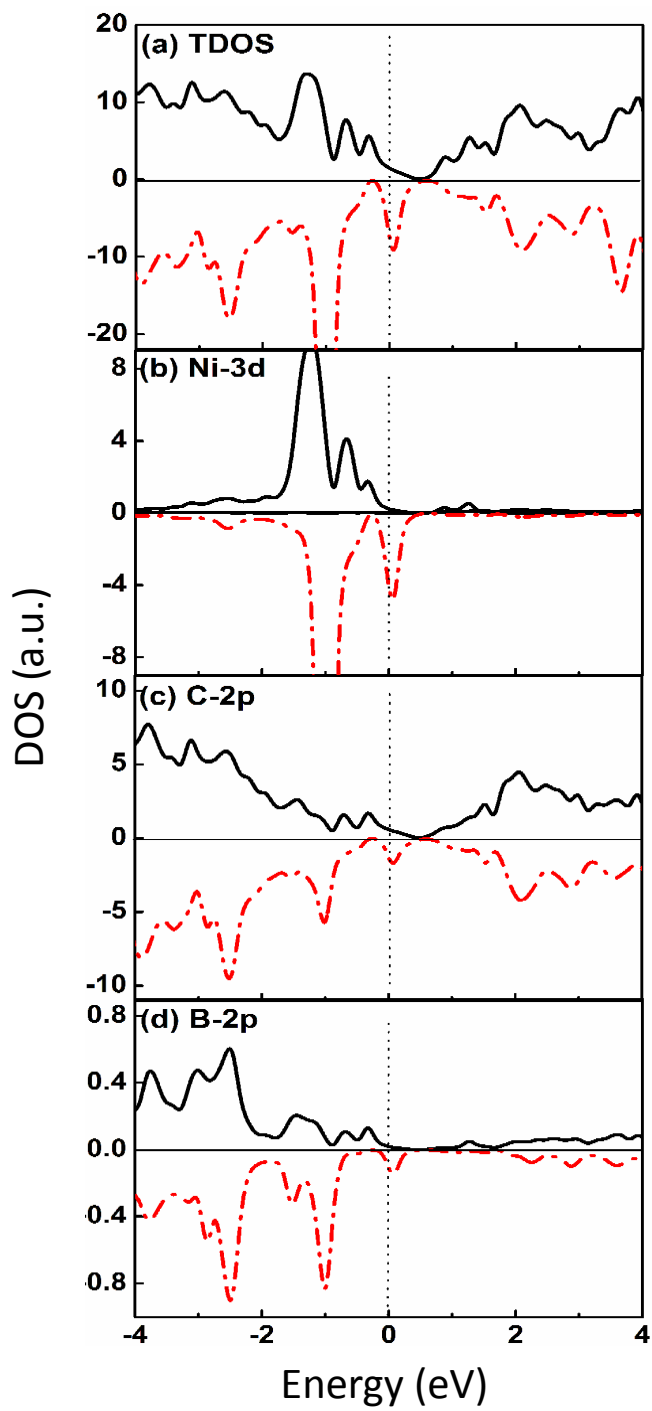


**Figure 3.18:** DOS and PDOS plots of the  $\text{H}_0\text{S}_0\text{-H}_3\text{S}_2$  configuration shown in Fig. 3.17 (a).

codoped graphene in the behavior of the magnetic coupling. The reason may lie in the details of the  $p$ - $d$  hybridization between the TM adatoms and graphene.

# Chapter 4

## Topological Insulator Heterostructures

### 4.1 CO Oxidation Facilitated by Robust Surface States on Au-Covered Topological Insulators

#### 4.1.1 Introduction

Surface states [18, 19] can be present in many systems, e.g., the free-electron like states on the (111) surfaces of noble metals [229], and the dangling bond derived states on semiconductor surfaces [230]. Aside from their spatial proximity, the *sp*- or *d*-band derived surface states can be located at or near the Fermi level ( $E_F$ ) in energy space; consequently they can significantly influence the physical and chemical processes happening at the surfaces [20, 22, 231, 232]. However, since they arise as a result of the different bonding environment at the surface from the bulk [18], normal surface states are easily destroyed by local modifications at the surfaces, e.g., presence of impurities, surface defects, surface reconstruction, or a change in the surface termination or orientation. This fundamental limitation has prohibited

systematic studies of the potential role of surface states in surface reactions and catalysis, especially in more realistic environments.

In contrast, the exotic metallic TSS of the recently discovered three-dimensional topological insulators (3DTI) [233–236] are exceptionally robust compared to conventional surface states. The TSS arise from the nontrivial topology of the electron bands of the 3DTI, and their persistence is protected by time-reversal symmetry. Therefore, the TSS are insensitive to the structural details of the surface [237, 238], and will persist as long as the bulk band gap embodying the TSS remains open. The robust TSS thus provides a perfect platform for investigating the catalytic role of surface states in less constrained environments.

In this section, we focus on CO oxidation by supported Au films, a prototype system of fundamental and practical importance in heterogeneous catalysis [239–242]. The use of the 3DTI  $\text{Bi}_2\text{Se}_3$  [3, 243] as the substrate, instead of conventional oxides such as  $\text{TiO}_2$  or  $\text{MgO}$ , is to introduce additional surface electron states (the TSS) at  $E_F$ . As shown recently for the case of metal-induced semiconductor surface reconstruction [21], such extra states may serve as an electron bath to significantly modify the bonding configurations on the surface through proper static electron transfer.

### 4.1.2 Methods

Our density functional calculations are carried out using the Vienna *ab initio* simulation package (VASP) [125] with PAW potentials [126, 127] and the generalized gradient approximation (PBE-GGA) [128] for exchange-correlation functional. The lattice constants of  $\text{Bi}_2\text{Se}_3$  are adopted from experiments. The generic  $\text{Bi}_2\text{Se}_3$  substrate is modeled by a slab of 15 atomic layers or 3 quintuple layers (QL), and a Bi-terminated substrate is realized by removing one outermost Se layer. The vacuum layers are over 20 Å thick to ensure decoupling between neighboring slabs. During relaxation, atoms in the lower 11 atomic layers are fixed in their respective bulk

positions, and all the other atoms are allowed to relax until the forces on them are smaller than  $0.01 \text{ eV}/\text{\AA}$ . A  $7\times 7\times 1$   $k$ -point mesh is used for the  $1\times 1$  surface unit cell, and  $3\times 3\times 1$  for the  $2\times 2$  surface unit cell [167].

#### 4.1.3 TSS on Au-covered $\text{Bi}_2\text{Se}_3$ surface

Crystalline  $\text{Bi}_2\text{Se}_3$  has rhombohedral structure and its unit cell is composed of 3 weakly coupled QL, each of which comprises of 5 alternating Bi and Se layers in a sequence Se-Bi-Se-Bi-Se [3, 243]. The naturally cleaved surface is therefore the Se surface. In Fig. 4.1 (a) we plot the band structure around  $E_F$  of a naturally cleaved 3 QL  $\text{Bi}_2\text{Se}_3$  film. The surface states in the bulk band gap ( $\sim 0.3 \text{ eV}$ ) have close to linear dispersion near  $E_F$ . This single “Dirac-cone” like band structure is a distinctive feature of the TSS of  $\text{Bi}_2\text{Se}_3$  [3, 243]. The small gap ( $\sim 50 \text{ meV}$ ) opened at the Dirac point is due to the coupling between the two degenerate TSS on the two surfaces of a very thin 3DTI film [244].

We use the Bi-terminated surface of  $\text{Bi}_2\text{Se}_3$ , to which Au binds more strongly than the naturally cleaved Se surface, to support Au atoms without formation of 3D Au clusters [241]. Experimentally it is possible to intentionally introduce a large amount of Se vacancies on the surfaces of  $\text{Bi}_2\text{Se}_3$  or eventually form a complete Bi-terminated surface, due to the large vapor pressure difference between Bi and Se [244]. We therefore can use the ideal Bi-terminated surface in the present proof-of-principle study. The band structure of the Bi-terminated film is shown in Fig. 4.1 (b). The two TSS Dirac bands still robustly persist and shift below  $E_F$ , agreeing with experiments [3, 237]. Additionally, the degeneracy of the two Dirac bands is lifted, of which the upper and lower bands correspond to the TSS at the upper (Bi-terminated) and lower (Se-terminated) surface, respectively.

We choose 2 monolayers (ML) of Au deposited on the Bi surface of the  $\text{Bi}_2\text{Se}_3$  film [Fig. 4.1 (c) inset] as a model system because of its optimal stability for subsequent calculations. Here 1 ML is defined to be the same number of atoms as that in each

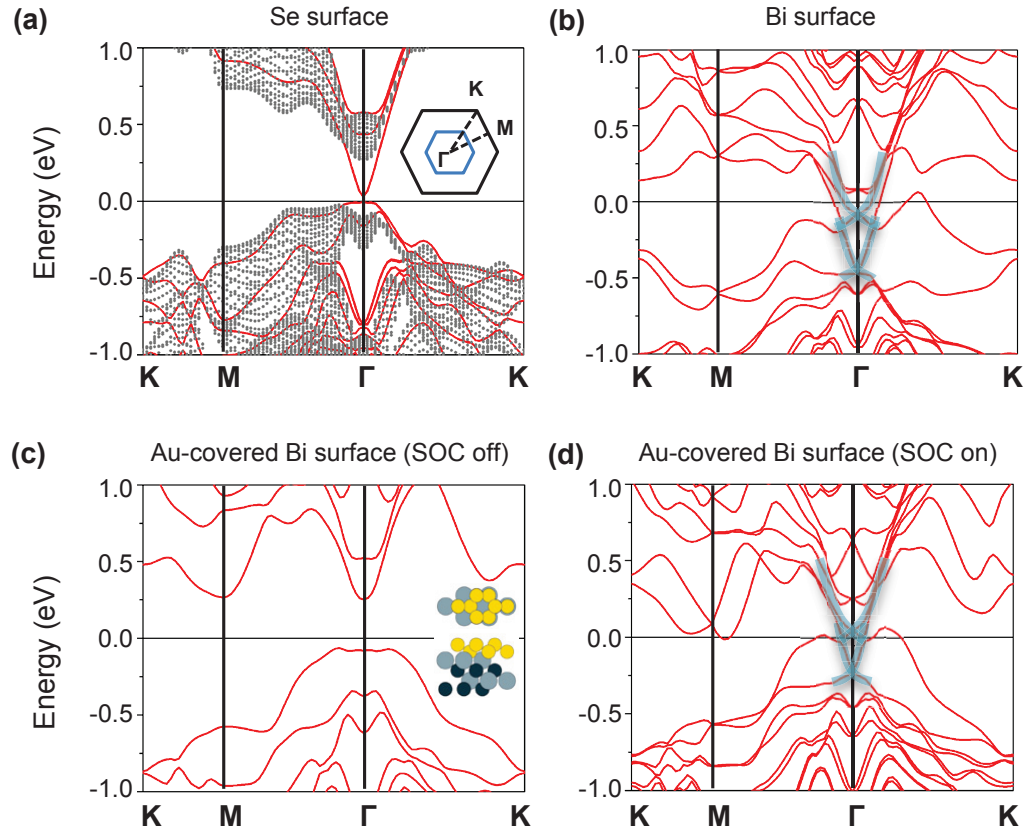


**Figure 4.1:** (a) Band structure of a 3 QL  $\text{Bi}_2\text{Se}_3$  film, where the shaded area is the bulk band structure projected to the 2D Brillouin zone. The inset shows the shape of the 2D Brillouin zone for different surface unit cells (Black solid lines- $1 \times 1$ ; blue solid lines- $2 \times 2$ ). (b) Band structure of a Bi-terminated  $\text{Bi}_2\text{Se}_3$  film. (c) and (d) Band structures of 2 ML Au deposited on the Bi-terminated surface without and with SOC, respectively. In (b) and (d) the TSS are highlighted by the transparent blue lines. The inset in (c) shows the top and side views of the structure (only top 4 atomic layers of  $\text{Bi}_2\text{Se}_3$  are shown). Yellow balls-Au; light blue balls-Bi; dark blue balls-Se.

atomic layer of  $\text{Bi}_2\text{Se}_3$ , which is equal to 0.48 times the atom density in a (111) layer of bulk Au. Figs. 4.1 (c) and (d) show the band structures of the Au-covered  $\text{Bi}_2\text{Se}_3$  film without and with spin-orbit coupling (SOC), respectively. Two TSS Dirac bands emerge only when the SOC is switched on, confirming that the TSS indeed originates from the SOC of the bulk states [233, 234]. This observation allows us to conveniently isolate the effects of the TSS by comparative studies with and without SOC. The shape of the two TSS bands near the  $\Gamma$  point closely resembles that of the TSS in Fig. 4.1 (b) for the Bi-terminated  $\text{Bi}_2\text{Se}_3$  film despite the slight shift in their relative positions in energy. Therefore the TSS survives even if the  $\text{Bi}_2\text{Se}_3$  surface is completely buried under the 2 ML Au film.

#### 4.1.4 “Electron bath” effect of TSS in promoting surface reactions

The CO binding energies on the model system with and without SOC, calculated as  $\Delta E = E_{\text{adsorbate+substrate}} - E_{\text{adsorbate}} - E_{\text{substrate}}$ , are listed in Table 4.1. With SOC, the binding energy is considerably enhanced by 0.2 eV compared to that without SOC, accompanied by a decrease of the C-Au bond length from 2.029 Å to 1.981 Å. The enhanced CO binding with SOC is due to the static electron transfer facilitated by the TSS. To see this effect we first compare the local density of states (LDOS) on the C atom of an adsorbed CO with and without SOC, shown in Fig. 4.2 (a). The antibonding  $2\pi^*$  states shift to higher energies with SOC, indicating decreased electron occupation, and hence enhanced CO-Au binding [26, 245]. On the other hand, from Fig. 4.2 (c), the top Dirac band, corresponding to the TSS on the Au-deposited Bi-terminated surface, shifts to lower energy after the adsorption of CO, indicating increased electron occupation. Taken together, net electrons are transferred to the TSS serving as an electron bath when CO is adsorbed on the surface.

The enhanced CO binding with SOC is not due to Au, though Au does have large SOC. To see this we consider two comparative cases: One is fixing the 2 ML Au film in

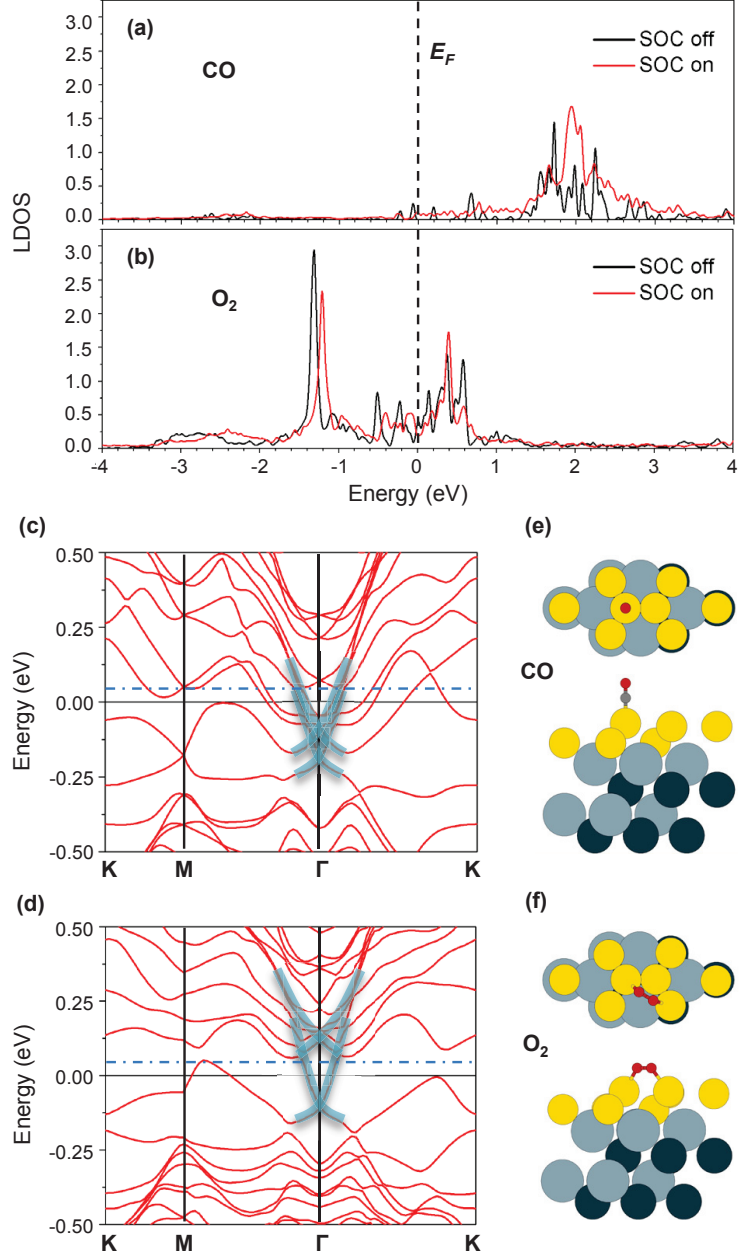


**Figure 4.2:** (a) and (b) LDOS on the C atom of CO, and one O atom of  $O_2$ , featuring the energy range corresponding to the  $2\pi^*$  states of CO and  $O_2$ , respectively. (c) and (d) Band structures of the CO and  $O_2$  adsorbed 2 ML Au-Bi<sub>2</sub>Se<sub>3</sub> film, shown in a reduced Brillouin zone corresponding to the  $2\times 2$  surface unit cell [Fig. 4.1 (a) inset]. The TSS bands are highlighted by the transparent blue lines. The blue dot-dash lines indicate the position of the upper Dirac point in Fig. 4.1 (d). The upper and lower panels in (e) and (f) are the top and side views of the atomic structures. Small red balls-O; small gray balls-C; yellow balls-Au; light blue balls-Bi; dark blue balls-Se.

**Table 4.1:** Binding energies (in eV) of CO and O<sub>2</sub> on three comparative substrates. (1) 2 ML Au on Bi-terminated Bi<sub>2</sub>Se<sub>3</sub>, (2) freestanding 2 ML Au fixed in the same geometry as in (1), and (3) (unreconstructed) Au(111) surface. The CO/O<sub>2</sub> coverage is 1/4 ML in (1) and (2), and 1/16 ML in (3). The geometries of adsorbed CO and O<sub>2</sub> are shown in Figs. 4.2 (e) and (f), respectively.

		(1) Au-Bi <sub>2</sub> Se <sub>3</sub>	(2) 2 ML Au	(3) Au(111)
CO	SOC	0.49	0.95	0.30
	No SOC	0.29	0.92	0.27
O <sub>2</sub>	SOC	0.23	0.52	<0.01
	No SOC	0.07	0.49	<0.01

vacuum with the Bi<sub>2</sub>Se<sub>3</sub> substrate removed; the other is the unreconstructed Au(111) surface. The Au(111) surface is modeled by a 4 layer slab, each layer comprising of 16 Au atoms, with the lower 2 layers fixed. From Table I, the CO binding energy differences with and without SOC are about one order of magnitude smaller ( $\sim 0.03$  eV) in these two latter cases. We also note that with SOC the CO binding energy on the Au-Bi<sub>2</sub>Se<sub>3</sub> system is much larger than that on Au(111). Based on these results, we conclude that the TSS of the underlying Bi<sub>2</sub>Se<sub>3</sub> enhance the CO binding by accepting the electrons that otherwise would have been transferred to the antibonding states of the CO-Au system.

Next we show that the TSS as an electron bath can also enhance the adsorption of O<sub>2</sub>, but by invoking a different direction of static electron transfer. On the Au-Bi<sub>2</sub>Se<sub>3</sub> substrate, O<sub>2</sub> binding energy increases by 0.16 eV with SOC, which is also much larger than that on the freestanding Au film or Au(111) surface (Table 4.1). The LDOS on one O atom of O<sub>2</sub> is shown in Fig. 4.2 (b). The two groups of peaks below and above  $E_F$  correspond to the spin-up and spin-down antibonding  $2\pi^*$  states, respectively [246]. As the half-filled  $2\pi^*$  states hybridize with the Au  $d$  states, more electrons will be transferred to the  $2\pi^*$  states and promote O<sub>2</sub> toward dissociation [246, 247]. At the same time, the spin splitting of the  $2\pi^*$  states will decrease due to the weakened O-O bond. In Fig. 4.2 (b), both groups of the

spin-split peaks shift toward  $E_F$  after turning on SOC, indicating decreased spin splitting in the O<sub>2</sub> orbitals. Meanwhile, the O-O bond length increases from 1.289 Å without SOC to 1.299 Å with SOC. The increased electron occupation of the 2π\* states upon switching on SOC is not easily visible from Fig. 4.2 (b), but is confirmed by the calculated increase in the relative spectral weight of the 2π\* DOS below  $E_F$ , equal to 0.56 with SOC and 0.55 without SOC. This difference is roughly equal to 0.04 e per O<sub>2</sub> molecule, originated from the TSS. On the other hand, from Fig. 4.2 (d), the top TSS Dirac band shifts upward compared to that without O<sub>2</sub> adsorption, indicating that electrons are transferred out of the TSS. Therefore, rather than accepting electrons as in the case of CO, the TSS now donates electrons and promotes O<sub>2</sub> toward dissociative adsorption on Au. Moreover, the adsorption energy of O<sub>2</sub> is now comparable to that of CO with a moderate strength, which is a desirable feature for easier reaction and high catalytic activity.

In studying adsorption of molecules on transition metal surfaces, the prevailing theoretical framework has been the *d*-band theory, according to which the chemical activity of a metal substrate is correlated with the position of its *d*-band center ( $E_d$ ) in the energy spectrum [26, 245]. Specifically, the closer  $E_d$  of the metal substrate is to  $E_F$ , the stronger molecular adsorbates bind to the substrate. A major contribution to the energy gain as  $E_d$  shifts up toward  $E_F$  is from the decreased filling of the adsorbate's antibonding states as they are “pushed away” from  $E_F$  by the *d* bands. To see whether our results can be explained independently by the *d*-band theory, we have calculated  $E_d$  of Au in the top layer of the 2 ML Au film [Figs. 4.3 (a) and (b)] as

$$E_d = \frac{\int_{-\infty}^{\infty} PDOS_d(E) \times (E - E_F) dE}{\int_{-\infty}^{\infty} PDOS_d(E) dE}, \quad (4.1)$$

where  $PDOS_d$  is the density of states projected to the *d* orbital of Au. We find that, in the present case,  $E_d$  actually shifts down away from  $E_F$  by 0.21 eV (from -2.68 eV to -2.89 eV) after switching on SOC, and the shift is even larger than that of the

freestanding 2 ML Au film, which is 0.12 eV to the same direction (from -2.57 eV to -2.69 eV). These findings unambiguously rule out the *d*-band theory to be mainly operative in the present systems.

#### 4.1.5 Discussion and conclusion

An implicit assumption of the *d*-band theory is that the *sp* states around  $E_F$  do not differ much among different systems. However, our present study offers a striking and unique counter example to this assumption. In particular, since these TSS are gapless and not completely filled, they can readily donate or accept electrons in order to lower the total energy upon molecular adsorption [see illustrations in Figs. 4.3 (c-e)]. Such *sp*-band derived states near  $E_F$ , either due to extrinsic effects such as the 3DTI substrate studied here or associated with the transition metals themselves, can play a prominent role in surface reactivity, especially for late transition metals with deeper *d* bands. Furthermore, the delocalized *sp* surface states may also help to smooth the energy profile of the surface and lower the diffusion and reaction barriers of the adsorbed molecules [20, 231], an intriguing aspect worth future investigations. The present study indicates manipulation of the *sp* surface states may be complementary to the guiding principles from *d*-band theory in searching and designing new catalysts, and 3DTI materials may offer rich opportunities for this purpose.

### 4.2 Precise Tuning of the Vertical Location of Helical Surface States in Topological Insulator Heterostructures via Dual-Proximity Effects

#### 4.2.1 Introduction

In the previous subsection, we were essentially playing with the robustness of the topological surface states, but did not really focus on the TSS itself. An especially

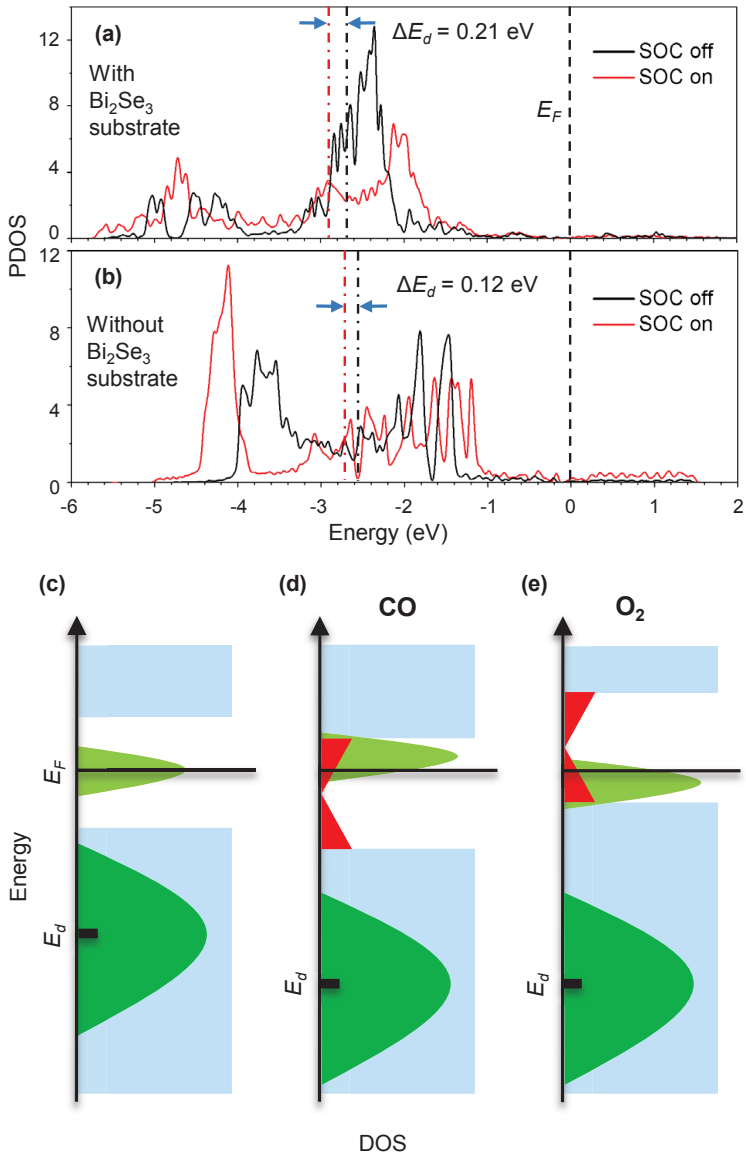


**Figure 4.3:** (a) and (b) PDOS of an Au atom in the top layer of the 2 ML Au film with and without  $\text{Bi}_2\text{Se}_3$  substrate, respectively. In (b) the Au film is fixed in space. The red and black dot-dash lines indicate the positions of  $E_d$  with and without SOC, respectively. (c-e) Illustration of the role of the TSS in molecular adsorption. Blue-valence and conduction bands of the 3DTI support; light green-antibonding states of adsorbed molecules; red-TSS; dark green-metal  $d$  bands. (c) Without the TSS, the support will not be involved in the static electron transfer. (d) and (e) With the TSS, electrons of the molecule-metal system can be transferred either to or from the partially filled metallic surface states, depending on which way can lower the total energy.

interesting problem in the studies of TI is how the TSS will behave when a TI is hybridized with other materials, and a number of peculiar quantum phenomena have been discovered in such TI-based heterostructures, such as Majorana fermions induced by the superconducting proximity effect [33], topological magnetoelectric effect [34], quantized anomalous Hall effect [35], etc.

In this section, we will reveal a new degree of freedom in the tunability of the TSS properties, namely, its vertical location perpendicular to the surface, as a conventional insulator (CI) overlayer is placed onto a TI substrate. We establish this intriguing and highly desirable tunability using ultrathin (single stoichiometric layer) films of CIs ( $ZnM$ ,  $M = S$ , Se, and Te) on  $Bi_2Se_3$  or  $Bi_2Te_3$  as specific examples, and the concepts established are expected to be applicable when thicker overlayers are used. We show that, because of the strong influence of the interaction with TI on the electronic properties of the ultrathin CI films, the latter may undergo a nontrivial topological phase transition, implied by the relocation of the TSS from the TI/CI interface to the top of the CI film [Fig. 4.4 (a)]. Furthermore, the TSS can also be manipulated to stay put at the TI/CI interface [Fig. 4.4 (b)] by tuning one or more key properties of the CI to be out of the window for topological phase transition. Most strikingly, we discover a reverse-proximity effect: The top quintuple layer (QL) of the TI may even be driven by the CI film to a topologically trivial phase, implied by a spatial shift of the TSS toward the inside of the TI [Fig. 4.4 (c)].

#### 4.2.2 Methods

All the density functional calculations were carried out using the Vienna *ab initio* simulation package (VASP) [125] with projector-augmented-wave potentials [126, 127] and the Perdew-Burke-Ernzerhof [128] generalized gradient approximation for exchange-correlation functional. The lattice constants of  $Bi_2Se_3$  and  $Bi_2Te_3$  were adopted from experiments. The generic  $Bi_2Se_3$  and  $Bi_2Te_3$  substrate was modeled by a slab of 32 atomic layers or 6 QLs. The semiconducting overlayers  $ZnM(111)$

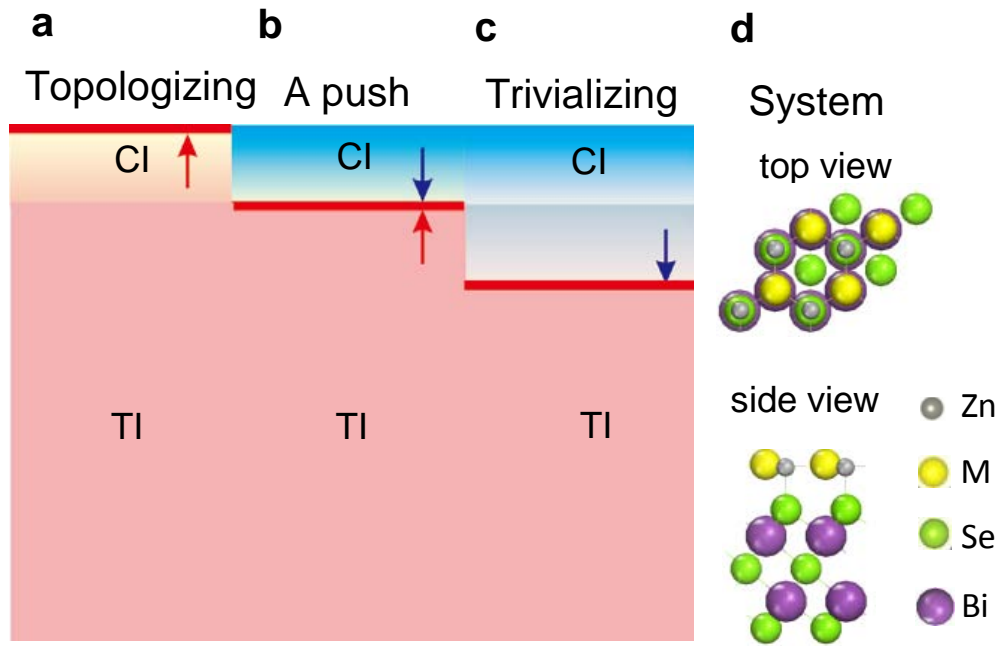


**Figure 4.4:** Schematic illustration on tuning the vertical location of the topological surface states (TSS) as a topological insulator (TI) is covered with a layer of conventional insulator (CI). (a) TSS Floating to the top of the CI. (b) Staying put at the CI/TI interface. (c) Diving into the TI. (d) The atomic structure of  $ZnM/Bi_2Se_3$  ( $M = S, Se, Te$ ). The red lines denote the TSS; the arrows indicate the resulting directions of the topological phase transition.

( $M = \text{S, Se, Te}$ ) were epitaxially placed on the (0001) surface of the TIs, and the energetically most stable configuration is obtained by putting Zn directly above Se, and M in the hcp sites, with the Zn face adjacent to the  $\text{Bi}_2\text{Se}_3$  surface [Fig. 4.4 (d)]. The vacuum layers used are over 20 Å thick to ensure decoupling between neighboring slabs. During structural relaxation, atoms in the TI substrate were fixed in their respective bulk positions, and all the other atoms in the semiconducting overlayer were allowed to relax until the forces on them are smaller than 0.01 eV/Å. A  $7 \times 7 \times 1$   $k$ -point mesh was used for the  $1 \times 1$  surface unit cell [167].

#### 4.2.3 Proximity effects in $\text{ZnS}/\text{Bi}_2\text{Se}_3$ and $\text{ZnSe}/\text{Bi}_2\text{Se}_3$

A bulk  $\text{Zn}M$  ( $M = \text{S, Se, and Te}$ ) material crystallizes in a zincblende structure (space group  $Fd - 3m$ ), with their (111) surface geometry matching well with the (0001) surface of  $\text{Bi}_2\text{Se}_3$ . The lattice mismatch between  $\text{Zn}M(111)$  and  $\text{Bi}_2\text{Se}_3(0001)$  is +8.4%, +3.5%, and -3.9% for  $M = \text{S, Se, and Te}$ , respectively, where “+” or “-” denotes tensile or compressive strain. Another advantage of using the  $\text{Zn}M$  family is that they span a considerable range of the key property parameters such as the SOC and band gap (Table 4.2). As proof of principles, here we limit ourselves to the cases where a single stoichiometric  $\text{Zn}M$  layer is deposited on TI substrate [Fig. 4.4 (d)].

**Table 4.2:** Characteristic properties and vertical locations of the TSS in different CI/TI heterostructures. The values for the band gap ( $E_g$ ), spin-orbit splitting ( $\Delta_{SO}$ ), and work function ( $\Phi$ ) are obtained for free-standing single-layered CIs; the bulk lattice constants ( $a$ ) of the CI are from experiments. The last three columns indicate the lattice mismatch ( $\Delta a$ ), binding energy ( $E_b$ ) between the CI and TI, and the location of the TSS ( $Z$ ). The values in the square brackets are the corresponding values for the TI substrates.

System(Substrate)	$E_g$ (eV)	$\Delta_{SO}$ (eV)	$\Phi$ (eV)	$a$ (Å)	$\Delta a$	$E_b$ (eV)	$Z$
$\text{ZnS} (\text{Bi}_2\text{Se}_3)$	1.82 [0.40]	0.03	6.10 [5.55]	3.82 [4.14]	+8.4%	0.06	Interface
$\text{ZnSe} (\text{Bi}_2\text{Se}_3)$	1.58 [0.40]	0.20	5.77 [5.55]	4.00 [4.14]	+3.5%	0.09	Top
$\text{ZnTe} (\text{Bi}_2\text{Se}_3)$	1.85 [0.40]	0.55	3.98 [5.55]	4.31 [4.14]	-3.9%	0.29	Inside
$\text{ZnTe} (\text{Bi}_2\text{Te}_3)$	1.39 [0.39]	0.48	4.93 [5.00]	4.31 [4.38]	+1.6%	0.19	Top

Figs. 4.5 (a-c) display the atom-resolved band structure of ZnS/Bi<sub>2</sub>Se<sub>3</sub>. The Dirac points of the TSSs are still located at the Fermi level, indicating a negligible charge transfer between the ZnS film and Bi<sub>2</sub>Se<sub>3</sub>. Although the existence of the Dirac points is guaranteed by time reversal symmetry, away from the  $\Gamma$  point, the degeneracy of the two TSSs from the two surfaces of the TI slab is lifted, due to the interaction between the ZnS film and the upper surface of the Bi<sub>2</sub>Se<sub>3</sub>. To find out the spatial location of the TSS, we plot the atom-specific character of each band, as indicated by the dots superposed onto the band structure. It is apparent from Figs. 4.5 (b) and (c) that the Dirac-cone like TSS bands are localized in the 1st QL (upper surface) and 6th QL (lower surface) of the Bi<sub>2</sub>Se<sub>3</sub>, whereas from Fig. 4.5 (a) the TSS has negligible weight in the ZnS film. The real-space density of states of the upper-surface TSS at the Dirac point [Fig. 4.5 (d)] also confirms this identification. Therefore, the ZnS/Bi<sub>2</sub>Se<sub>3</sub> system can be regarded as the same as a bare Bi<sub>2</sub>Se<sub>3</sub> film placed in the air, in the sense that the ZnS film is a topologically trivial CI just like the vacuum, and hence the TSS in essence stays put at the surface of the Bi<sub>2</sub>Se<sub>3</sub>.

The same analysis yields very different behaviors for the system of ZnSe/Bi<sub>2</sub>Se<sub>3</sub>, shown in Figs. 4.5 (e-h). Compared to the former case of ZnS/Bi<sub>2</sub>Se<sub>3</sub>, the upper-surface TSS now shifts downward in energy due to enhanced charge transfer from ZnSe to Bi<sub>2</sub>Se<sub>3</sub>, which can be qualitatively understood from the smaller work function of the ZnSe film than that of ZnS (see Table 4.2). However, the most interesting difference between the present system and the former one is that, from Fig. 4.5 (e), a considerable weight of the TSS is carried by the ZnSe film, which is also unambiguously confirmed by the real space density of states of the TSS in Fig. 4.5 (h). Because a TSS marks the boundary between topologically inequivalent phases of matter, the upward shift of the TSS to the surface of the ZnSe overlayer indicates that the ZnSe has experienced a topological phase transition from its CI state to TI state, or in other words, being “topologized” by the TI via proximity effect.

We now discuss the underlying physical origin of the contrasting behaviors of the TSS in ZnS/Bi<sub>2</sub>Se<sub>3</sub> and ZnSe/Bi<sub>2</sub>Se<sub>3</sub>. Since the nontrivial topology of the electronic

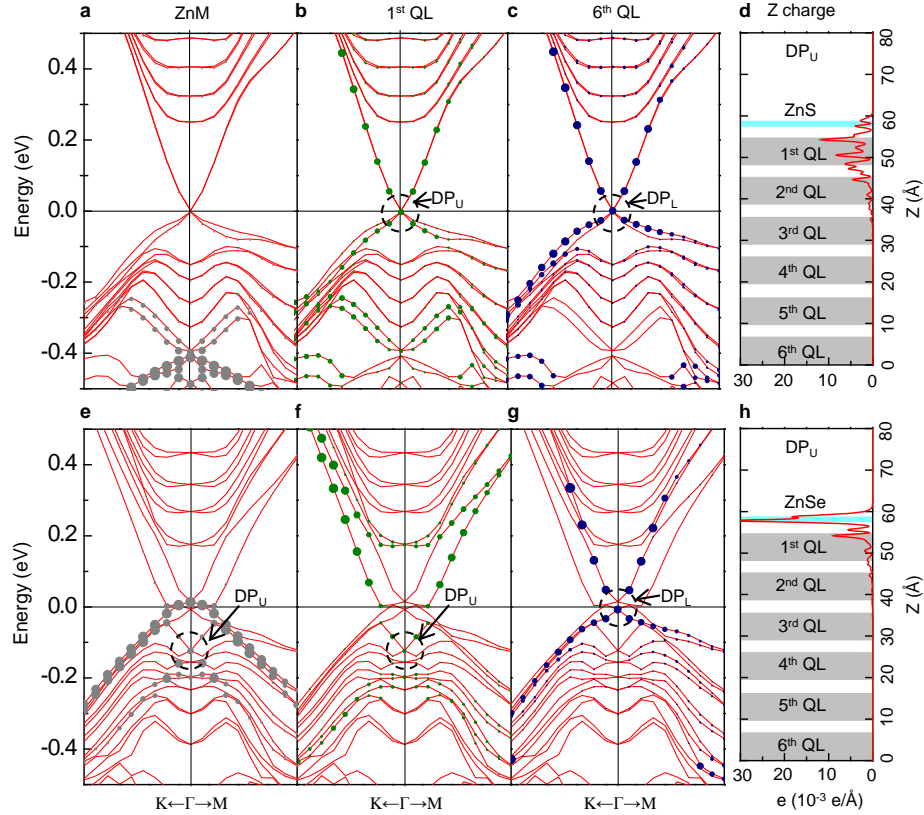


**Figure 4.5:** Band structures of ZnS/Bi<sub>2</sub>Se<sub>3</sub> (upper row) and ZnSe/Bi<sub>2</sub>Se<sub>3</sub> (lower row) along the K- $\Gamma$ -M direction. The dots indicate the electronic bands contributed by the CI [(a) and (e)], the 1st QL of the TI [(b) and (f)], and the 6th QL [(c) and (g)], respectively; the sizes and colors of the dots also indicate different spectral weights and contributions from different atoms, respectively. (d) and (h) show the charge density distribution of the upper-surface TSS at the  $\Gamma$  point marked by the circle and indicated by DP<sub>U</sub>. The DP<sub>U/L</sub> stands for the Dirac point at the upper/lower surface. The grey and cyan bars denote the locations of the different QLs and the CI, respectively.

structure of  $\text{Bi}_2\text{Se}_3$  is ascribed to its strong SOC and small bulk band gap, it is intuitive that these factors associated with the CI materials are also essential for the different topological proximity effects we just observed. Indeed, the bulk phase of ZnSe has a much larger SOC (0.12 eV compared to 0.02 eV) and smaller band gap (1.20 eV compared to 2.09 eV) than ZnS, and the trend is preserved for the single-layer films as well (see Table 4.2), making ZnSe “more proximate” to a TI material property-wise. Thus the term “proximity effect” here carries a dual meaning of both spatial and property-wise closeness. To gain a deeper understanding of the roles played by these key parameters of the  $\text{Zn}M$ , we look into the band structures of the two heterostructures [Figs. 4.5 (a), (e)]. In the ZnSe/ $\text{Bi}_2\text{Se}_3$  case [Fig. 4.5 (e)], one can see that the SOC-induced gap ( $\Delta_{SO}$ ) within the valence band of the ZnSe is aligned with the energy range of the TSS, and the TSS is mainly derived from the lower branch of the split bands. Such an optimal band alignment is essential for the topological proximity effect to take place. In contrast, for ZnS/ $\text{Bi}_2\text{Se}_3$ , the bulk gap (and correspondingly the TSS) of the TI falls completely within the gap of the CI film [see Figs. 4.5 (a-c)]; consequently, the bands from the ZnS and  $\text{Bi}_2\text{Se}_3$  are only mutually weakly perturbed. This “bad” alignment in the sense of absent proximity effect is partly due to the much larger band gap of ZnS than that of ZnSe, and partly because of the smaller mismatch between the work functions of the ZnS film and  $\text{Bi}_2\text{Se}_3$  substrate than that in the ZnSe/ $\text{Bi}_2\text{Se}_3$  case (Table 4.2). As an alternative view, the seemingly trivial case of ZnS/ $\text{Bi}_2\text{Se}_3$  in essence represents a balanced outcome of precise tuning, where one or more of the key CI parameters are pushed out of the range for the topological phase transition to take place.

#### 4.2.4 Reverse proximity effect in $\text{ZnTe}/\text{Bi}_2\text{Se}_3$

With these competing factors in mind, we next look into the system of  $\text{ZnTe}/\text{Bi}_2\text{Se}_3$ . Since ZnTe has an even larger SOC and a smaller bulk band gap than that of ZnSe, we expected to see an even more pronounced relocation of the TSS to the top of the

ZnTe film. However, as a counterintuitive surprise, the upper-surface TSS now has a reverse shift toward the inner of  $\text{Bi}_2\text{Se}_3$ , with its peaked density located on the top of the 2nd QL [Figs. 4.6 (a-e)].

To reveal the physical origin of this unexpected reverse-proximity effect, we first notice that, from Figs. 4.6 (a-d), both the bulk bands of  $\text{Bi}_2\text{Se}_3$  and the TSS have a more noticeable downward shift in energy compared to the case of  $\text{ZnSe}/\text{Bi}_2\text{Se}_3$ , while the ZnTe film becomes strongly *p*-doped, indicating the most pronounced charge transfer from the CI overlayer to the TI substrate among the three cases. This behavior can be understood from the much smaller work function of the ZnTe film than that of ZnSe. The concomitant misalignment between the TSS and valence band top of ZnTe prevents the ZnTe film from being topologized by the  $\text{Bi}_2\text{Se}_3$  substrate, as we have discussed before. Moreover, because of the significant charge transfer, the binding energy between the ZnTe film and the  $\text{Bi}_2\text{Se}_3$  substrate (Table 4.2) is much larger (0.29 eV) than the other two systems (<0.1 eV). Since the QLs of  $\text{Bi}_2\text{Se}_3$  are mutually coupled through weak van der Waals-like interactions, such a strong coupling between the ZnTe film and the 1st QL will compete with and weaken the interaction between the 1st and 2nd QL. Therefore, not only being unable to be topologized by the  $\text{Bi}_2\text{Se}_3$  substrate, but the ZnTe film also forces the 1st QL of the TI to be electronically partially decoupled from the remaining QLs. Furthermore, because one QL of  $\text{Bi}_2\text{Se}_3$  does not have gapless TSS [244], the upper-surface TSS will naturally be relocated to the top of the 2nd QL. In other words, the CI has prevailed by topologically “trivializing” the 1st QL of the TI via a reverse-proximity effect.

To provide further support of the physical picture above, we have performed two additional comparative studies. In the first one, we kept the relative positions of the ZnTe film and the 1st QL of  $\text{Bi}_2\text{Se}_3$  fixed, and increased the distance between the 1st and 2nd QL from 2.5 Å to 3 Å, hence further decreasing their coupling. As shown in Figs. 4.6 (f-j), the TSS now becomes even more localized on top of the 2nd QL. In the second one, we fixed all the QLs of  $\text{Bi}_2\text{Se}_3$  and slightly increased the distance

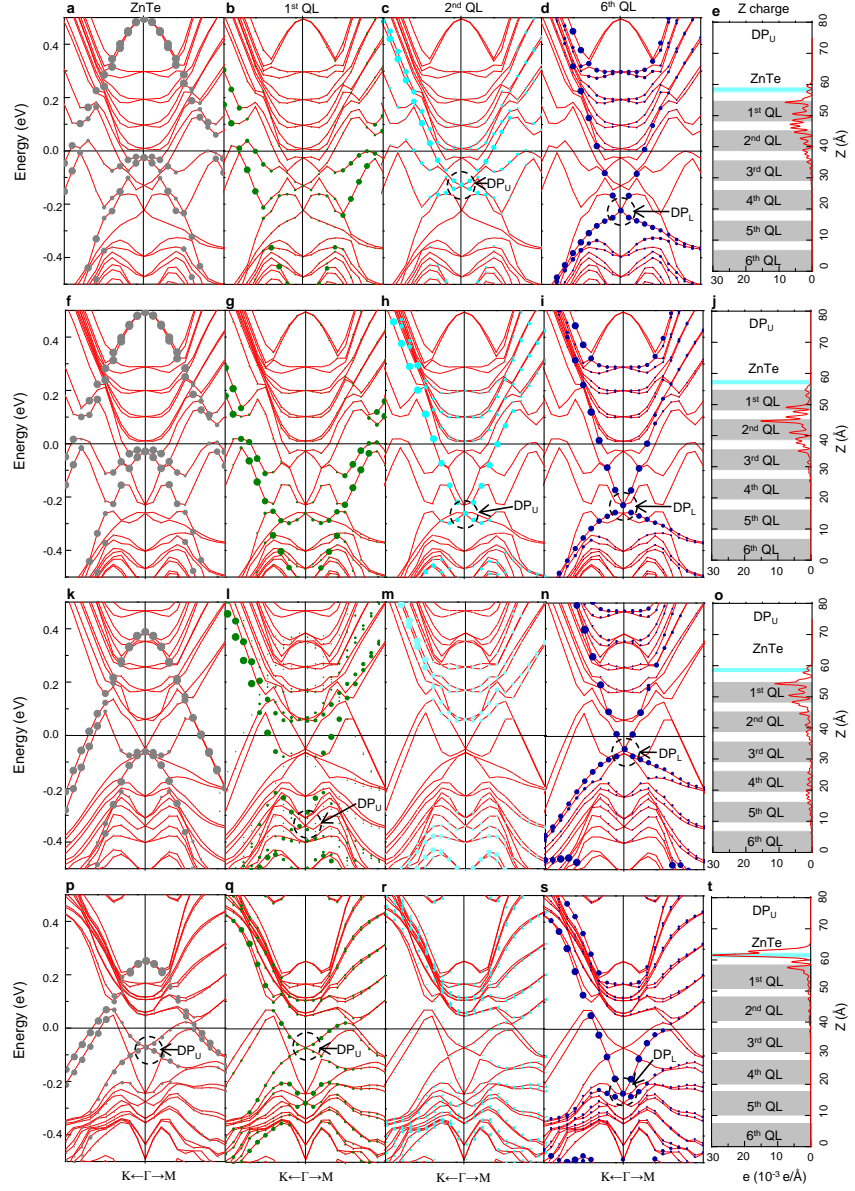


**Figure 4.6:** Band structures of ZnTe/Bi<sub>2</sub>Se<sub>3</sub> and ZnTe/Bi<sub>2</sub>Te<sub>3</sub> along the K- $\Gamma$ -M direction. Band structures of the relaxed ZnTe/Bi<sub>2</sub>Se<sub>3</sub> system (top row), the ZnTe/Bi<sub>2</sub>Se<sub>3</sub> system with an increased separation of 3 Å from 2.5 Å between the 1st QL and 2nd QL (second row), the ZnTe/Bi<sub>2</sub>Se<sub>3</sub> system with an increased separation of 3 Å from 2.6 Å between the CI and 1st QL (third row), and the relaxed ZnTe/Bi<sub>2</sub>Te<sub>3</sub> system (bottom row). All other symbols are the same as in Fig. 4.5.

between the ZnTe film and the 1st QL from 2.6 Å to 3 Å. As expected, the TSS now moves back to the top of the 1st QL.

As yet another strong and complementary support of the above picture, here we study the system of ZnTe/Bi<sub>2</sub>Te<sub>3</sub>, i.e., replacing Bi<sub>2</sub>Se<sub>3</sub> with the structurally nearly identical Bi<sub>2</sub>Te<sub>3</sub>, which is also a TI. The charge transfer is less dramatic than that in ZnTe/Bi<sub>2</sub>Se<sub>3</sub>, as shown by Figs. 4.6 (k-n). The reason lies in the smaller work function of Bi<sub>2</sub>Te<sub>3</sub> than that of Bi<sub>2</sub>Se<sub>3</sub>, and the larger work function of the tensilely strained ZnTe film than that in the ZnTe/Bi<sub>2</sub>Se<sub>3</sub> case (Table 4.2). The band gap of the ZnTe film is also decreased from 1.85 eV in the ZnTe/Bi<sub>2</sub>Se<sub>3</sub> system to 1.39 eV in the present structure, because of the different strains in the two systems (Table 4.2). As a consequence, both the band misalignment [Fig. 4.6 (k)] and binding energy (Table 4.2) between the ZnTe film and the substrate become smaller compared to that in the former case. Naturally, the TSS now floats to the top of the ZnTe film, indicating that the ZnTe is topologized by the Bi<sub>2</sub>Te<sub>3</sub> substrate.

#### 4.2.5 Discussion and conclusion

We note that the dual-proximity effects revealed above are reminiscent of the proximity effect or the Holm-Meissner effect in the field of superconductivity. The peculiarity lies in the dual directions of the proximity effects in the present systems, which is an inherent property of the discrete nature of the  $Z_2$  order parameter for this new class of quantum materials [34, 233, 234, 248]. The precise tunability of the vertical location of the TSS using well-controlled conventional semiconductor overayers is expected to open a new route towards fully exploiting the properties and different manifestations of the TSS in various heterostructures. Appealing examples include exploiting the robust nature of the TSS on top of a conventional catalyst for enhanced surface catalysis, isolating the TSS from the bulk state of TI for conductivity measurement of the TSS, protecting the TSS from gas contamination in air, etc.

Such advances will also enrich our imaginations on the functionality and potential technological applications of the TI-based heterostructures.

# Chapter 5

## Conclusion and Perspective

In this thesis, we have carried out a series of study under the general theme of theoretical modeling of low-dimensional materials and systems, on the topical subjects of diluted magnetic semiconductors, graphene, and topological insulators. Although our work only covers a very small number of topics in the respective areas, not to mention in the whole field of low-dimensional physics, we hope these works can somehow convey our angle of seeing and addressing the problems in these areas, and even beyond.

Throughout this thesis, we have been specially emphasizing the correlation between structure and functionality. In DMS, in order to obtain high Curie temperature one must decrease the amount of interstitial Mn doping. In surface catalysis using gold films supported on oxides, the films must be at just the right thickness to achieve optimal activity. In epitaxial growth of graphene on metal substrates, the surface composition and morphology of the substrates determine the quality of graphene thus obtained. On the one hand, the correlation usually implies some underlying physical mechanisms to be sought out. On the other hand, it simply means one generally should not ignore the structural details of a new system when studying its properties. Moreover, the general experience acquired in the exploration of the correlation between structure and functionality, guided by fundamental physical

principles, can even help to construct or design new systems with desired properties. For example, the electrostatic attraction between *n*- and *p*-type dopants can lead to *n-p* codoped diluted magnetic semiconductors and diluted ferromagnetic graphene with many desired properties. By realizing the possible charge transfer effect facilitated by the delocalized surface states, replacing the inert oxide substrates by topological insulators in gold catalysis can further enhance the catalytic activity of the supported gold films. And, by using a superstructured surface alloy as the substrate to break the orientational degeneracy of small carbon islands in the initial growth stage, grain boundaries of epitaxial graphene can be significantly suppressed.

Although *ab initio* methods have a significant weight in the methodologies used in this thesis, we stress that nowadays a (nearly) complete understanding of a problem or a system generally requires the collaboration between several different methods. This is not only because of the practical limitation of computation power, or the fundamental inadequacy of the *ab initio* methods on certain topics, but also due to the irreplaceable efficiency and elegance of many other methods in revealing the physics in specific situations. For example, with the essential rate parameters obtained by *ab initio* methods, a kinetic Monte Carlo simulation can straightforwardly show the growth behaviors that may not be expected by just looking at the numbers. In estimating the transition temperatures of magnetic systems, the disorder effect is reasonably captured only with the help of the Monte Carlo approach. In our ongoing effort of establishing the theory of RKKY interaction between magnetic nanoparticles deposited on graphene, we are working on a phenomenological model based on the Dirac Hamiltonian of the charge carriers of graphene, with the exchange parameters between graphene and magnetic transition metal nanoparticles obtained by first-principles methods. The model can be readily applied to large systems that cannot be addressed by *ab initio* methods. Moreover, the phenomenological model can give predictions with their physical origins easily traced back to the fundamental physics built in the model. We are going to apply the multi-method multi-scale approach to many other seminal topics such as nanoplasmatics, strongly-correlated oxides, etc.,

in low-dimensional systems and beyond, and expect more excitements to come about in the future.

# Bibliography

# Bibliography

- [1] M. F. Crommie, C. P. Lutz, D. M. Eigler, and E. J. Heller, Surface Review and Letters **2**, 127 (1995). xiv, 4, 5
- [2] B. Hammer and J. K. Nørskov, Advances in Catalysis **45**, 71 (2000). xiv, 6, 7
- [3] Y. Xia et al., Nature Physics **5**, 398 (2009). xiv, 9, 94, 95
- [4] H. Lüth, *Solid Surface, Interfaces and Thin Films*, Springer-Verlag, 2001. 2, 3
- [5] D. J. Chadi, Journal of Vacuum Science and Technology A **5**, 834 (1987). 2
- [6] M. D. Pashley, Physical Review B **40**, 10481 (1989). 2
- [7] C. B. Duke, Chemical Reviews **96**, 1237 (1996). 2
- [8] Q. Xue, T. Hashizume, and T. Sakurai, Progress in Surface Science **56**, 1 (1997).
- [9] S. Lee, W. Moritz, and M. Scheffler, Physical Review Letters **85**, 3890 (2000).
- [10] W. G. Schmidt et al., Physical Review Letters **90**, 126101 (2003). 2
- [11] H. Ibach, *Physics of Surfaces and Interfaces*, Springer, 1 edition, 2006. 3, 4
- [12] Z. Zhang and M. G. Lagally, Science **276**, 377 (1997). 3
- [13] Z. Zhang and M. G. Lagally, editors, *Morphological Organizations in Epitaxial Growth and Removal*, World Scientific Pub Co Inc, 1999. 3

- [14] G. Ehrlich and F. G. Hudda, *The Journal of Chemical Physics* **44**, 1039 (1966). 3, 48
- [15] R. L. Schwoebel and E. J. Shipsey, *Journal of Applied Physics* **37**, 3682 (1966). 3, 48
- [16] Z. Zhang, *Surface Science* **571**, 1 (2004). 4
- [17] Z. Zhang, Q. Niu, and C. Shih, *Physical Review Letters* **80**, 5381 (1998). 4
- [18] I. Tamm, *Phys. Z. Sowjetunion* **1**, 733 (1932). 4, 93
- [19] W. Shockley, *Physical Review* **56**, 317 (1939). 4, 93
- [20] E. Bertel, P. Roos, and J. Lehmann, *Physical Review B* **52**, R14384 (1995). 4, 93, 101
- [21] L. Zhang, E. G. Wang, Q. K. Xue, S. B. Zhang, and Z. Zhang, *Physical Review Letters* **97**, 126103 (2006). 4, 11, 94
- [22] A. Vojvodic, A. Hellman, C. Ruberto, and B. I. Lundqvist, *Physical Review Letters* **103**, 146103 (2009). 4, 93
- [23] J. E. Moore, *Nature* **464**, 194 (2010). 4, 10, 15
- [24] M. Z. Hasan and C. L. Kane, *Reviews of Modern Physics* **82**, 3045 (2010).
- [25] X. Qi and S. Zhang, *Physics Today* **63**, 33 (2010). 4, 10, 15
- [26] A. Nilsson, L. G. Pettersson, and J. K. Nørskov, editors, *Chemical Bonding at Surfaces and Interfaces*, Elsevier Science, 1 edition, 2007. 6, 48, 97, 100
- [27] M. Mavrikakis, P. Stoltze, and J. Nørskov, *Catalysis Letters* **64**, 101 (2000). 7
- [28] M. A. Ruderman and C. Kittel, *Physical Review* **96**, 99 (1954). 7
- [29] T. Kasuya, *Progress of Theoretical Physics* **16**, 45 (1956).

- [30] K. Yosida, Physical Review **106**, 893 (1957). 7
- [31] M. A. H. Vozmediano, M. P. López-Sancho, T. Stauber, and F. Guinea, Physical Review B **72**, 155121 (2005). 8
- [32] Z. F. Ezawa, *Quantum Hall Effects: Field Theoretical Approach and Related Topics*, World Scientific Publishing Company, 1st edition, 2001. 8
- [33] L. Fu and C. L. Kane, Physical Review Letters **100**, 096407 (2008). 10, 103
- [34] X. Qi, T. L. Hughes, and S. Zhang, Physical Review B **78**, 195424 (2008). 10, 103, 111
- [35] R. Yu et al., Science **329**, 61 (2010). 10, 103
- [36] P. N. First, R. A. Dragoset, J. A. Stroscio, R. J. Celotta, and R. M. Feenstra, Journal of Vacuum Science and Technology A **7**, 2868 (1989). 10
- [37] L. Whitman, B. Bennett, E. Kneedler, B. Jonker, and B. Shanabrook, Surface Science **436**, L707 (1999). 11
- [38] S. B. Zhang et al., Physical Review B **69**, 121308 (2004). 11
- [39] S. Yang, L. Zhang, H. Chen, E. Wang, and Z. Zhang, Physics Review B **78**, 075305 (2008). 11
- [40] J. Wintterlin and M. Bocquet, Surface Science **603**, 1841 (2009). 11, 45, 73
- [41] S. Marchini, S. Günther, and J. Wintterlin, Physical Review B **76**, 075429 (2007).
- [42] P. W. Sutter, J. Flege, and E. A. Sutter, Nature Materials **7**, 406 (2008). 73
- [43] J. Coraux, A. T. N'Diaye, C. Busse, and T. Michely, Nano Letters **8**, 565 (2008). 73
- [44] Q. Yu et al., Applied Physics Letters **93**, 113103 (2008). 45

- [45] X. Li et al., *Science* **324**, 1312 (2009). 12, 45, 56, 73
- [46] K. S. Kim et al., *Nature* **457**, 706 (2009). 45, 73
- [47] E. Loginova, N. C. Bartelt, P. J. Feibelman, and K. F. McCarty, *New Journal of Physics* **10**, 093026 (2008). 46, 48, 52, 54, 61
- [48] E. Loginova, N. C. Bartelt, P. J. Feibelman, and K. F. McCarty, *New Journal of Physics* **11**, 063046 (2009). 46, 48, 73
- [49] K. F. McCarty, P. J. Feibelman, E. Loginova, and N. C. Bartelt, *Carbon* **47**, 1806 (2009). 46
- [50] P. Lacovig et al., *Physical Review Letters* **103**, 166101 (2009). 46, 57, 61, 65
- [51] X. Li, W. Cai, L. Colombo, and R. S. Ruoff, *Nano Letters* **9**, 4268 (2009). 12, 46, 56, 73
- [52] E. Loginova, S. Nie, K. Thürmer, N. C. Bartelt, and K. F. McCarty, *Physical Review B* **80**, 085430 (2009). 46
- [53] R. van Gastel et al., *Applied Physics Letters* **95**, 121901 (2009). 11, 45, 46
- [54] H. Chen, W. G. Zhu, and Z. Y. Zhang, *Physical Review Letters* **104**, 186101 (2010). 11, 18, 56, 61, 70
- [55] H. Cao et al., *Applied Physics Letters* **96**, 122106 (2010). 12, 56
- [56] L. Gao, J. R. Guest, and N. P. Guisinger, *Nano Letters* **10**, 3512 (2010). 63
- [57] S. Bae et al., *Nature Nanotechnology* **5**, 574 (2010). 12, 56
- [58] R. G. Van Wesep, H. Chen, W. Zhu, and Z. Zhang, *The Journal of Chemical Physics* **134**, 171105 (2011). 12, 18
- [59] Q. Yu et al., *Nature Materials* **10**, 443 (2011). 12, 63

- [60] P. M. Ajayan and B. I. Yakobson, *Nature Materials* **10**, 415 (2011).
- [61] O. V. Yazyev and S. G. Louie, *Physical Review B* **81**, 195420 (2010). 63
- [62] O. V. Yazyev and S. G. Louie, *Nature Materials* **9**, 806 (2010).
- [63] R. Grantab, V. B. Shenoy, and R. S. Ruoff, *Science* **330**, 946 (2010).
- [64] P. Y. Huang et al., *Nature* **469**, 389 (2011). 12, 63, 67
- [65] K. Kim et al., *ACS Nano* **5**, 2142 (2011).
- [66] J. An et al., *ACS Nano* **5**, 2433 (2011). 12, 63, 67
- [67] W. Chen et al., arXiv:1112.2283 (2011). 13, 18
- [68] S. A. Wolf et al., *Science* **294**, 1488 (2001). 13, 19
- [69] I. Žutić, J. Fabian, and S. Das Sarma, *Reviews of Modern Physics* **76**, 323 (2004). 19
- [70] H. Ohno, *Science* **281**, 951 (1998). 19
- [71] T. Dietl, H. Ohno, F. Matsukura, J. Cibert, and D. Ferrand, *Science* **287**, 1019 (2000). 40
- [72] R. N. Bhatt, M. Berciu, M. P. Kennett, and X. Wan, *Journal of Superconductivity* **15**, 71 (2002).
- [73] C. Timm, *Journal of Physics: Condensed Matter* **15**, R1865 (2003). 13, 19
- [74] T. Jungwirth, J. Sinova, J. Mašek, J. Kučera, and A. H. MacDonald, *Reviews of Modern Physics* **78**, 809 (2006). 13, 19, 20, 40
- [75] R. Q. Wu, *Physical Review Letters* **94**, 207201 (2005). 13, 19
- [76] S. C. Erwin and A. G. Petukhov, *Physical Review Letters* **89**, 227201 (2002).

- [77] K. M. Yu et al., Physical Review B **65**, 201303 (2002). 20
- [78] S. Q. Hao and Z. Y. Zhang, Physical Review Letters **99**, 166101 (2007). 13, 19
- [79] F. D'Orazio et al., Journal of Magnetism and Magnetic Materials **262**, 158 (2003). 13, 20
- [80] C. G. Zeng, W. G. Zhu, S. C. Erwin, Z. Y. Zhang, and H. H. Weitering, Physical Review B **70**, 205340 (2004).
- [81] M. Jamet et al., Nature Materials **5**, 653 (2006). 40
- [82] Y. Kwon, T. Kang, H. Cho, and T. Kim, Solid State Communications **136**, 257 (2005). 13, 20
- [83] W. G. Zhu, Z. Y. Zhang, and E. Kaxiras, Physical Review Letters **100**, 027205 (2008). 13, 16, 20, 85
- [84] H. Chen, W. G. Zhu, E. Kaxiras, and Z. Y. Zhang, Physical Review B **79**, 235202 (2009). 13, 16, 18
- [85] W. Zhu et al., Physical Review Letters **103**, 226401 (2009). 14, 85
- [86] C. Park, Y. Son, L. Yang, M. L. Cohen, and S. G. Louie, Nano Letters **8**, 2920 (2008). 14, 73, 84
- [87] C. Park, L. Yang, Y. Son, M. L. Cohen, and S. G. Louie, Nature Physics **4**, 213 (2008). 14, 73
- [88] C. Park, Y. Son, L. Yang, M. L. Cohen, and S. G. Louie, Physical Review Letters **103**, 046808 (2009). 14, 73
- [89] L. Brey and H. A. Fertig, Physical Review Letters **103**, 046809 (2009). 14, 73
- [90] J. Sun, H. A. Fertig, and L. Brey, Physical Review Letters **105**, 156801 (2010). 14, 73

- [91] W. Zhu, H. Chen, K. H. Bevan, and Z. Zhang, ACS Nano **5**, 3707 (2011). 14, 18
- [92] I. B. Altfeder, K. A. Matveev, and D. M. Chen, Physical Review Letters **78**, 2815 (1997). 14, 73
- [93] C. M. Wei and M. Y. Chou, Physical Review B **66**, 233408 (2002). 14, 74
- [94] Y. Jia, B. Wu, H. H. Weitering, and Z. Zhang, Physical Review B **74**, 035433 (2006).
- [95] Y. Qi et al., Applied Physics Letters **90**, 013109 (2007). 82
- [96] J. Kim et al., Proceedings of the National Academy of Sciences **107**, 12761 (2010). 14, 74, 82
- [97] H. Chen, W. Zhu, D. Xiao, and Z. Zhang, Physical Review Letters **107**, 056804 (2011). 15, 18
- [98] G. Wu et al., to be published (2012). 16, 18
- [99] J. Maassen, W. Ji, and H. Guo, Nano Letters **11**, 151 (2010). 16, 85
- [100] J. Fernández-Rossier and J. J. Palacios, Physical Review Letters **99**, 177204 (2007). 16, 85
- [101] B. Uchoa, V. N. Kotov, N. M. R. Peres, and A. H. Castro Neto, Physical Review Letters **101**, 026805 (2008). 85
- [102] D. C. Elias et al., Science **323**, 610 (2009). 85
- [103] J. Zhou et al., Nano Letters **9**, 3867 (2009). 85
- [104] E. J. G. Santos, D. Sánchez-Portal, and A. Ayuela, Physical Review B **81**, 125433 (2010). 16, 85

- [105] C. Cao, M. Wu, J. Jiang, and H. Cheng, Physical Review B **81**, 205424 (2010).  
16, 85, 87
- [106] D. M. Duffy and J. A. Blackman, Physical Review B **58**, 7443 (1998).
- [107] H. Johll, H. C. Kang, and E. S. Tok, Physical Review B **79**, 245416 (2009). 87
- [108] M. Wu, E. Liu, M. Y. Ge, and J. Z. Jiang, Applied Physics Letters **94**, 102505 (2009).
- [109] T. O. Wehling, A. V. Balatsky, M. I. Katsnelson, A. I. Lichtenstein, and A. Rosch, Physical Review B **81**, 115427 (2010).
- [110] R. C. Longo, J. Carrete, J. Ferrer, and L. J. Gallego, Physical Review B **81**, 115418 (2010).
- [111] V. A. Rigo, T. B. Martins, A. J. R. da Silva, A. Fazzio, and R. H. Miwa, Physical Review B **79**, 075435 (2009). 16, 85
- [112] H. Sevincli, M. Topsakal, E. Durgun, and S. Ciraci, Physical Review B **77**, 195434 (2008). 16, 85
- [113] Y. Zhang et al., Nature **459**, 820 (2009). 17, 80
- [114] S. Qi, H. Chen, X. Xu, and Z. Zhang, to be submitted (2012). 18
- [115] S. Sanvito, G. Theurich, and N. A. Hill, Journal of Superconductivity **15**, 85 (2002). 19
- [116] Y. D. Park et al., Science **295**, 651 (2002). 19, 21, 22, 40
- [117] H. Ohta et al., Physica B: Condensed Matter **298**, 449 (2001).
- [118] H. Nakayama, H. Ohta, and E. Kulatov, Physica B: Condensed Matter **302-303**, 419 (2001).
- [119] S. Abe et al., Applied Surface Science **142**, 537 (1999).

- [120] S. Picozzi et al., Physical Review B **70**, 165205 (2004).
- [121] M. Bolduc et al., Physical Review B **71**, 033302 (2005).
- [122] C. G. Zeng, Z. Y. Zhang, K. van Benthem, M. F. Chisholm, and H. H. Weitering, Physical Review Letters **100**, 066101 (2008). 19, 42
- [123] K. C. Ku et al., Applied Physics Letters **82**, 2302 (2003). 20
- [124] K. W. Edmonds et al., Physical Review Letters **92**, 037201 (2004). 20
- [125] G. Kresse and J. Furthmüller, Physical Review B **54**, 11169 (1996). 21, 47, 57, 64, 74, 86, 94, 103
- [126] P. E. Blöchl, Physics Review B **50**, 17953 (1994). 21, 47, 57, 64, 74, 94, 103
- [127] G. Kresse and D. Joubert, Physical Review B **59**, 1758 (1999). 21, 57, 64, 74, 86, 94, 103
- [128] J. P. Perdew, K. Burke, and M. Ernzerhof, Physical Review Letters **77**, 3865 (1996). 21, 47, 57, 64, 86, 94, 103
- [129] C. R. Hubbard, H. E. Swanson, and F. A. Mauer, Journal of Applied Crystallography **8**, 45 (1975). 21
- [130] A. P. Li, J. Shen, J. R. Thompson, and H. H. Weitering, Applied Physics Letters **86**, 152507 (2005). 21, 22, 40
- [131] S. Ma et al., Solid State Communications **140**, 192 (2006). 21
- [132] Y. Zhao, T. Shishidou, and A. J. Freeman, Physical Review Letters **90**, 047204 (2003). 21, 32, 35
- [133] A. Stroppa, S. Picozzi, A. Continenza, and A. J. Freeman, Physical Review B **68**, 155203 (2003).
- [134] H. Weng and J. Dong, Physical Review B **71**, 035201 (2005).

- [135] P. Mahadevan, A. Zunger, and D. D. Sarma, Physical Review Letters **93**, 177201 (2004). 21, 32, 35
- [136] G. Henkelman, B. P. Uberuaga, and H. Jónsson, The Journal of Chemical Physics **113**, 9901 (2000). 21, 47, 60
- [137] K. Binder, Physical Review Letters **47**, 693 (1981). 22, 37
- [138] H. Ohno et al., Applied Physics Letters **69**, 363 (1996). 22
- [139] H. Ohno, F. Matsukura, T. Omiya, and N. Akiba, Journal of Applied Physics **85**, 4277 (1999). 22
- [140] A. J. R. da Silva, A. Fazzio, and A. Antonelli, Physical Review B **70**, 193205 (2004). 23
- [141] S. Picozzi, M. Ležaić, and S. Blügel, physica status solidi (a) **203**, 2738 (2006). 23
- [142] F. Matsukura, H. Ohno, A. Shen, and Y. Sugawara, Physical Review B **57**, R2037 (1998). 35, 40
- [143] J. Kudrnovský et al., Physical Review B **69**, 115208 (2004). 35
- [144] L. M. Sandratskii and P. Bruno, Physical Review B **67**, 214402 (2003). 35
- [145] K. Sato, W. Schweika, P. H. Dederichs, and H. Katayama-Yoshida, Physical Review B **70**, 201202 (2004). 37, 39
- [146] L. Bergqvist et al., Physical Review Letters **93**, 137202 (2004). 37
- [147] L. Bergqvist et al., Physical Review B **72**, 195210 (2005). 37, 39
- [148] K. W. Edmonds et al., Applied Physics Letters **81**, 4991 (2002). 39
- [149] C. Jaeger et al., Physical Review B **74**, 045330 (2006). 39, 40

- [150] S. F. Edwards and P. W. Anderson, *Journal of Physics F: Metal Physics* **5**, 965 (1975). 40
- [151] R. N. Bhatt and A. P. Young, *Physical Review B* **37**, 5606 (1988). 40
- [152] H. Ohno, *Journal of Magnetism and Magnetic Materials* **200**, 110 (1999). 40
- [153] S. Cho et al., *Physical Review B* **66**, 033303 (2002). 40
- [154] A. P. Li et al., *Physical Review B* **72**, 195205 (2005). 40
- [155] T. Dietl, *Journal of Applied Physics* **103**, 07D111 (2008). 40
- [156] D. Bougeard, S. Ahlers, A. Trampert, N. Sircar, and G. Abstreiter, *Physical Review Letters* **97**, 237202 (2006). 40
- [157] J. Kang et al., *Physical Review Letters* **94**, 147202 (2005). 40
- [158] A. P. Li et al., *Physical Review B* **75**, 201201 (2007). 40
- [159] H. Katayama-yoshida et al., *physica status solidi (a)* **204**, 15 (2007). 40
- [160] A. Continenza and G. Profeta, *Physical Review B* **78**, 085215 (2008). 42
- [161] W. G. Zhu, H. H. Weitering, E. G. Wang, E. Kaxiras, and Z. Y. Zhang, *Physical Review Letters* **93**, 126102 (2004). 43
- [162] A. K. Geim and K. S. Novoselov, *Nature Materials* **6**, 183 (2007). 45, 72
- [163] A. H. Castro Neto, F. Guinea, N. M. R. Peres, K. S. Novoselov, and A. K. Geim, *Reviews of Modern Physics* **81**, 109 (2009). 45, 72, 85
- [164] J. Coraux et al., *New Journal of Physics* **11**, 023006 (2009). 45, 46, 52
- [165] S. Helveg et al., *Nature* **427**, 426 (2004). 46
- [166] F. Abild-Pedersen, J. K. Nørskov, J. R. Rostrup-Nielsen, J. Sehested, and S. Helveg, *Physical Review B* **73**, 115419 (2006). 46

- [167] M. Methfessel and A. T. Paxton, Physical Review B **40**, 3616 (1989). 47, 64, 95, 105
- [168] Y. Mo, W. Zhu, E. Kaxiras, and Z. Zhang, Physical Review Letters **101**, 216101 (2008). 48
- [169] P. J. Feibelman, S. Esch, and T. Michely, Physical Review Letters **77**, 2257 (1996). 48
- [170] O. V. Yazyev and A. Pasquarello, Physical Review Letters **100**, 156102 (2008). 48, 52, 56
- [171] B. Wang, M. Bocquet, S. Marchini, S. Günther, and J. Wintterlin, Physical Chemistry Chemical Physics **10**, 3530 (2008). 48
- [172] N. D. Lang and P. Avouris, Physical Review Letters **81**, 3515 (1998). 57
- [173] S. Tongay, R. T. Senger, S. Dag, and S. Ciraci, Physical Review Letters **93**, 136404 (2004).
- [174] v. Crnjen and G. Baranovic, Physical Review Letters **98**, 116801 (2007). 57
- [175] C. Jin, H. Lan, L. Peng, K. Suenaga, and S. Iijima, Physical Review Letters **102**, 205501 (2009). 57
- [176] H. E. Troiani et al., Nano Letters **3**, 751 (2003).
- [177] T. D. Yuzvinsky et al., Nano Letters **6**, 2718 (2006).
- [178] R. J. Lagow et al., Science **267**, 362 (1995).
- [179] V. Derycke, P. Soukiassian, A. Mayne, G. Dujardin, and J. Gautier, Physical Review Letters **81**, 5868 (1998). 57
- [180] W. Fan, X. G. Gong, and W. M. Lau, Physical Review B **66**, 115418 (2002). 60, 61

- [181] D. Bassett, *Thin Solid Films* **48**, 237 (1978).
- [182] S. J. Koh and G. Ehrlich, *Physical Review Letters* **87**, 106103 (2001).
- [183] P. R. Schwoebel and G. L. Kellogg, *Physical Review B* **38**, 5326 (1988). 61
- [184] P. He, Y. Mao, L. Sun, and J. Zhong, *Journal of Computational and Theoretical Nanoscience* **7**, 2063 (2010). 61
- [185] J. Gao, J. Yip, J. Zhao, B. I. Yakobson, and F. Ding, *Journal of the American Chemical Society* **133**, 5009 (2011). 61
- [186] X. Li et al., *Journal of the American Chemical Society* **133**, 2816 (2011). 63
- [187] X. Li et al., *Nano Letters* **10**, 4328 (2010). 63
- [188] G. Rosenfeld, R. Servaty, C. Teichert, B. Poelsema, and G. Comsa, *Physical Review Letters* **71**, 895 (1993). 64, 70
- [189] J. Schneider, A. Rosenhahn, and K. Wandelt, *Applied Surface Science* **142**, 68 (1999). 64, 68
- [190] G. Bihlmayer, P. Kurz, and S. Blügel, *Physical Review B* **62**, 4726 (2000). 64
- [191] J. G. Chen, C. A. Menning, and M. B. Zellner, *Surface Science Reports* **63**, 201 (2008). 68
- [192] Z. Li et al., *ACS Nano* **5**, 3385 (2011). 68, 70
- [193] C. Barckholtz, T. A. Barckholtz, and C. M. Hadad, *Journal of the American Chemical Society* **121**, 491 (1999). 70
- [194] D. Martoccia et al., *Physical Review Letters* **101**, 126102 (2008). 72
- [195] I. Osborne, M. Lavine, and R. Coontz, *Science* **327**, 1595 (2010). 72
- [196] F. Schwierz, *Nature Nanotechnology* **5**, 487 (2010). 72

- [197] A. K. Geim, *Science* **324**, 1530 (2009). 72
- [198] M. I. Katsnelson, K. S. Novoselov, and A. K. Geim, *Nature Physics* **2**, 620 (2006). 73
- [199] C. W. J. Beenakker, *Reviews of Modern Physics* **80**, 1337 (2008). 73
- [200] V. V. Cheianov, V. Fal'ko, and B. L. Altshuler, *Science* **315**, 1252 (2007). 73
- [201] E. G. Mishchenko, A. V. Shytov, and P. G. Silvestrov, *Physical Review Letters* **104**, 156806 (2010). 73
- [202] J. R. Williams, L. DiCarlo, and C. M. Marcus, *Science* **317**, 638 (2007). 73
- [203] B. Huard et al., *Physical Review Letters* **98**, 236803 (2007).
- [204] B. Özyilmaz, P. Jarillo-Herrero, D. Efetov, and P. Kim, *Applied Physics Letters* **91**, 192107 (2007). 73
- [205] T. Lohmann, K. von Klitzing, and J. H. Smet, *Nano Letters* **9**, 1973 (2009). 73
- [206] H. Chiu, V. Perebeinos, Y. Lin, and P. Avouris, *Nano Letters* **10**, 4634 (2010). 73
- [207] G. Giovannetti et al., *Physical Review Letters* **101**, 026803 (2008). 73, 76, 78, 80, 81
- [208] P. A. Khomyakov et al., *Physical Review B* **79**, 195425 (2009). 73, 74, 76, 78, 80, 81
- [209] Y. Pan et al., *Advanced Materials* **21**, 2777 (2009). 73
- [210] H. Okamoto, D. Chen, and T. Yamada, *Physical Review Letters* **89**, 256101 (2002). 73
- [211] S. Li et al., *Physical Review B* **74**, 075410 (2006). 73

- [212] Y. Guo et al., *Science* **306**, 1915 (2004). 73
- [213] X. Ma et al., *Proceedings of the National Academy of Sciences* **104**, 9204 (2007). 84
- [214] L. Ma et al., *Physical Review Letters* **97**, 266102 (2006).
- [215] P. Jiang et al., *Journal of the American Chemical Society* **130**, 7790 (2008). 73, 84
- [216] J. P. Perdew and A. Zunger, *Physical Review B* **23**, 5048 (1981). 74
- [217] J. Neugebauer and M. Scheffler, *Physical Review B* **46**, 16067 (1992). 76
- [218] G. Makov and M. C. Payne, *Physical Review B* **51**, 4014 (1995). 76
- [219] V. M. Karpan et al., *Physical Review Letters* **99**, 176602 (2007). 82
- [220] K. S. Novoselov et al., *Nature* **438**, 197 (2005). 84
- [221] Z. F. Wang, Y. Zhang, and F. Liu, *Physical Review B* **83**, 041403 (2011). 84
- [222] X. H. Xu et al., *New Journal of Physics* **8**, 135 (2006). 85
- [223] Y. G. Zhou, X. T. Zu, F. Gao, J. L. Nie, and H. Y. Xiao, *Journal of Applied Physics* **105**, 014309 (2009). 85
- [224] X. Wang, Z. Zeng, H. Ahn, and G. Wang, *Applied Physics Letters* **95**, 183103 (2009).
- [225] Y. Zhang et al., *Nanotechnology* **20**, 185504 (2009).
- [226] L. S. Panchakarla et al., *Advanced Materials* **21**, 4726 (2009). 85
- [227] K. T. Chan, J. B. Neaton, and M. L. Cohen, *Physical Review B* **77**, 235430 (2008). 86

[228] B. Uchoa, C. Lin, and A. H. Castro Neto, Physical Review B **77**, 035420 (2008).

86

[229] M. F. Crommie, C. P. Lutz, and D. M. Eigler, Nature **363**, 524 (1993). 93

[230] G. V. Hansson and R. I. Uhrberg, Surface Science Reports **9**, 197 (1988). 93

[231] N. Memmel and E. Bertel, Physical Review Letters **75**, 485 (1995). 93, 101

[232] Z. Cheng et al., Physical Review Letters **105**, 066104 (2010). 93

[233] L. Fu, C. L. Kane, and E. J. Mele, Physical Review Letters **98**, 106803 (2007). 94, 97, 111

[234] J. E. Moore and L. Balents, Physical Review B **75**, 121306 (2007). 97, 111

[235] D. Hsieh et al., Nature **452**, 970 (2008).

[236] T. Zhang et al., Physical Review Letters **103**, 266803 (2009). 94

[237] D. Hsieh et al., Nature **460**, 1101 (2009). 94, 95

[238] Y. L. Chen et al., Science **325**, 178 (2009). 94

[239] M. Haruta, Catalysis Today **36**, 153 (1997). 94

[240] M. S. Chen and D. W. Goodman, Science **306**, 252 (2004).

[241] M. Chen and D. W. Goodman, Chemical Society Reviews **37**, 1860 (2008). 95

[242] M. Bonn et al., Science **285**, 1042 (1999). 94

[243] H. Zhang et al., Nature Physics **5**, 438 (2009). 94, 95

[244] Y. Zhang et al., Nature Physics **6**, 584 (2010). 95, 109

[245] B. Hammer, Y. Morikawa, and J. K. Nørskov, Physical Review Letters **76**, 2141 (1996). 97, 100

- [246] B. Yoon, H. Häkkinen, and U. Landman, *The Journal of Physical Chemistry A* **107**, 4066 (2003). 99
- [247] G. Mills, M. S. Gordon, and H. Metiu, *The Journal of Chemical Physics* **118**, 4198 (2003). 99
- [248] C. L. Kane and E. J. Mele, *Physical Review Letters* **95**, 146802 (2005). 111

# List of Publications

1. Shifei Qi, Hua Chen, Xiaohong Xu, and Zhenyu Zhang, “Diluted Ferromagnetic Graphene via Compensated *n-p* Codoping”, to be submitted.
2. Guangfen Wu, Hua Chen, Yan Sun, Xiaoguang Li, Ping Cui, Cesare Franchini, Jinlan Wang, Xing-Qiu Chen, and Zhenyu Zhang, “Precise Tuning of the Vertical Location of Helical Surface States in Topological Insulator Heterostructures via Dual-Proximity Effects”, submitted to Physical Review Letters.
3. Wei Chen, Hua Chen, Haiping Lan, Ping Cui, Tim P. Schulze, Wenguang Zhu, and Zhenyu Zhang, “Suppression of Grain Boundaries in Graphene Growth on Superstructured Mn-Cu(111) Surface”, arXiv:1112.2283, submitted to Physical Review Letters.
4. Hua Chen, Wenguang Zhu, Di Xiao, and Zhenyu Zhang, “CO Oxidation Facilitated by Robust Surface States on Au-Covered Topological Insulators”, Physical Review Letters **107**, 056804 (2011).
5. Robert Van Wesep, Hua Chen, Wenguang Zhu, and Zhenyu Zhang, “Stable Carbon Nanoarches in the Initial Stages of Epitaxial Growth of Graphene on Cu(111)”, Journal of Chemical Physics **134**, 171105 (2011).
6. Wenguang Zhu, Hua Chen, Kirk H. Bevan, and Zhenyu Zhang, “Formation of Graphene *p-n* Supperlattices on Pb Quantum Wedged Islands”, ACS Nano **5**, 3707 (2011).

7. Hua Chen, Wenguang Zhu, and Zhenyu Zhang, “Contrasting Behavior of Carbon Nucleation in the Initial Stages of Graphene Epitaxial Growth on Stepped Metal Surfaces”, *Physical Review Letters* **104**, 186101 (2010).
8. Hua Chen, Wenguang Zhu, Efthimios Kaxiras, and Zhenyu Zhang, “Optimization of Mn Doping in Group-IV-Based Dilute Magnetic Semiconductors by Electronic Codopants”, *Physical Review B* **79**, 235202 (2009).
9. Shenyuan Yang, Lixin Zhang, Hua Chen, Enge Wang, and Zhenyu Zhang, “Generic Guiding Principle for the Prediction of Metal-induced Reconstructions of Compound Semiconductor Surfaces”, *Physical Review B* **78**, 075305 (2008).

# Vita

Hua Chen was born in Pingdingshan, Henan, China on May 22, 1984, to the parents of Gaoke Chen and Congyu Hua. He attended the Fourteenth Middle School and continued to the Experimental High School of Pingdingshan. He entered Zhengzhou University at Zhengzhou, Henan, China in 2002 for undergraduate study, and got his Bachelor of Science degree in Physics in 2006. In 2007, he went to the University of Tennessee at Knoxville for graduate study and started to work with Prof. Zhenyu Zhang in condensed matter physics. Also in 2007 he married his wife Qin Wang in Hangzhou, Zhejiang, China. Hua graduated with a Doctor of Philosophy degree in Physics in May 2012.